Chemically active micromotors

Von der Fakultat Chemie der Universitat Stuttgart zur Erlangung der Würde eines Doktors der Naturwissenschaften (Dr. rer. nat.) genehmigte Abhandlung

Vorgelegt von

Tingting YU

aus Changsha, China

Hauptberichter: Prof. Dr. Peer Fischer
Mitberichter: Prof. Dr. Thomas Sottmann
Prüfungsvorsitzender: Prof. Dr. Elias Klemm

Tag der mündlichen Prüfung: 08. Juli 2021

Max-Planck-Institut für Intelligente Systeme, Stuttgart

Institut für Physikalische Chemie, Universität Stuttgart

Erscheinungsjahr 2021

Declaration of Authorship

I, Tingting YU, declare that this thesis titled, "Chemically active micromotors" and the work presented in it are my own. I confirm that:

- This work was done wholly or mainly while in candidature for a research degree at this University.
- Where any part of this thesis has previously been submitted for a degree or any other qualification at this University or any other institution, this has been clearly stated.
- Where I have consulted the published work of others, this is always clearly attributed.
- Where I have quoted from the work of others, the source is always given. With the exception of such quotations, this thesis is entirely my own work.
- I have acknowledged all main sources of help.
- Where the thesis is based on work done by myself jointly with others, I have made clear exactly what was done by others and what I have contributed myself.

Signed:

(Tingting Yu)

Date:

Abstract

Motion is a mark of living systems. It is realised by energy conversion to perform vital tasks and is thus of great importance for all living systems. One approach to achieve motion is by including active motion of micro/nano objects. Unlike in the fluid at the macro scale, active swimming cannot be achieved by reciprocal movements at the micro scale. Breaking symmetry at the micro scale thus becomes a critical issue. The challenge is that this often requires outside intervention to build systems that already show symmetry breaking. And another challenge is that there are few examples where active microscale motion can cause a macroscopic effect, or facilitate a useful application.

In the first part of the thesis, the first challenge is addressed and a new route of spontaneous symmetry breaking is developed. Microscale motion in artificial chemical systems has thus far been realised in chemical motion. These are microparticles that are fabricated to possess two different halves, known as Janus particles. One half is catalytically active and drives the self-phoretics. The Janus micromotors are generally fabricated using fabrication techniques such as PVD, CVD. These techniques require deposition onto a surface, which limit the number of structures that can be fabricated. In this work, we show that two species of isotropic (symmetric) micro particles, one is a photocatalytically active particle TiO_2, the other is a passive SiO_2 particle can spontaneously form a dimer structure. Under UV illumination, a chemical gradient is generated around the photo active particles. The passive particle is attracted toward the highest chemical concentration of the reaction product towards the active particle. A dimer forms that starts to self-propel. The speed of the dimer can be controlled by adjusting the UV intensity.

The mechanism of the dimer formation is examined and shown to be due to a diffusiophoretic interaction between the active and the passive particle. The interaction force and the propulsion of the dimer swimmers are examined. The role of salts, particle size and concentration are studied. An additional repulsion interaction is observed between two active particles. An optimal volumetric particle density of $\leq 2\%$ is identified for dimer formation and the dimers remain active for > 20s. This thesis thereby demonstrates a self-assembly route where the chemical activity causes dimer formation and thus spontaneous symmetry breaking which does not require any physical fabrication steps.

Most work thus far has studied the behaviour of individual chemical micromotors (Janus particles) at the micro scale. To induce a macroscopic effect and facilitate an application using individual micro/nano active particles requires cooperative effects of many "micromotors". Therefore, we developed a novel fabrication method which allows a large number of Janus structures to be assembled in an ordered manner. We fabricated an array of photoactive Janus micro structures on a surface by glancing angle deposition (GLAD) onto a photolithography patterned substrate. Illuminating the surface of Janus array structures with UV light initiates the water splitting reaction, which produces an osmotic flow around the micro structures. The osmotic flow at each structure is coupled with the flows generated by the neighbouring particles. The microscopic osmotic flow thereby results in a macroscopic fluid flow. By adjusting the spacing between single micro structures, an optimised pumping velocity is achieved with a micro pillar diameter of 2 μm and a spacing of $\sim$ 2 μm. We compared the pumping performance of the micro pillar array with other topological chemical structures, such as micro Janus bar arrays and 2D micro Janus disk arrays, and find that the 3D structure is essential to generate a chemical gradient on the surface. We believe that this is the first chemical micropump formed by chemically active Janus structures. The active pumping surface can provide a flow speed of up to 4 μm/s.

This active surface consisting of micropillar arrays can be easily integrated in most microchannels and serve as an on-board micropump. A theoretical model and numerical simulations are presented to describe the microchannel pumping. The theory reproduces the experimentally measured flow profiles very well. We have thus established a new type of chemical pump, which can wirelessly pump fluid in a microchannel, and the pumping volume rate and flow profile can be modified simply by changing the nature and orientation of the self-pumping walls.

Zusammenfassung

Bewegung ist ein Zeichen der lebenden Systeme. Es wird durch die Energie umwandlung zur Erfüllung lebenswichtiger Aufgaben realisiert und ist daher für alle lebenden Systeme von großer Bedeutung. Ein Ansatz, um Bewegung zu erreichen, besteht darin, die aktive Bewegung eines Mikro- / Nanoobjekts einzubeziehen. Anders als in der Flüssigkeit auf der Makroskala kann aktives Schwimmen nicht durch gegenseitige Bewegungen auf der Mikroskala erreicht werden. Das Brechen der Symmetrie auf der Mikroskala ist daher eine Bedingung um einen Schwimmer zu realisieren. Die Herausforderung besteht darin, dass dies häufig um ein System zu erstellen, das eine gebrochene Symmetrie aufweist. Eine weitere Herausforderung besteht darin, dass es nur wenige Beispiele gibt, bei denen eine aktive Bewegung im Mikromaßstab einen makroskopischen Effekt hervorrufen oder eine nützliche Anwendung ermöglichen kann.

Im ersten Teil der Arbeit wird die erste Herausforderung angesprochen und ein neuer Weg des spontanen Symmetriebrechens entwickelt. Bewegung im Mikromaßstab in künstlichen chemischen Systemen wurde bisher in chemischer Bewegung realisiert. Dies sind Mikropartikel, die so hergestellt sind, dass sie zwei verschiedene Hälften besitzen, die als Janus-Partikel bekannt sind. Eine Hälfte ist katalytisch aktiv und treibt die Selbstphoretik an. Die Janus-Mikromotoren werden im Allgemeinen unter Verwendung von Herstellungstechniken wie PVD, CVD hergestellt. Diese Techniken erfordern die Abscheidung von Material auf einer Oberfläche, wodurch die Anzahl der herzustellenden Strukturen begrenzt ist. In dieser Arbeit zeigen wir, dass zwei Arten von isotropen (symmetrischen) Mikropartikeln, eines davon ein photokatalytisch aktives TiO_2 Partikel ist, das andere ein passives SiO_2-Partikel ist, die spontan eine Dimerstruktur bilden können. Unter UV- Beleuchtung wird ein chemischer Gradient um die photoaktiven Partikel erzeugt. Das passive Teilchen wird zur höchsten chemischen Konzentration des Reaktionsprodukts nahe des aktiven Teilchens aktiven Teilchen angezogen. Ein Dimer bildet sich, das sich selbst anzutreiben beginnt. Die Geschwindigkeit des Dimers kann durch das Einstellen der UV-Intensität gesteuert werden.

Der Mechanismus der Dimerbildung wird untersucht und kann mit einer diffusiophoretischen Wechselwirkung zwischen dem aktiven und dem passiven Teilchen beschrieben werden. Die Wechselkraft und der Antrieb der Dimerschwimmer werden

untersucht. Die Rolle von Salzen, Partikelgröße und Partikelkonzentration werden untersucht. Eine zusätzliche Abstoßungswechselwirkung wird zwischen zwei aktiven Partikeln beobachtet. Eine optimale volumetrische Teilchendichte von 2% wird für die Dimerbildung identifiziert und die Dimere bleiben für 20 s aktiv. Diese Arbeit zeigt dabei einen Selbstorganisationsweg, bei dem die chemische Aktivität die Bildung von Dimeren und damit das spontane Brechen der Symmetrie verursacht, was keine besonderen Herstellungsschritte erfordert.

Bisher wurde in vielen Arbeiten primär das Verhalten einzelner chemischer Mikromotoren (Janus-Partikel) im Mikromaßstab untersucht. Um einen makroskopischen Effekt zu induzieren und eine Anwendung unter Verwendung einzelner aktiver Mikropartikel Partikel zu ermöglichen, sind kooperative Effekte vieler "Mikromotoren" erforderlich. Daher haben wir eine neuartige Herstellungsmethode entwickelt, die es erlaubt eine große Anzahl geordnerter Janus-Strukturen zu erhalten. Wir haben eine Reihe photoaktiver Janus-Mikrostrukturen auf einer Oberfläche durch die Schattenaufdampfmethode (glancing angle deposition, GLAD) auf ein mit Photolithographie strukturiertes Substrat hergestellt ist. Die Beleuchtung der Oberfläche von Janus-Array-Strukturen mit UV-Licht löst die Wasserspaltungsreaktion aus, die einen osmotischen Fluss um die Mikrostrukturen erzeugt. Der osmotische Fluss an jeder Struktur ist mit den von den benachbarten Partikeln erzeugten Flüssen gekoppelt. Der mikroskopische osmotische Fluss führt dadurch zu einem makroskopischen Flüssigkeitsfluss. Durch Einstellen des Abstands zwischen einzelnen Mikrostrukturen wird eine optimierte Pumpgeschwindigkeit für Mikrostrukturen mit einem Duchmesser von 2 μm und einem Abstand von 2 μm erreicht. Wir haben die Pumpleistung des Mikrosäulenarrays mit anderen topologischen chemischen Strukturen wie Janus-Balken- und Janus-Scheiben-Strukturen verglichen und festgestellt, dass die 3D-Struktur für die Erzeugung eines chemischen Gradienten auf der Oberfläche bedeutsam ist. Wir glauben, dass diese Pumpe die ersten gerichte- ten chemischen Mikropumpen sind, die von chemisch aktiven Janus-Strukturen ge- bildet werden. Die aktive Pumpfläche kann eine Strömungsgeschwindigkeit von bis zu 4 μm/s liefern.

Diese aktive Oberfläche, die aus Mikrosäulenarrays besteht, kann leicht in mikrofluidischen Kanäle integriert werden und dient als integrierte Mikropumpe. Ein theoretisches Modell und numerische Simulationen werden vorgestellt, um das Mikrokanalpumpen zu beschreiben. Die Theorie gibt die experimentell gemessenen Strömungsprofile sehr gut wieder. Wir haben daher einen neuen Typ einer chemischen Pumpe entwickelt, die drahtlos Flüssigkeit in einem Mikrokanal pumpen kann. Die

Pumpvolumenrate und das Strömungsprofil können einfach geändert werden, indem die Art und Ausrichtung der selbstpumpenden Wände geändert werden.

Contents

List of Figures

List of Tables

List of Abbreviations

2D/3D	**T**wo **D**imensional / **T**hree **D**imensional
CB	**C**onduction **B**and
CCD	**C**harge-**C**oupled **D**evices
CMOS	**C**omplemenatery **M**etal **O**xide **S**emiconductor
CVD	**C**hemical **V**apour **D**eposition
DOPA	**D**ihydr**o**xy**p**henyl**a**lanine
E. Coli	**E**scherichia **c**oli
EDX	**E**nergy **D**ispersive **X**-ray
fps	**f**rame **p**er **s**econd
GLAD	**Gl**ancing **A**ngle **D**eposition
HMDS	**H**exa**m**ethyl**di**silizane
LB	**L**angmuir-**B**lodgett
LED	**L**ight-**E**mitting **D**iode
LSPR	**L**ocalized **S**urface **P**lasmon **R**esonance
MD	**M**olecular **D**ynamics
MPCD	**M**ulti**p**article **C**ollision **D**ynamics
MSD	**M**ean **S**quare **D**isplacement
NHE	**N**ormal **H**ydrogen **E**lectrode
PDE	**P**artial **D**ifferential **E**quation

PDMS	**P**oly**dim**ethyl**s**ilane
PS	**P**oly**s**tyrene
PVD	**P**hysical **V**apour **D**eposition
Re	**Re**ynolds number
SEM	**S**canning **E**lectron **M**icroscope
TMAH	**T**etra**m**ethyl**a**mmonium **h**ydroxide
UV	**U**ltra-**V**iolett
VB	**V**alence **B**and
XRD	**X**-**r**ay **D**iffraction

Chapter 1

Introduction

One sign of life in the macroscopic world is the ability to perform motion. The system that in this thesis is studied and investigated is a micro scale chemical motor or swimmer. The property of the fluid determines how an object can swim and thus is discussed in section 1.1.

When micro/nano scale objects suspend in liquid, they move in Brownian motion. Brownian motion plays a significant role in the microscopic motion and affects diffusion, see section 1.2.

Nevertheless, passive diffusion is not an effective way to transport protein or other biomolecules over a distance at macro scale [1]. To introduce active motion in the micro world, the micromotor or -swimmer is designed to be consist of different materials or to shape asymmetric to achieve non-reciprocal motion in a fluid. The principal mechanism to induce motion and to cause the fluid flow to chemical motors are phoretic flows that arise due to local concentration gradients. We will give an introduction to the underlying principles of photo-activated chemical micromotors in section 1.3.

1.1 Low Reynolds number

1.1.1 Reynolds Number at Micro Scale

The behaviour of a flow surrounding a swimming object can be described with the Navier-Stokes equation, which is derived from conservation laws [2]:

$$\rho\frac{\partial \mathbf{u}}{\partial t} + \rho\mathbf{u}\cdot\nabla\mathbf{u} = -\nabla p + \eta\nabla^2\mathbf{u} + \mathbf{f}_{ext} \tag{1.1}$$

where $\mathbf{u}$ is the flow velocity, ρ and η the density and the dynamic viscosity of the fluid, and p the pressure. If the fluid is incompressible:

$$\nabla \cdot \mathbf{u} = 0 \tag{1.2}$$

The terms on the left side of equation 1.1 correspond to inertia, while the three terms on the right side of it to pressure gradient, viscous force and an external force. To investigate the relative importance of inertia and viscosity, the ratio of the two can be considered. An object with characteristic length L and in a flow with a flow speed of u which does not change with time. By analysing the scale of the inertia term in Eq. 1.1 [1]:

$$F_{inertial} \sim \rho u \frac{u}{L} \tag{1.3}$$

And the dissipative force due to the fluid viscosity can be derived from the second term on the right side of equation 1.1 and scales as:

$$F_{viscous} \sim \eta \frac{u}{L^2} \tag{1.4}$$

where η the dynamic viscosity of the fluid. The Reynolds number Re is defined as the ratio of inertia force to viscous force:

$$Re = \frac{F_{inertial}}{F_{viscous}} = \frac{\rho L u}{\eta} \tag{1.5}$$

In the macroscopic realm, the inertia dominates when $Re \gg 1$. Human swimming in water $Re \approx 1.7\ m \times 1\ ms^{-1}/10^{-6}\ m^2 s^{-1} = 1.7 \times 10^6 \gg 1$. For a bacterium with a size of 5 μm and a swimming velocity of 20 $\mu m/s$, the Reynolds number is $10^{-4} \ll 1$. In this case, the contribution of inertia can be neglected. The above equation 1.1 can then be simplified to:

$$-\boldsymbol{\nabla} p + \eta \nabla^2 \mathbf{u} = -\mathbf{f}_{ext} \tag{1.6}$$

The flow around a microswimmer is thus affected by the pressure, the viscous resistance and the external forces applied on the swimmer. Since the time related inertia term has been removed from the equation, the motion of the microswimmer is no more

time-dependent, which is illustrated by the famous scallop theorem by Purcell [3].

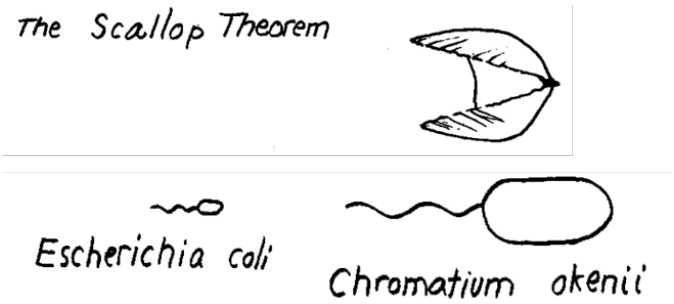

FIGURE 1.1: Sketches adapted from Purcell's paper "Life at low Reynolds number" A scallop does not swim at low Reynolds number while a bacteria does by rotating its flagella [3].

The scallop in Fig. 1.1 opens and closes its shell periodically. This shape change that repeats in a cycle is called reciprocal motion. Since the Stokes equation which can describe the motion in the low Re regime is not dependent on time anymore, no matter how fast or slow the reciprocal motion a scallop is conducting, it will not propel. On the contrary, a rotating bacterial flagellum can swim efficiently at microscale since it is executing a non-reciprocal motion.

When later in this thesis, the focus changes from microswimmer(-motor) to the fluid flow, the equation 1.1 can be simplified in the creeping mode or Stokes equation.

$$-\boldsymbol{\nabla} p + \eta \nabla^2 \mathbf{u} = 0 \tag{1.7}$$

Combining 1.7 and 1.2, can be used to obtain an analytical solution in a microfluidic environment.

1.1.2 Stokes Law

A micro particle moving or diffusing in a fluid, the Reynolds number is very small, $Re \ll 1$. The resistance that the particle experiences arising from the viscosity of the fluid is considered as a drag force and is derived by George Gabriel Stokes in 1851 by solving Stokes flow limit for the Stokes equations.

The frictional force exerted on a moving particle with a radius of R and a speed of u is proportional to the speed u, the surface area of the particle $A = 4\pi r^2$, and by considering the flow changes over a distance of the scale as the particle size r. The exact

equation for calculating the drag resistance is by relating all these relationships and the viscosity with a factor 1.5, given as the Stokes law [1]:

$$F_{drag} = 6\pi r\eta u \tag{1.8}$$

Stokes law is also useful for studying the swimming behavior of microorganisms, the sedimentation of micro particles and organisms in a fluid [4].

1.2 Diffusion and Brownian motion

In 1827, pollen grains were observed to undergo an irregular zigzag motion in water by Robert Brown. It was not understood at that time that whether the pollen grains were experiencing an external force or whether they are active themselves to conduct the motion or to change the motion direction, until 1905, Albert Einstein pointed out that the pollen grains' motion is due to the random collisions with the thermally active water molecules. This motion is at a thermal equilibrium and is called Brownian motion. [5]

1.2.1 Fick's First and Second Law

Diffusion of colloidal particles is a result of Brownian motion induced by random collisions between solvent and particle and due to a gradient of concentration of the colloidal particles. This random translational and rotational motion can be negligible when it refers to a particle with size of tens of microns or larger. With a size of sub-microns or smaller in contrast, these random thermal collisions will be taken into account when trying to understand and predict the behaviour of a propeller [6].

Existing a concentration gradient, a net flux of particles takes place and is proportional to the concentration gradient $\partial c/\partial x$, which shows an opposite direction to the concentration gradient.

Fick's first law describes the net flux of the particle in a concentration gradient:

$$J_x = -D\nabla c \tag{1.9}$$

Where D is the diffusion coefficient. The negative sign indicates the direction of the diffusive flux. The unit of D is $cm^2 \cdot s^{-1}$.

The concentration is changing with time when this concentration gradient varies with position.

The relationship between the change of concentration with time at position x: $\frac{\partial c}{\partial t}$ and the gradient in the flux: $\frac{\partial J}{\partial x}$ is proportional. Fick's second law can therefore be derived from the Fick's first law [7]:

$$(\frac{\partial c}{\partial t})_x = D(\frac{\partial^2 c}{\partial x^2})_t \tag{1.10}$$

1.2.2 Diffusion Coefficient and Mean Concentration Distribution

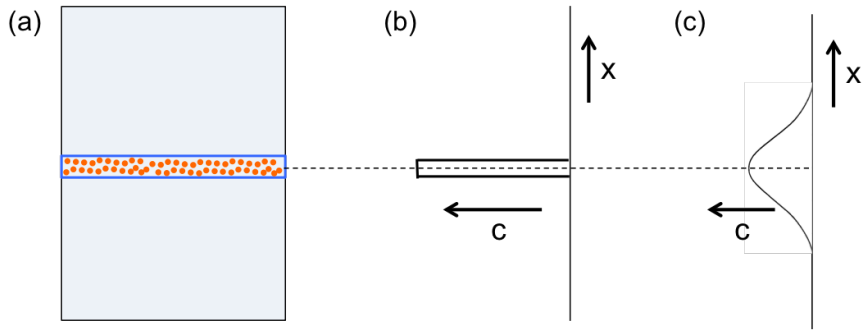

FIGURE 1.2: (a)Particles diffuse from a thin concentrated layer of solute particles: (b) state at time 0; (c) state at time t, which obeys Gaussian distribution. Image adapted from [8].

As shown in Fig. 1.2, assume a thin layer of solute particles located between layers of solvent at t = 0. Equation 1.10 can be integrated, c at position x and time t can be given by [8].

$$c = \frac{1}{(4\pi Dt)^{1/2}} e^{-x^2/4Dt} \tag{1.11}$$

The concentration profile is developed from the initial concentration distribution as shown in Fig. 1.2b at time 0 to the distribution at time t in Fig. 1.2c. The mean square placement $< x^2 >$ can be calculated by integrating the concentration equation [8]:

$$< x^2 >= \int_{-\infty}^{\infty} x^2 c(x) dx = 2 \int_0^{\infty} x^2 \frac{1}{(4\pi Dt)^{1/2}} e^{-x^2/4Dt} dx \tag{1.12}$$

$$< x^2 >= 2Dt \tag{1.13}$$

The diffusion coefficient is half of the mean square displacement over a unit time [8].

$$D = \frac{< x^2 >}{2t} \tag{1.14}$$

1.2.3 Diffusion Coefficient and Microscopic Property

The diffusion coefficient thus can be obtained by analysing the mean square displacement according to 1.13, which is from the macroscopic aspect. The microscopic relation between diffusion coefficient and molecular parameters can be derived by applying Newton's law to a moving object. An object moving with a constant velocity u in viscous medium, the driving force is equal to the frictional force, which is proportional to the velocity with a factor f [8]:

$$F = f\mathbf{u} \tag{1.15}$$

where f is the frictional coefficient, which describes the speed of motion of an object under a driving force. The unit of f is $g \cdot s^{-1}$. The driving force for an object comes microscopically from the average of the random forces provided by the thermal kinetic energy, so that one can substitute the driving force F in Eq. 1.15 with the force from the thermal kinetic energy and get the relation between the diffusion coefficient and the microscopic property [8]:

$$D = \frac{k_B T}{f} \tag{1.16}$$

This is the general form of the Einstein relation, where k_B is the Boltzmann constant, T is the temperature. The microscopic property f is related to the size, shape of the object, and the interaction between the object and the surrounding environment. For a spherical object, the frictional coefficient is delivered by the Stokes' law [8]:

$$f = 6\pi\eta r \tag{1.17}$$

where η is the dynamic viscosity of the surrounding medium, r is the radius of the spherical object.

The diffusion coefficient can thus be given by combining Eq. 1.16 and 1.17, which is known as the Stokes-Einstein equation [8]:

$$D = \frac{k_B T}{6\pi\eta r} \tag{1.18}$$

1.3 Active Chemical Motor

In section 1.2 we have shown that molecules or micro/nano object experience collisions with the solvent molecules, such that it is not an efficient way for an object to be transported over long distances. Furthermore, the viscosity dominates at low Reynolds number. To overcome viscosity from the environment and induce motion at microscale, external energy is required. The microorganisms which move in living systems undergo active swimming instead of passive Brownian motion by converting chemical energy. Artificial microswimmers can be designed to perform complex tasks and are envisioned to be useful in drug delivery, bio sensing and bio therapy. Examples of artificial self-propelled microswimmers and/or nanoswimmers with comparison to biological microswimmers are summarised in [9] and shown in Fig. 1.3 below.

If the particle is able to convert chemical energy into mechanical work, it is driven out of the equilibrium state. This resulting active non-equilibrium process is called active Brownian motion, which combines both active swimming and thermal fluctuations. In section 1.1, we have discussed that a time reciprocal motion at low Reynolds number will not lead to directional net propulsion (swimming) of an object. A time non-reciprocal motion like the rotation of flagella, or any other symmetry breaking way is essential for propelling at micro scale. To design a new type of microswimmers, the symmetry of the particle must be broken.

Chemical motors are powered by a chemical gradient generated from chemical reactions. Since chemical motors obtain mechanical energy from chemical energy of a chemical reaction, and do not undergo any physical shape changing motion like bacteria, they are often called a "motor". The locally generated chemical gradient can propel the colloid by a self-phoretic mechanism. A chemical gradient results due to the asymmetric shape of the catalyst distribution: breaking the symmetry of the motor in shape

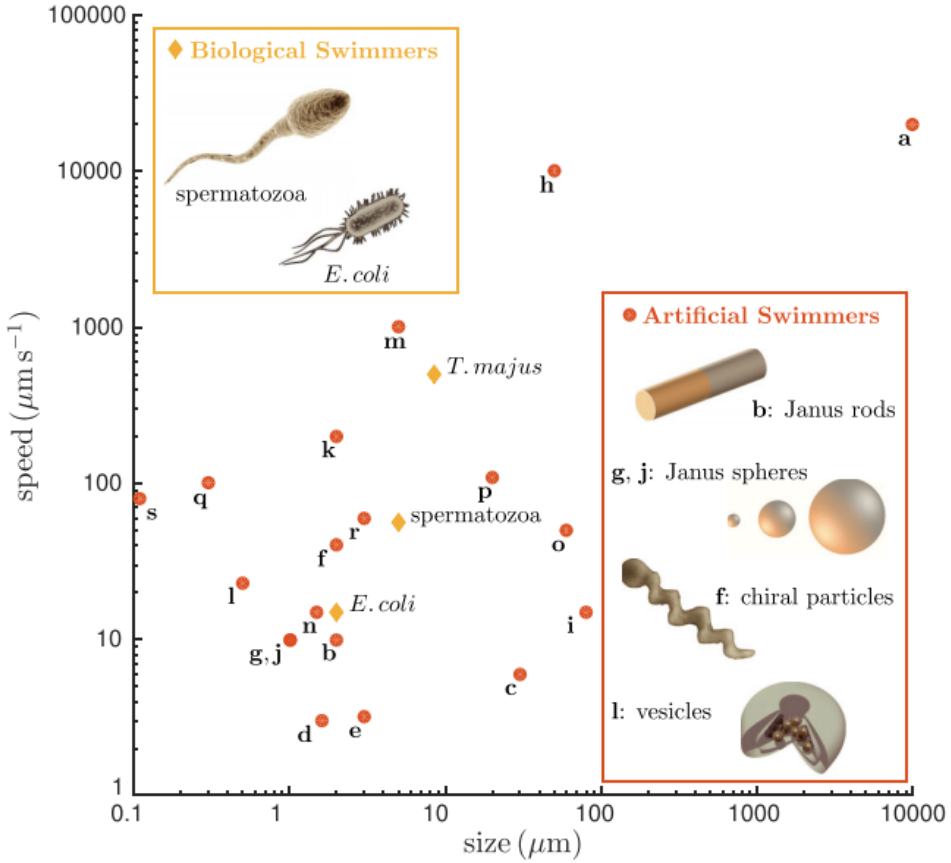

FIGURE 1.3: Examples of biological and artificial microswimmers. The size and speed of typical biological microswimmers, E. coli, spermatozoa for instance, are labeled in the diagram, while some examples of artificial microswimmers are indicated with the corresponding letters in the inset at the right bottom of the diagram. Image taken from [9].

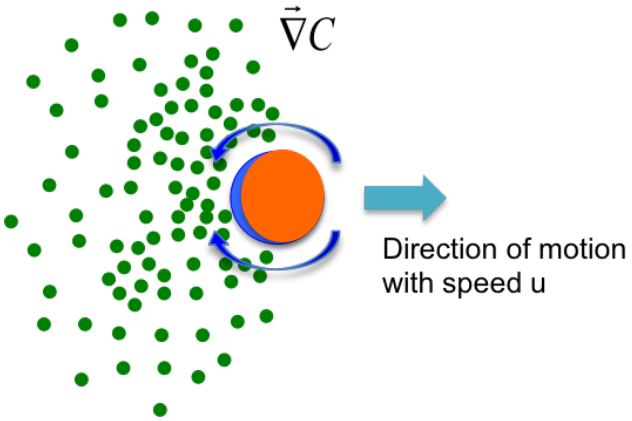

FIGURE 1.4: A two-patch Janus particle with one chemically active side and the opposite side with different reactivity. The material on the blue side reacts or catalyzes a chemical reaction with the fuel molecule in the solution. The product molecules are produced and represented in green dots, which introduces local fluid flow around the particle (blue arrows) and motion of the particle in the opposite direction (green arrow).

or chemical composition.

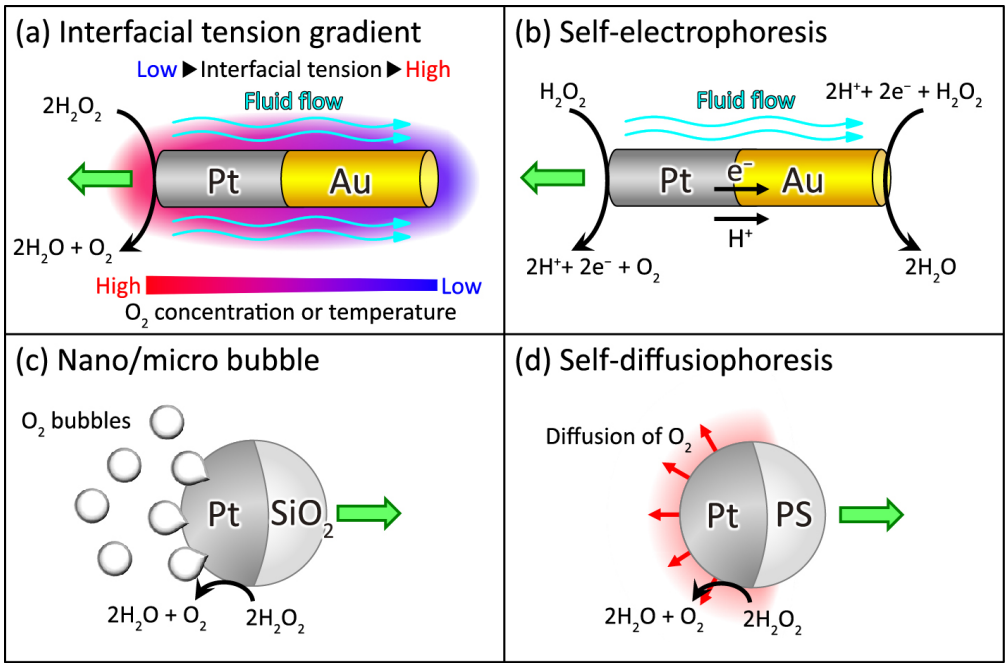

FIGURE 1.5: Catalytic nano/micromotors with different mechanisms: (a) Interfacial concentration gradient, (b) self-electrophoresis (c) nano/micro bubble, and (d) self-diffusiophoresis. Image taken from [10].

Based on the type of the reaction, the chemical motors can be divided into two categories: self reacted [11]–[13] and catalytic motor. A self-reacted chemical motor consists of chemicals which react in/with the solvent to generate an asymmetric chemical field or shape. These motors have a limited lifetime. Catalytic motors in contrast promote a reaction without exhausting, and can be driven by different mechanisms, see Fig. 1.5. For the propelling microrods with the material combination Pt/Au, the motion is induced by an interfacial concentration gradient caused by the chemical product O_2 in water. The direction of the induced flow along the particle surface is from Pt to Au, resulting in an opposite motion of the particle [14]. Later in [15]–[17], an electrokinetic mechanism was developed to interpret the motion of the same system. In the electrophoresis theory, an oxidation reaction takes place at the Pt end, while a reduction reaction at Au end, since the electrons generated at the Pt end transfer to the Au end. The recombination of protons and electrons at the Au end is a result of an induced ion flux towards gold. The particles propel thus in the direction of the Pt end.

$$Pt : H_2O_2 \rightarrow O_2 + 2H^+ + 2e^- \tag{1.19}$$

$$Au : H_2O_2 + 2H^+ + 2e^- \rightarrow 2H_2O \tag{1.20}$$

$$O_2 + 4H^+ + 4e^- \rightarrow 2H_2O \tag{1.21}$$

Other mechanism like bubble propulsion as a result of the chemical reaction at one end of the particle is depicted in Fig. 1.4c [18]. Self-diffusiophoresis shown in Fig. 1.4d as a consequence of the continuously produced chemical gradient will be introduced more in detail in next chapter.

Among all the artificial microswimmers, chemical micro-/ nanomotors are of great interest. They can be easily engineered by changing the chemical reaction material based on the application requirements and the way the motors sense and respond to each other's chemical field can help to understand the collective behaviours in the microbial systems.

This thesis is organized as follows:

Chapter 1 gives an introduction and chapter 2 contains detailed theory and background information relevant to the thesis.

So far, the Janus particles are commonly fabricated by sputtering or thermal deposition of a material onto a monolayer of microparticles, which requires a complex experimental setup with a limited fabrication yield. In chapter 3, a new approach to form Janus particles in solution in larger amounts by self-assembly will be introduced.

In chapter 4, a new chemical micropump is presented.

In chapter 5, the summary and the outlook of the thesis are discussed.

Work presented in this thesis has been in part been published and presented:

- Yu, T., Chuphal, P., Thakur, S., Reigh, S. Y., Singh, D. P., Fischer, P. Chemical micromotors self-assemble and self-propel by spontaneous symmetry breaking, *Chem. Comm.*, 54, pages: 11933-11936, **August 2018**

- Yu, T., Athanassiadis, A., Popescu, M., Chikkadi, V., Güth, A., Singh, D., Qiu, T., Fischer, P. Microchannels with Self-Pumping Walls, *ACS Nano*, 14, 10, 13673-13680, **September 2020**

- Poster: Yu, T., Chuphal, P., Thakur, S., Reigh, S. Y., Singh, D. P., Fischer, P., Chemical Motors that self-assemble, *SPP winter school, 2019* **February 2019**

- Poster: Yu, T., Athanassiadis, A., Popescu, M., Chikkadi, V., Güth, A., Singh, D., Qiu, T., Fischer, P., Photochemically active Janus micro-pillar arrays in narrow fluid channels, *Motile Active Matter International Conference, 2020* **October 2020**

Chapter 2

Theory and Background

2.1 Photocatalytic Activity of TiO_2

In chapter 1, different types of chemical micromotors are briefly introduced. They differ from each other from chemical material to working mechanism. In this section, more details of the catalyst system being utilized in the self-assembled chemical motor (Chapter 3) and the self-pumping wall (Chapter 4) will be discussed.

There are a variety of elements that function as semiconductors. These materials are neither preferable to lose electrons nor to gain electrons. There are normally four electrons in their valence shells, forming perfect covalent bonds with four neighbouring atoms. Semiconductor with only one element include arsenic, boron, carbon, germanium, silicon and etc. Expanding this atom structure unit in space, we get a crystal lattice. In this perfect pure crystal lattice, no electrons are movable and thus the crystal structure is not conductive. A semiconductor is designed by introducing impurities or dopants in the crystal structure. N-type semiconductors hold extra negatively charged electrons, while P-type semiconductors carry positively charged electron holes as charge carriers. Examples of semiconductors with their band gap values are listed in table 2.1.

2.1.1 Photocatalytic Activity Of TiO_2

Since 1972, when water photolysis at semiconductor electrode first being reported by Fujishima and Honda [23], photocatalytic materials have attracted enormous attention for their potential application in solar energy conversion and environmental field. TiO_2 with its photoactivity has been broadly studied due to its nontoxicity, chemical stability, low cost, hydrophilicity, long durability and strong oxidizing ability.

TABLE 2.1: Examples of semiconductor materials [19].

Group	Formula	Bandgap [eV]
IV	Si	1.12 [20], [21]
IV	Ge	0.67 [20], [21]
III - V	GaAs	1.43 [20], [21]
II - VI	CdS	2.42 [21]
II - VI	ZnO	3.37 [21]
Oxide	TiO_2, anatase	3.20 [22]
Oxide	TiO_2, rutile	3.00 [22]

The band gap of TiO_2 (anatase) is 3.2 eV, which corresponds to a photon with a wavelength at $\sim$ 387 μm, which locates in the UV range.

The photogenerated holes and electrons are separated diffusively and are involved in different part of a photocatalytic water splitting reaction. The charge carrier generation [25]:

$$TiO_2 + hv \rightarrow TiO_2 + e^- + h^+ \tag{2.1}$$

The holes produced in valence band diffuse to the TiO_2 surface and promote an oxidation reaction with water, while the electrons in conduction band react with the oxygen to produce superoxide radical anions [26]:

$$h^+ + H_2O \rightarrow^{\bullet} OH + H^+ \tag{2.2}$$

$$e^- + O_2 \rightarrow O_2^{\bullet -} \tag{2.3}$$

2.1.2 Modified TiO_2 Photocatalysis

From the perspective of application and energy, the photocatalysis of TiO_2 remains inefficient due to its large band gap and the recombination of photoinduced charge carriers. To overcome these limits, a variety of methods have been developed, like coupling with a narrow band gap semiconductor, metal ion/ nonmetal ion doping, codoping with two

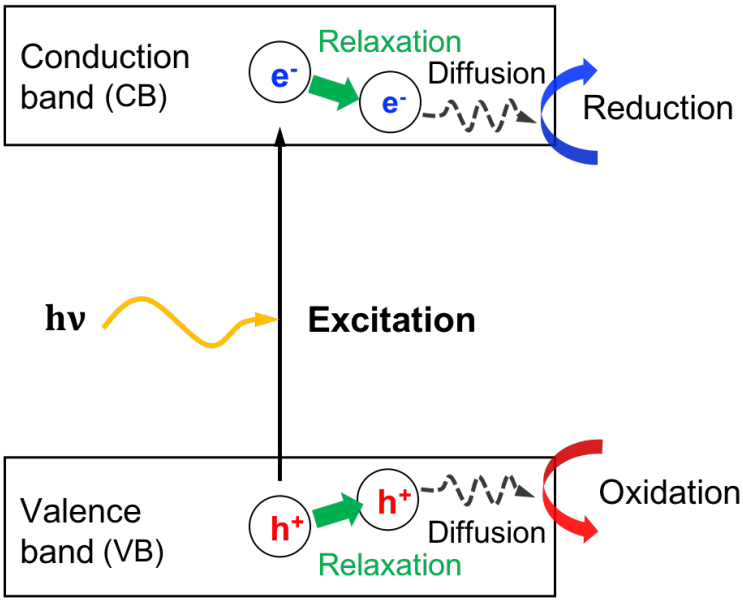

FIGURE 2.1: Electrons move from valence band to the conduction band under light excitation, leaving a positively charged hole in the valence band. The electrons in the conduction band can diffuse and promote a reduction reaction, whereas the separated holes promote an oxidation reaction. Image taken from [24].

or more foreign ions, surface sensitization by organic dyes or metal complexes, surface fluorination, noble metal deposition or the addition of suitable electron acceptors in the reaction medium [27]. In this thesis, we focus on two strategies to improve the efficiency of TiO_2 photocatalysis: Noble metal deposition and the addition of suitable electron acceptors.

Metal deposited titania

If a semiconductor is able to catalyse a water-splitting reaction, charge carriers production and separation in VB and CB are essential. After the transfer of the electrons to CB, the positively charged holes remain in the VB, a water-splitting reaction is in principle possible with the following reduction and oxidation reactions [27]:

$$VB: \quad 2H_2O + 4h^+ \rightarrow O_2 + 4H^+ \tag{2.4}$$

$$CB: \quad 2H^+ + 2e^- \rightarrow H_2 \tag{2.5}$$

The standard reaction potentials of the half reactions of water splitting are [7]:

$$2H^+ + 2e^- \rightarrow H_2, \quad E^o = 0\ V \tag{2.6}$$

$$O_2 + 4H^+ + 4e^- \rightarrow 2H_2O, \quad E^o = -1.23\ V \tag{2.7}$$

The reaction can take place for a reversible electrochemical reaction at constant temperature and pressure when the Gibbs free energy change per mole of the reaction at standard conditions $\Delta_r G \leq 0$ [7]:

$$\Delta_r G^\circ = -nFE^\circ \tag{2.8}$$

Where n is the moles of electrons being transferred in the reaction, F is the Faraday constant and E° is the standard reaction potential. For the hydrogen production reaction 2.5, the CB level should be more negative than hydrogen reduction level (E_{H_2/H_2O}). The VB level should be more positive than water oxidation level (E_{O_2/H_2O} for an efficient production of hydrogen and oxygen from water by photolysis. Theoretically, all the semiconductors fulfill this criteria that the relative positions of the energy levels of valence and conduction bands with respect to E_{H_2/H_2O} and E_{O_2/H_2O} can decompose water by photocatalysis [28].

However, due to the photocorrosion of many semiconductor materials, such as CdS and SiC, their application is strongly limited [27]. In this scenario, TiO_2 proves itself as a promising candidate as a photocatalyst for water-splitting (Fig. 2.2).

However, the energy conversion efficiency in the TiO_2 photocatalytic water-splitting is still low. Possible reasons could be [27], [28]:

- *Recombination of photogenerated charge carriers (electron-hole pair):*
  The excited electrons in the conduction band can recombine with the electron holes in valence band quickly and release energy in form of heat or emitting photons;
- *Fast backward reaction:*
  The water decomposition reaction is an endothermic reaction. The backward recombination of hydrogen and oxygen reaction is more preferable in terms of energy.

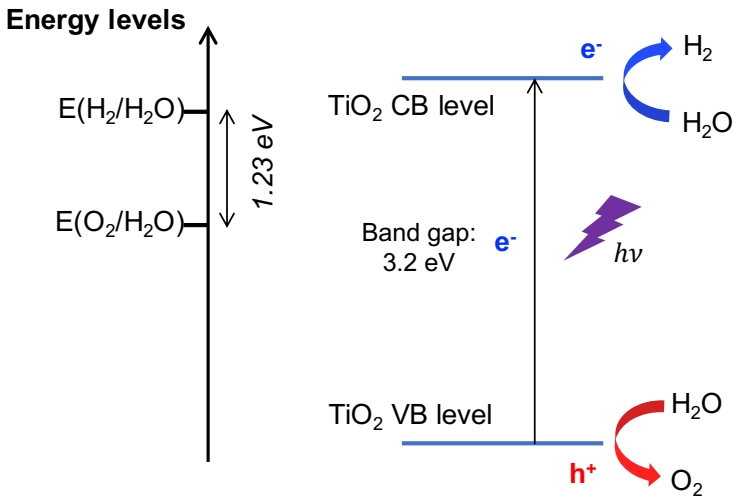

FIGURE 2.2: Mechanism of water-splitting reaction with TiO_2 by photocatalysis which produces oxygen and hydrogen. Image adapted from [28].

Studies reveal that by depositing noble metals on the semiconductor, the efficiency of the photocatalytic process will be significantly enhanced. The metal deposits benefit the interfacial charge transfer as a sink for electrons, and thus weaken the recombination of electrons and holes [27]. Beside of the improved charge separation, the better photocatalytic performance of metal-semiconductor composites can be attributed to the Fermi energy level shifts [29]–[33].

The Fermi level E_F is related to the energy level of the conduction band E_{CB} versus normal hydrogen electrode (NHE), the number of accumulated electrons n_C and the charge carrier density N_C [34]:

$$E_F = E_{CB} + kTlnn_C/N_C \tag{2.9}$$

The Fermi level can be shifted to more negative potential if there is more accumulation of electrons in the system. In the case of TiO_2/Au, Subramanian, Kamat and coworkers determined the Fermi level of TiO_2 and TiO_2/Au with a standard redox couple $C_{60}/C_{60}^{\bullet-}$ with a known $E^{\circ}(C_{60}/C_{60}^{\bullet-}) = -0.25$ V versus NHE. By measuring the concentration of C_{60}^{-} in the TiO_2 or TiO_2/Au suspension under UV radiation at equilibrium, and substituting in the following expression [31], [34]–[36]:

$$E_F^*(TiO_2(e)) = E_{fb} = E^{\circ}_{Ox/Red} + 0.059log([Ox]_{eq}/[Red]_{eq}) \tag{2.10}$$

where E_F^* is the apparent Fermi level of TiO_2 or TiO_2/Au and $E^\circ_{Ox/Red}$ the standard reduction potential of the redox couple. They obtained the apparent Fermi level of -230 mV versus NHE for TiO_2 particles, which is about 270 mV more positive than the conduction band of bulk TiO_2 under neutral pH condition, and a negative shift of Fermi level to -250 mV, -270 mV and -290 mV if the TiO_2 particles are in contact with 8 nm, 5 nm and 3 nm Au particles, respectively. The photogenerated electrons move from TiO_2 to Au, which has a Fermi level of Au = +0.45 V versus NHE, when they contact until the two systems reach equilibrium state. The equation 2.9 depicts that the negative shift of the Fermi level means more accumulated electrons between TiO_2 and Au. This enhanced charge separation in TiO_2/Au is indicative for a higher photocatalytic performance in the system (see Fig. 2.3). A greater energy level shift is shown with smaller size Au nanoparticles, which in turn shows higher catalytic activity [34]. When later at the choice of the thickness of gold halve in Janus TiO_2/Au micropillar in Chapter 4, both the size effect and the robustness of the structure will be considered and balanced.

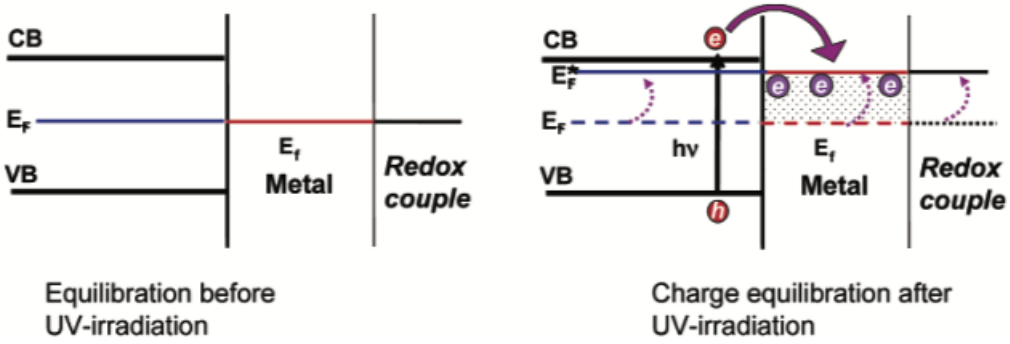

FIGURE 2.3: Charge equilibration before and after UV irradiation in a metal- semiconductor nanocomposites redox couple system. Image taken from [34].

Effects of oxidants on degradation rate

Adding electron acceptors or oxidizing agents in the TiO_2 water suspension can prevent the recombination of electrons and holes. These oxidants can influence the system in following aspects [27], [37]–[39]:

- Number of trapped electrons can be increased so that the recombination with holes is inhibited.
- More free radical and other oxidizing species are produced.
- The oxidation rate of intermediate compounds raises.

- Problems with low oxygen level due to oxygen consumption or slow oxygen mass transfer are avoided.

TABLE 2.2: Oxidation potential for typical oxidants referred to a normal hydrogen electrode. Table taken from [40].

Oxidant	Potential E^0 [V] (25°C)
Fluoride	3.06
Hydroxyl radical	2.80
Hydrogen peroxide	1.78
Oxygen	1.23

Table 2.2 indicates that the H_2O_2 is a stronger electron acceptor than O_2. The reactions that H_2O_2 is involved at presence with TiO_2 are [38], [40], [41]:

$$H_2O_2 + h\nu \rightarrow 2OH^{\bullet} \tag{2.11}$$

$$H_2O_2 + {O_2}^{-\bullet} \rightarrow OH^{\bullet} + OH^{-} + O_2 \tag{2.12}$$

$$H_2O_2 + e^{-} \rightarrow OH^{\bullet} + OH^{-} \tag{2.13}$$

However, the speed of degradation of H_2O_2 can be reduced when the concentration of H_2O_2 is too high. Thereby they serve as scavenger for valence band holes or hydroxyl radicals.

$$H_2O_2 + h^{+} \rightarrow {HO_2}^{\bullet} + H^{+} \tag{2.14}$$

$$H_2O_2 + OH^{\bullet} \rightarrow {HO_2}^{\bullet} + H_2O \tag{2.15}$$

$$H_2O_2 + OH^{\bullet} \rightarrow H_2O + O_2 \tag{2.16}$$

2.1.3 Anatase and Rutile

There are four polymorphs of TiO_2 known in nature: anatase (tetragonal), brookite (orthorhombic), rutile (tetragonal), and TiO_2 (B) (monoclinic) [42]–[44]. The most two common forms are the anatase and rutile crystal structures.

Rutile: Rutile TiO_2 shows a tetragonal structure and contains 6 atoms per unit cell. The octahedron structure of TiO_2 is slightly distorted [45]–[47]. The rutile phase is stable at most temperatures, but the activity of rutile phase is relative poor.

Anatase: Anatase TiO_2 has a tetragonal structure as well, but with a slightly larger distortion of the TiO_2 octahedron in comparison to the rutile phase [46], [48]. The anatase is more stable than rutile at 0 K [49]. It exhibits higher photoactivity than the rutile phase since it has a slightly higher Fermi level, the capacity to adsorb oxygen is low and the hydroxylation degree is higher [50].

Applying different annealing conditions, one can obtain different crystalline structure of TiO_2. Andronic and coworkers have examined the TiO_2 phase with different annealing temperatures by XRD. See results in table 2.3.

TABLE 2.3: Anatase and rutile percentage with different annealing temperature. Table taken from [51].

Annealing temperature [°C]	Crystallite size [nm]		Crystalline phases [%]	
	Anatase	Rutile	Anatase	Rutile
300	8	–	100	–
400	8	–	100	–
500	15	–	100	–
600	32	45	40	60
700	34	50	35	65
800	–	50	–	100
900	–	34	–	100

There are ongoing discussions about the cause of higher activity of anatase TiO_2 [50].

- In semiconductors, an indirect band gap material presents a longer charge carrier life time compared to direct gap materials. For the anatase phase, an indirect band gap is shown, which is usually smaller than its direct band gap. Rutile, in contrast, exhibits a direct band gap or an indirect band gap which is very similar to its direct band gap. The electron-hole pair has longer life in anatase than in rutile, they have higher chance to participate in the oxidation or reduction reactions at the surface [52].

- The transfer of the excitons from the bulk to the surface is also responsible for the photocatalytic activity difference between the two phases. The anatase phase shows deeper excited charge carriers than in rutile. The activity increases for thin anatase films up to $\sim$ 5 nm, while rutile films reach their maximum activity already for $\sim$ 2.5 nm films [52].

2.2 Self-Phoretic Motion

In section 1.1, we have discussed that a non-reciprocal motion is essential for swimming or propulsion in the microscopic world. A typical microswimmer, which swims with a non-reciprocal motion attributing to its asymmertric helical structure is shown in section 1.3. In an alternative category for artificial microswimmers, instead of a complex geometry design, the physical properties of the surrounding medium is intensionally modified and tuned asymmetric so that a micro particle or colloid would experience a driving force. This driving force originates from the asymmetric distribution of a physical change or a chemical substance and gives rise to a phoretic force. It could be from the asymmetric distribution of a physical property like temperature, surface tension, or of a chemical gradient. The driving forces give rise to thermophoresis, phoretic motion by the Marangoni effect, electrophoresis and diffusiophoresis, respectively. The microparticles generate these gradients themselves, experience an interaction between the field of the driving force and the particle surface and are thus able to propel themselves. This type of motion is defined as self-phoretic motion.

In this chapter, we will introduce briefly the differences between thermophoresis, electrophoresis and diffusiophoresis, and mainly discuss the model to describe and understand the diffusiophoresis.

2.2.1 Thermophoresis

Thermophoresis is the motion of particles in a temperature gradient. This phenomenon refers to all phases of matter. The first thermophoresis observation of an aerosol is reported by John Tyndall in 1870. Thermophoresis in a liquid mixture was found by Carl Ludwig in 1856, and the theory was provided by Charles Soret in 1879. Thermophoresis is thus also known as Soret effect. Even though thermophoresis has been known for a long time, its theoretical explanation for molecules in liquids is still unclear [53].

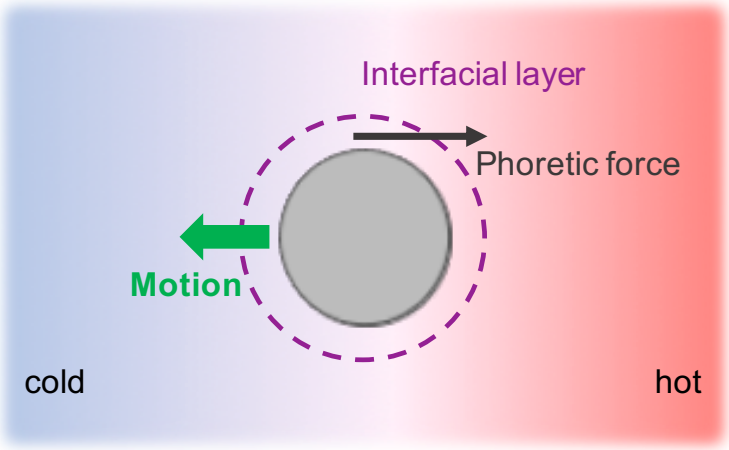

FIGURE 2.4: Schematic illustration of thermophoresis of a particle. The particle displays a motion driven by the phoretic force induced by the interaction between the temperature gradient and the interfacial layer of the particle. Figure adapted from [54].

The colloids in a suspension in a temperature gradient exhibit in addition to Brownian motion, a steady motion velocity [55]:

$$v_s = -D_T \nabla T \tag{2.17}$$

where D_T describes the thermophoretic mobility of a particle and is named as thermal diffusion coefficient [56]. D_T can be positive or negative, indicating the particles move to the cooler region (thermophobic) or hotter region (thermophilic). [57] We can relate this D_T to a model developed by Derjaguin in 1987 for the slip velocity at a solid/liquid interface. In this model, two terms are calculated: the momentum flux resulting from a tangential temperature gradient by applying Onsager's reciprocal therorem, and the flux of energy (enthalpy) which emerges with the pressure-driven convection of the fluid across a porous barrier. By applying the relationship that the momentum flux is equal to the mean flow velocity of liquid through the pores, the slip velocity can be expressed in the following form [58], [59] with the thermal gradient in

the direction of x and a distance y from the solid surface:

$$v_s = -\frac{2}{\eta}\int_0^\infty yh(y)dy\frac{dlnT}{dx} \tag{2.18}$$

where h(y) is the local excess specific enthalpy in the interfacial layer. The integration of h(y) is assigned as a constant H, which tells the excess enthalpy at the interface and is difficult to be measured experimentally [58].

$$H = \int_0^\infty h(y)dy \tag{2.19}$$

Therefore, another approach to determine the thermal diffusion constant is enabled by assuming a uniform thermal gradient directed along x, a steady-state concentration profile can be written with the density distribution [55]:

$$\frac{dc}{dx} = -cS_T\frac{dT}{dx} \tag{2.20}$$

where $S_T = D_T/D = -1/c(dc/dT)$ and is called the Soret coefficient [55]. A positive S_T analog to D_T implies that the colloids move towards the cold. For a specific colloidal suspension, measuring both the given temperature profile and the concentration distribution enables the determination of the Soret coefficient.

2.2.2 Electrophoresis

In electrophoresis, a particle is charged (e.g. -ve here). The charge on the particle surface induces an increased concentration of counterions as a diffuse cloud in the Debye layer κ^{-1}, within which the charge density $\rho_e(y)$ decays exponentially at a distance y from the surface. Placing the charged particle, together with its counterion cloud in an electric field, which can also be generated by the particle itself with a chemical reaction, the diffuse cloud of counterions (+ve) moves in the direction of electric field, while the negatively charged particle moves oppositely. The fluid velocity at the outer edge of the double layer S^+ is the sum of the particle velocity **U** and the slip velocity V_s. [58]

The diffuse space charge density $\rho_e(y)$ interacts with the electric field results in the slip velocity is the difference between the concentrations of counterions and coions.

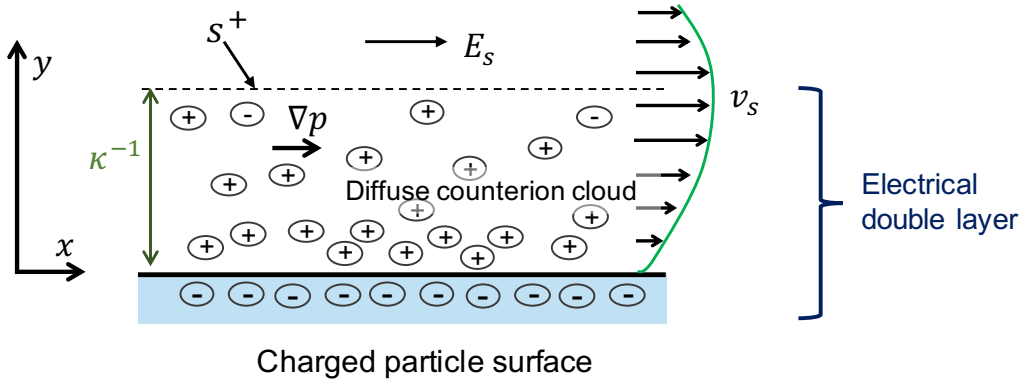

FIGURE 2.5: Electrophoresis of a charged particle (negatively here) in a self-produced or external electric field E_s. The counterion cloud and the negatively charged surface is defined as the electrical double layer. κ^{-1} is the Debye length of the solution, which indicates the interaction range. Figure based on [58].

$\rho_e(y)$ can be derived from Poisson's relation relates to an electrostatic potential at distance y from a charged layer $\psi(y)$ [58]:

$$\rho_e = -\frac{\varepsilon}{4\pi}\frac{\partial^2\psi}{\partial y^2} \tag{2.21}$$

The electric force that the particle body experiences is simply $\rho_e E_s$. The Stokes equation along the x direction is [58]:

$$\eta\frac{\partial^2 v_x}{\partial y^2} + \rho_e E_s = 0 \tag{2.22}$$

The double layer has a length scale of the Debye length [58]:

$$\kappa^{-1} = \left[\frac{8\pi Z^2 e^2}{\varepsilon kT} C^s\right]^{-1/2} \tag{2.23}$$

where C^s is the concentration of electrolyte at the outer edge of the double layer ($\kappa y \to \infty$), Z refers to the valence of the positive and negative ions of the electrolyte, e is the electron charge, ε is the dielectric constant of the fluid, kT the thermal energy. Integrating eq. 2.21, applying the non-slip boundary condition, $v_x = 0$ at y = 0, velocity gradient at $y \to \infty$ is zero, in eq. 2.22 and combining the two equations, the velocity profile within the double layer is obtained [58]:

$$v_x = \frac{\varepsilon}{4\pi\eta}[\psi(y) - \zeta]E_s \tag{2.24}$$

where ζ is called the zeta potential, and equals ψ at y = 0 [60].

The condition that the velocity at the outer edge of the double layer $y \to \infty$ is used to derive the slip velocity v_s [58]:

$$v_s = \lim_{y\to\infty} v_x = -\frac{\varepsilon\zeta}{4\pi\eta}E_s \tag{2.25}$$

where ζ is the zeta potential $\zeta \approx kT/e$, E_s is the electric field with $E_s \approx 1V/cm$, η and ε the viscosity and dielectric constant of water for instance, respectively. We get v_s is of order micrometers per second in water. The slip velocity is linear with E_s. The prefactor $\frac{\varepsilon\zeta}{4\pi\eta}$ defines the electrophoretic mobility of a particle. The charge sign of the particle decides the zeta potential and further influences the direction of the particle motion in the electric field [58].

2.2.3 Phoresis and Chemical Motors

This section is based on and closely follows [1].

Another phoretic driving force initiates from an asymmetric distribution of chemical concentration, which is known as diffusiophoresis. Fick's first law as introduced in section 1.2 relates a flux to a concentration gradient:

$$J_x = -D\frac{dc}{dx} \tag{2.26}$$

The flux in $mol/(m^2 \cdot s)$ can also be written in any of a flow speed u_x:

$$J_x = cu_x \tag{2.27}$$

The flux in Eq. 2.26 is associated with a flow in turn according to Eq. 2.27. This reveals that when there is one species of molecules or particles, the concentration gradient of the molecules or particles causes a diffusion of them from a high concentrated region to low concentrated region. When there are two or more species of molecules or

particles in a suspension, the behaviour that one species presents depends on the concentration gradient of the other species is a result of the interaction between the solute and the surface of the molecule or particle. The interaction in this scenario can include van der Waals forces, dipolar forces, or volume exclusion effects (entropy-driven effects). We combine these forces together and define a combined potential "potential of mean force" ϕ:

$$\vec{f}_{ext} = -\vec{\nabla}\phi \tag{2.28}$$

which delivers the force experienced by a solute molecule from the surface. To include all the solute molecules, the term concentration of the solute c dependent on the position along the surface x and the distance away from the surface y, $c(x,y)$ is introduced. The force points along the y direction and varies with x since the concentration of solute molecules distributes ununiformly along x. The combined force for many solute molecules at a specific location is given by:

$$F_y(x) = -c(x,y)\frac{d\phi(y)}{dy} \tag{2.29}$$

Since the force changes along x, the force per area of the particle generates a $p(x,y)$. Each volume element experiences a different force so that the generated pressure changes as well, which in turn acts on a fluid element and results in a hydrostatic pressure. On an infinitely long wall, the pressure difference along the wall drives a fluid flow, which is named diffusioosmosis. The flow along the surface is with a speed u_x. At the surface, when $y = 0$, the $u_x = 0$ due to the non-slip condition of the surface. u_x increases within a short distance away from the surface due to the hydrostatic pressure and then reduced eventually to zero again. The flow profile at the surface is shown in Fig. 2.6.

2.2.4 Diffusioosmosis

This section is based on and closely follows [1].

An external force term is added to the Stokes equation to describe the fluid behaviour in the interfacial layer between the solute and the surface in presence of a concentration

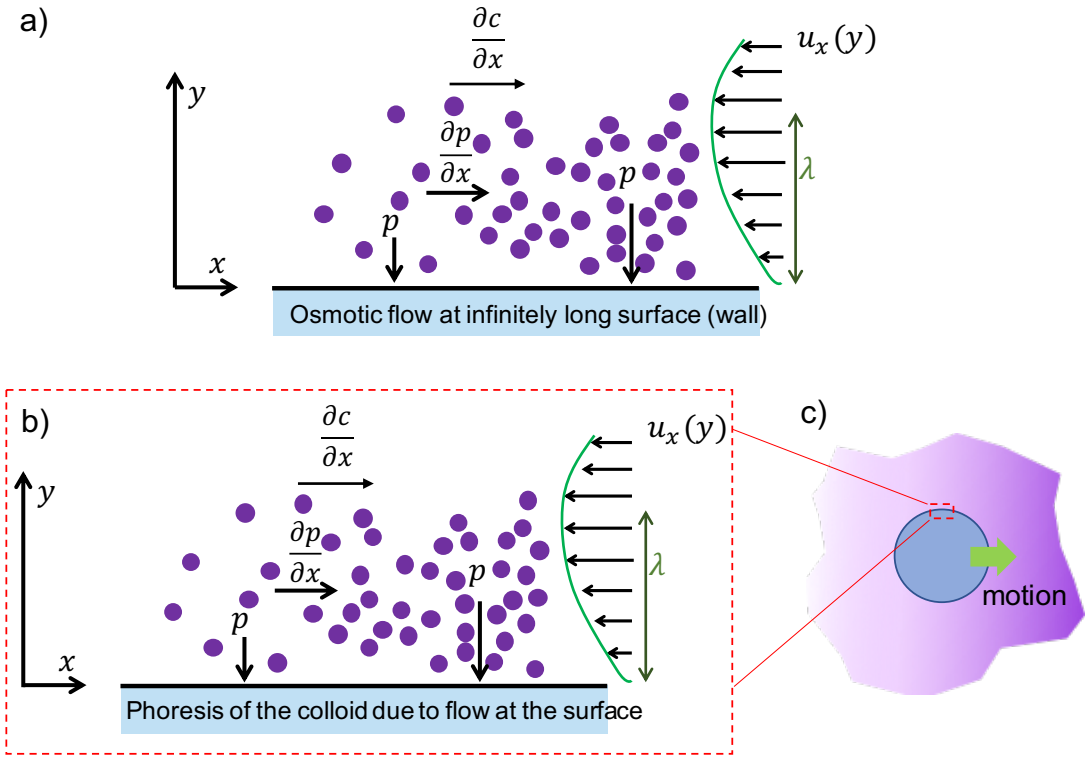

FIGURE 2.6: Diffusioosmosis and phoresis caused by a concentration gradient. (a) The fluid flow u_x is driven by a tangential pressure gradient $\vec{\nabla}p$ pointing in the direction from higher pressure to lower pressure, which is caused by the interaction between the solute molecules and the surface. λ refers to the range of the potential, the scale of which is much smaller than the colloid, $\lambda \ll R$, R is the radius of the colloid. (b) is a zoom in of the interfacial layer in (c). A colloid moves in a concentration gradient (purple shading) in (c), this phenomenon is termed diffusiophoresis.

gradient. The external force is due to the interaction potential:

$$\vec{\nabla} p - \eta \nabla^2 \vec{u} = -c\vec{\nabla}\phi \tag{2.30}$$

For an incompressible Newtonian fluid:

$$\vec{\nabla} \cdot \vec{u} = 0 \tag{2.31}$$

There are two dimensions for the quantities in Eq. 2.30: x along the surface and y the distance away from the surface. The pressure changes along x and y, the velocity points along x and changes along y, concentration changes along x and y, and the interaction potential changes with y. The Stokes equation is therefore rewritten in terms of two directions:

At a distance y from the surface:

$$\frac{\partial p(x,y)}{\partial z} = -c(x,y)\frac{\partial \phi(y)}{\partial y} \tag{2.32}$$

Along the surface x:

$$\frac{\partial p(x,y)}{\partial x} - \eta \frac{\partial^2 u_x(y)}{\partial y^2} = 0 \tag{2.33}$$

The concentration of solute molecules follows the Boltzmann distribution:

$$c(x,y) = c_b(x) exp(\frac{-\phi(y)}{kT}) \tag{2.34}$$

where c_b is the concentration of the solute molecules in the bulk, $c_b(x) = c(x; y > \lambda$. Substituting $c(x,y)$ from Eq. 2.34 in Eq. 2.32:

$$\frac{\partial p(x,y)}{\partial y} = -c_b(x) exp(\frac{-\phi(y)}{kT})\frac{\partial \phi(y)}{\partial y} \tag{2.35}$$

Integrating the Eq. 2.35 by y gives:

$$p(x,y) = c_b(x)kT(e^{-\phi(y)/(kT)} - 1) \tag{2.36}$$

This equation is differentiated with respect to x so that the pressure gradient along x can be substituted in Eq. 2.33.

$$\frac{\partial p(x,z)}{\partial x} = \frac{\partial c_b(x)}{\partial x}kT(e^{-\phi(y)/(kT)} - 1) \tag{2.37}$$

Simultaneous Eq. 2.33 and 2.37:

$$\eta\frac{\partial^2 u_x(y)}{\partial y^2} = \frac{\partial c_b(x)}{\partial x}kT(e^{-\phi(y)/(kT)} - 1) \tag{2.38}$$

This equation will be integrated twice along y. The term contained the unknown interaction potential $\phi(z)$ will be assigned to:

$$\beta = \int\int (e^{-\phi(y)/(kT)-1)}dydy \tag{2.39}$$

The speed of the diffusioosmotic flow near the surface is ultimately given in the following expression:

$$u_x = -\frac{\partial c_b(x)}{\partial x}\frac{kT}{\eta}\beta \tag{2.40}$$

and the general form is:

$$u_{\|} = -\nabla_{\|}c\frac{kT}{\eta}\beta \tag{2.41}$$

where $u_{\|}$ is the tangential flow which is parallel to the surface. The flow speed is linear to the concentration gradient and is related to the temperature, the viscosity of the fluid and the interaction potential.

2.2.5 Diffusiophoresis

This section is based on and closely follows [1].

When a force free particle is in a solution with concentration gradient which in turn generates a tangential flow along the surface, due to the conservation of momentum, the particle has to move to the opposite direction to give space for the fluid flow. The motion of the particle is called the diffusiophoresis of the particle. The speed of the diffusiophoretic motion U is calculated by integrating the flow across the entire surface of the particle with a radius R. The direction is reversed as the diffusioosmotic flow:

$$U = -\frac{1}{4\pi R^2}\int_{surface} u_{\parallel} dS \tag{2.42}$$

more generally:

$$\vec{U} = \beta\frac{kT}{\eta}\vec{\nabla}c_{ext} \tag{2.43}$$

where c_{ext} is the concentration distribution of the solute where the colloid locates, all the constants and interaction potential are included in ξ. The sign of the phoretic velocity indicates the motion direction of the colloid. With an attractive interaction, the colloid moves towards the higher solute concentration region leads to a lower energy. When the interaction is repulsion instead, the colloid moves in the opposite direction to a lower solute concentration.

In summary, phoretic propulsion describes the motion of colloidal particles by a gradient field that has interaction with the surface of a particle. The interaction takes place in an extremely thin interfacial layer. The phoretic speed is generally proportional to the field gradient. The proportionality is defined by the phoretic mobility, which contains the constant parameters of the system and interaction potential related parameters. The three different phoretic motions are compared in table 2.4.

TABLE 2.4: The gradient and the phoretic mobility which determine the phoretic speed [58].

	Gradient field	**Phoretic mobility**
Thermophoresis	Temperature	$yhdy$
Electrophoresis	Electrical potential	$-\frac{\varepsilon\zeta}{4\pi\eta}$
Diffusiophoresis (non-ionic)	Concentration of a chemical species	$\beta\frac{kT}{\eta}$

2.2.6 Self-Phoresis

If a particle can itself generate a gradient in temperature, electric charges or concentration, it can move. The motion is defined as self-phoretic motion. To achieve this functionality, a spherical particle needs to break its local symmetry to induce a specific gradient into the system. There are many ways to prepare an asymmetric microsized particles, *e.g.* membrane templated electrodeposition, bipolar electrochemical deposition, layer-by-layer assembly and physical vapour deposition [61].

Self-thermophoresis

To obtain a temperature gradient surrounds a particle, the thermal response at the two ends of a sphere should differ from each other. An example of design is shown in Fig. 2.7 [62].

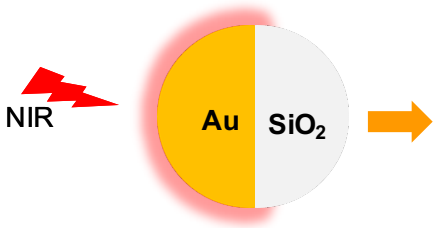

FIGURE 2.7: Themophoretic motion driven by a temperture gradient caused by the adsorption of near infrared light by gold on one side of the particle.

Thermophoretic system is usually less energetically efficient. Relatively large light intensities are needed. The application is thus limited.

Electrophoresis

- Induced-charge electrophoresis

As discussed in section 2.2.2, induced-charge electrophoresis takes place when a particle is charged and an external electric field is applied. The couterions cloud in the electric double layer moves to the direction in response to the electric field. An induced electrophoretic particle is presented in Fig. 2.8.

- Self-electrophoresis

A self-electrophoretic particle can generate an ionic flux itself, when it catalyses a chemical reaction to produce charged products. On the other side, a conductive material

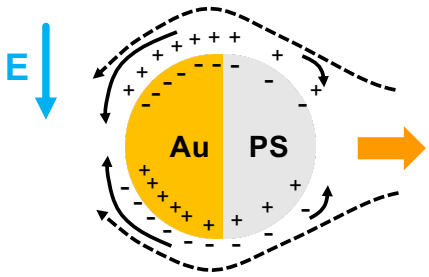

FIGURE 2.8: The heterogeneous distribution of the charges is induced by an external electric field on the particle. The electric double layer on the gold side is more strongly polarized and is able to drive an induced electroosmotic slip than the polystyrene side. The induced motion is the direction of the dielectric side. Image based on [63]

is present to separate and transfer the electrons to its side, which are products of the reaction at the other end. The redistribution of negatively charged electrons and positively charged protons causes a proton flow towards the electron accumulated side. (Fig. 2.9)

The self-induced electric field in a solution is determined by the ion diffusivity difference factor ξ and concentration gradient of solute ∇C, and is given as [64]:

$$\mathbf{E} = \frac{kT}{Ze}\xi\frac{\nabla C}{C} \tag{2.44}$$

where Z is the valence of the ions of the solute, C is the concentration of the ions, ξ is the ion diffusivity difference factor and is related to the diffusivities of the constituent ions, namely the cation diffusivity D_+ and anion diffusivity D_-:

$$\xi = (D_+ - D_-)/(D_+ + D_-) \tag{2.45}$$

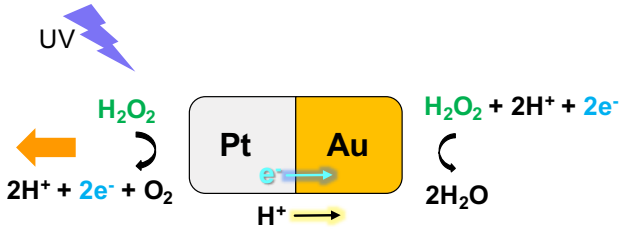

FIGURE 2.9: Schematic illustration of self electrophoresis. Hydrogen peroxide is decomposed and produces protons in the solution and electrons in the tube at the Pt side. The protons and electrons are transferred to the Au side and react with H_2O_2 to water there. This ion flux causes a motion of the particle relative to the fluid towards the platinum side [15].

Self-diffusiophoresis

Pt in above mentioned self-electrophoretic particle catalyses a H_2O_2 oxidation reaction, it produces not only protons and electrons, other main products are H_2O and O_2 as illustrated in Fig. 2.10. The reaction generates eventually a local concentration gradients of both educt and product across the particle. This concentration gradient induces a pressure gradient which in turn drives a fluid flow surrounding the particle and a self-diffusiophoretic motion of the particle.

When the Au side in the self-electrophoretic particle is replaced by a non-conductive inert material, polystyrene for instance. The electrons can not be transferred from the Pt side. The ionic flux will be reduced, and mainly a concentration gradient remains surrounding the particle [65].

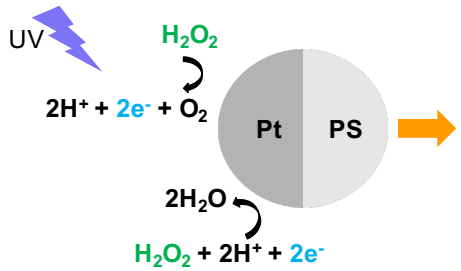

FIGURE 2.10: Schematic depiction of a Pt/PS Janus particle, which conducts self-diffusiophoresis in H_2O_2 solution under illumination of UV light. The Pt catalyses a chemical reaction of H_2O_2 and produces O_2 and H_2O. The one-sided distribution of these chemical products across the particle results in a pressure gradient and drives the particle to move. Image based on [65].

In the section 2.1.2, noble metal is deposited on photoactive catalyst to enhance the photocatalytic activity. With the design of a photocatalyst and a noble metal, the particle exhibits a motion with both self-electrophoretic and diffusiophoretic effects.

2.2.7 Chemical Gradient

To investigate the concentration distribution in space $C_{H_2O_2}(r)$ around a chemical catalytically active particle, TiO_2 sphere with a radius R for instance, two terms related to the concentration change of the educt/product: the diffusion and the kinetic reaction of the educt molecules are considered and combined in Eq. 2.46 [69]:

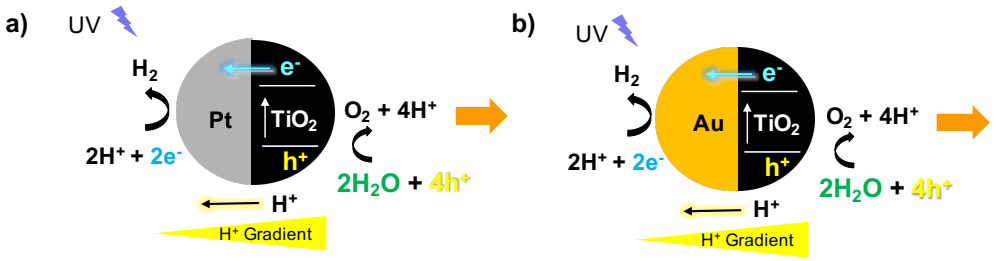

FIGURE 2.11: Cartoon illustrating that a photocatalyst/noble metal particle combines both self-electrophoresis and diffusiophoresis effects and propels. In both a) and b), the under UV illumination generated hole/ electron pair is separated by transferring the electrons to the noble metal side. The protons produced by the reaction of H_2O with the holes tend to move to the noble metal side for a recombination reaction with electrons for hydrogen production. This proton flux drives the motion of the particle self-electrophoretically. Meanwhile, the concentration gradient of the reactant and product initiated from the catalyst side propels the particle self-diffusiophoretically. Image adapted from [66]–[68].

$$\frac{\partial C_{H_2O_2}(r)}{\partial t} = D \cdot \Delta C_{H_2O_2}(r,t) - \alpha C_{H_2O_2}(0,t) \tag{2.46}$$

which is indicated as the diffusion-reaction equation, where r is the distance from the particle surface, t is the time, D is the diffusion coefficient of hydrogen peroxide, α the reaction rate constant of the chemical reaction on the active surface at $r = 0$.

When our system reaches a steady state, the time related term vanishes and gives a Laplace equation:

$$D \cdot \Delta C_{H_2O_2}(r) = \alpha C_{H_2O_2}(0) \tag{2.47}$$

The concentration distribution in terms of r is obtained by solving the Laplace equation for an infinite large reservoir of hydrogen peroxide solution: [69]

$$C_{H_2O_2}(r) = C_{H_2O_2}(\infty)\left(1 - \frac{R/2}{r}\right) \tag{2.48}$$

Where $C_{H_2O_2}(\infty)$ is the bulk concentration of hydrogen peroxide, R is the size of the catalytic site. Consuming hydrogen peroxide gives a production in oxygen that dissolves in the solution at very low concentration. The oxygen concentration distribution is given by taking the stoichiometry of the reaction equation into account:

$$C_{O_2}(r) = C_{H_2O_2}(\infty)\frac{R}{r} \tag{2.49}$$

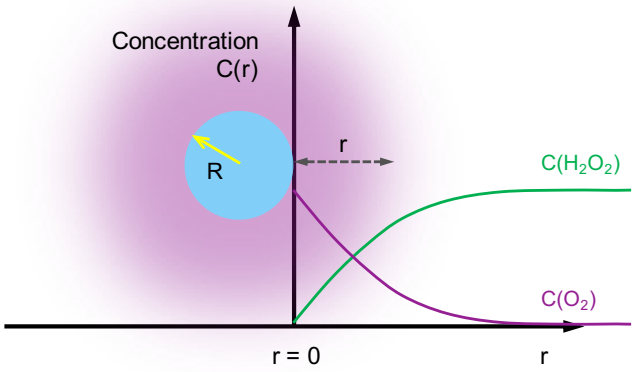

FIGURE 2.12: The chemical gradient of H_2O_2 and O_2 in a hydrogen peroxide decomposition reaction at a spherical catalytic particle surface with a radius R. The concentration of H_2O_2 and O_2 drop from a distance to the surface, and from the surface to infinitely far from the surface reciprocally, respectively. Image based on [69].

The diffusiophoretic velocity surrounding the catalytically active particle is thus dependent on the distance from the particle as well. Eq. 2.43 depicts that the diffusiophoretic velocity u_p is proportional to the chemical gradient $\nabla C(r)$: $u_p \propto \nabla C(r)$, and $C(r) = C_{H_2O_2}(\infty)R/r$ so that [69]:

$$u_p \propto C_{H_2O_2}(\infty)R\nabla\frac{1}{r} \propto 1/r^2 \tag{2.50}$$

The dependence of the diffusiophoretic velocity on the distance to the catalytically active particle is illustrated in Fig. 2.13.

2.3 Flow in Microchannels

So far, the chemical system and the propulsion mechanism for the chemical micromotors are discussed. By constructing chemical motors on a substrate in a large array manner, a self-pumping active wall can be applied to pump fluid in a microchannel (Cahpter 4). Now, I will present the theoretical background of typical fluid pumping in microchannel.

Microchannels can be used in drug delivery devices [70], [71], micro total analysis systems and other microfluidic devices [72]–[78]. The basic fluidic analysis to describe the flow in the microchannel can help for a better understanding of the flow properties

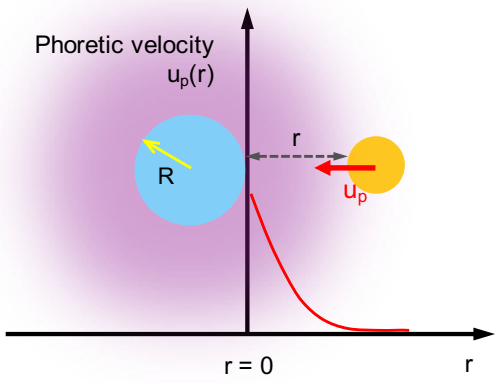

FIGURE 2.13: The diffusiophoretic velocity towards a catalytically active particle is proportional to the chemical gradient, showing a $u_p(r) \propto 1/r^2$ tendency. Image based on [69].

and for improving the performance of microanalysis or microfluidic device [78]. The microchannels normally have a cross-section size of micrometers to sub milimeter. As Eq. 1.5 indicates, at the low Reynolds regime, viscosity plays a more important role than inertia, where the incompressible flow in microchannels develops itself in a laminar flow manner rather than a turbulent flow. The fluid exhibits a creeping flow mode and can be mathematically described by the Stokes equation [2].

The cylindrical microchannel is the simplest analytical model among different channel geometries. A usual way of analyzing for a noncircular cross-section microchannels is by considering the equivalent hydraulic diameter [78], [79] in the 1D analysis of Hagen-Poiseuille for a cylindrical channel [80].

2.3.1 Pressure Force

The Navier-Stokes equation 1.1 describes the forces acting on a fluid parcel, and consists of three terms: the viscosity of the fluid, the pressure on the fluid and an external force term. The system described in this thesis experiences no external force. Flows are therefore caused by pressure differences which push the fluid from regions of higher pressure to regions of lower pressure. The pressure gradient $\frac{dp}{dx}$ is responsible for the driving of a flow. A counteracting force to this driving force is the frictional force in the fluid. Friction is set by the fluid viscosity and exists between the fluid and the channel and also within the fluid itself. Here, with the aid of a cylindrical channel model,

the pressure drop, frictional force and volume flow rate in a cylindrical channel will be shown. A section of cylindrical channel illustrated in Fig. 2.14 has a length of δx, a cross-section with an area of A and a radius of r. A pressure drop ($\delta p < 0$) is applied on the channel from position x_1 to x_2 [2], [81].

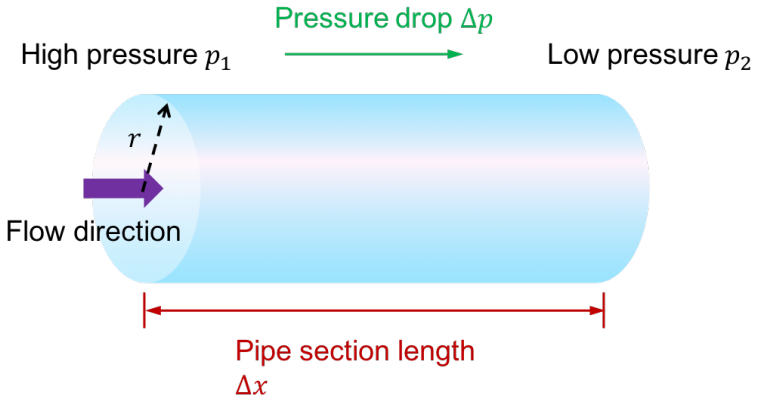

FIGURE 2.14: Illustration of a pressure-driven cylindrical channel. The pressure at point x_1 is higher than the pressure at x_2. The fluid flow in the channel is driven from the left to right due to a positive pressure gradient $\frac{dp}{dx}$ along the flow direction.

We consider the forces on a small volume element of fluid (Fig. 2.15a). The force from the pressure at $x = x_1$ is:

$$F_{p_1} = p_1 \cdot A \tag{2.51}$$

Similarly, the pressure at $x = x_2$, pointing to the opposite direction, is,:

$$F_{p_2} = p_2 \cdot A \tag{2.52}$$

Net flow is caused when the pressure on one side is larger than the other (Fig. 2.15b). The net force F_p on the volume element with which the pressure difference drives the fluid in motion results from the difference between the two forces while the y axis coordinate of the center of the circle cross-section is defined as y = 0 [2], [81]:

$$F_p = F_{p_1} - F_{p_2} = -\pi r^2 \cdot \delta p \tag{2.53}$$

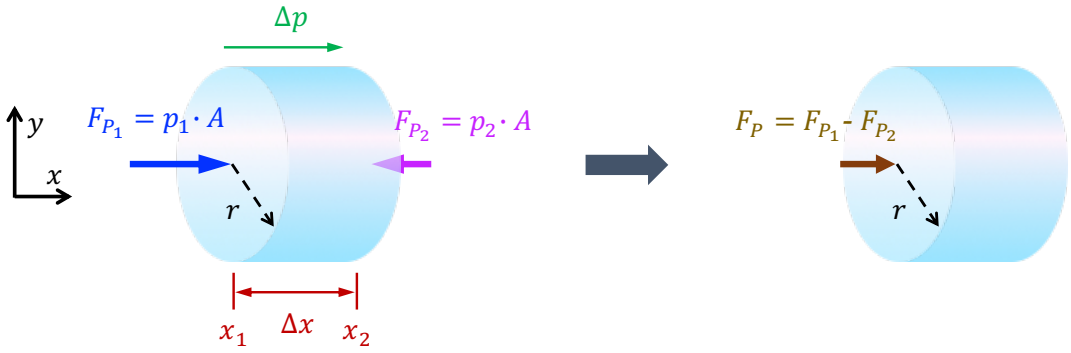

FIGURE 2.15: Pressure forces act on a small volume fluid element. (a) The pressure p_1 at position $x = x_1$ is higher than the pressure p_2 at position $x = x_2$ with $p_2 = p_1 + \delta p$ over the element length dx. (b) The resultant net force F_p is the difference of F_{p_1} and F_{p_2}. Image adapted from [81].

2.3.2 Frictional Force

The fluid flows by the pressure force, with another force acting on it, which is the frictional force. The fluid layer interacting with the wall of the channel experiences an adhesive force resulting in no relative fluid flow speed between the fluid and wall. This is called a no-slip condition. The frictional force between the fluid layers arising from the viscosity of the fluid leads to development of a flow velocity profile. As indicated in Fig. 2.16, the maximum flow velocity occurs at the centerline of the channel and decreases with y to 0 at the wall. In the laminar flow in a channel, the velocity is only considered to be in the direction of the flow ($u_y = 0$) [2], [81].

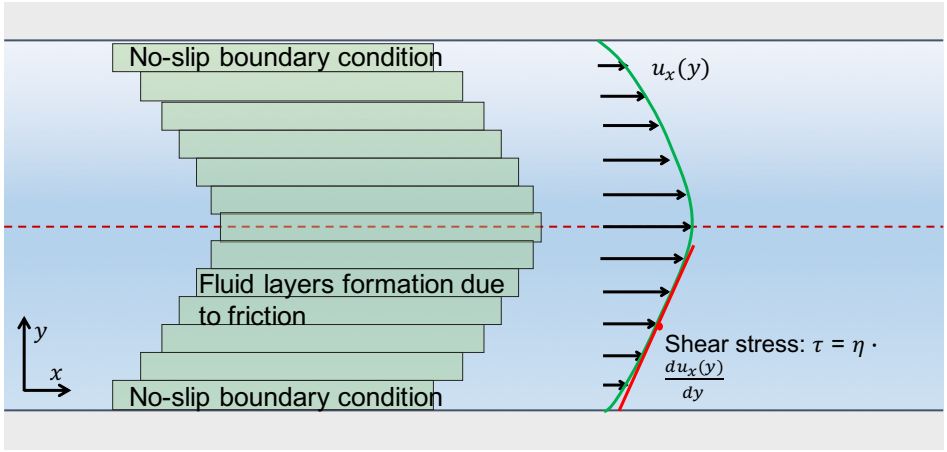

FIGURE 2.16: Friction exists between the fluid and the wall and between each fluid layer, leading to a flow velocity profile with $u_x(0) = u_x(y)_{max}$ at the centerline of the channel and $u_x(r) = 0$. The shear stress of the fluid is proportional to the slope of the flow profile with a factor of the fluid viscosity. Image adapted from [81].

The different velocity in each fluid layer causes a shear force on either side of the

plane. The shear stress can be expressed by the velocity gradient in the y direction, namely by the slope of the velocity profile $du_x(y)/dy$ [2], [81]:

$$\tau = \eta \cdot \frac{du_x(y)}{dy} \tag{2.54}$$

The frictional force F_f is determined by integrating the shear stress τ from Eq. 2.54 over the surface of the cylindrical volume element [2], [81]:

$$F_f = \tau \cdot dA = \eta \frac{du_x(y)}{dy} \cdot 2\pi y \cdot dx \tag{2.55}$$

2.3.3 Hagen-Poiseuille Equation

The cylindrical volume fluid element flows under the balance of the pressure force and the frictional force, the mathematical expression of which are derived so far above. To evaluate the flow velocity profile, we need to combine the two main forces on the system (Fig. 2.17); and solve for u_x [2]:

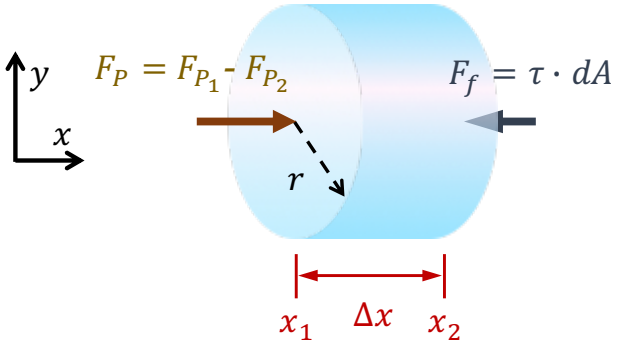

FIGURE 2.17: The fluid flow develops under the balance of the pressure force and the counteracting frictional force. τ is the shear stress, dA is the surface of the cylindrical fluid volume element. Image adapted from [81].

The net force resultant from the two forces decides the flow velocity property. For flows in a steady-state, the flow velocities do not change over time, the inertial term in the Navier-Stokes equation can be eliminated. The balance of the forces can be formulated [2], [81]:

$$F_p - F_f = 0 \tag{2.56}$$

deploying Eq. 2.53 and 2.55 in Eq. 2.56 so that,

$$\frac{du_x(y)}{dy} = -\frac{1}{2\eta}\frac{dp}{dx} \cdot y \tag{2.57}$$

Integrating Eq. 2.57 and applying the no-slip boundary condition $u_x(r) = 0$, the flow velocity profile $u_x(y)$ is obtained [2], [81]:

$$u_x(y) = -\frac{1}{4\eta}\frac{dp}{dx} \cdot y^2 + \frac{1}{4\eta}\frac{dp}{dx} \cdot r^2 \tag{2.58}$$

which indicates a parabolic flow profile of a flow of Newtonian fluid, the viscosity of which is constant, in a channel. This flow profile equation is also known as the *Hagen-Poiseuille equation* (Fig. 2.18). At the centerline of the channel (y = 0), the flow shows the maximum speed $u_{x,max} = -\frac{r^2}{4\eta}\frac{dp}{dx}$ [2], [81].

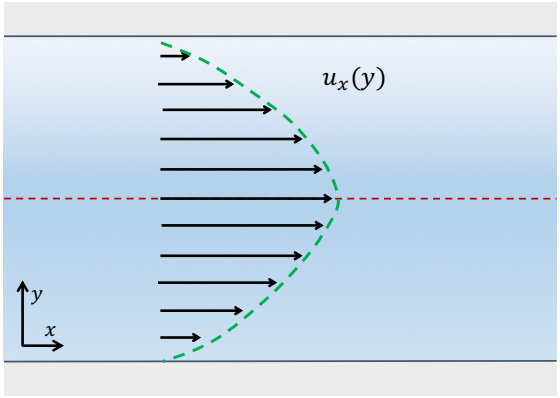

FIGURE 2.18: Parabolic flow profile of the Hagen-Poiseuille flow. The $u_{x,max}$ occurs at the centerline of the channel. Image adapted from [81].

2.3.4 Volume Flow Rate

The volume flow rate can be derived by first dividing the cylindrical channel into shells with an inner radius of y relative to the center axis of the channel and a thickness of an infinitesimal dy. The illustrative geometry is shown in Fig. 2.19 [2], [81].

The surface of the cross-section of the shell dA_s is:

$$dA_s = 2\pi y \cdot dy \tag{2.59}$$

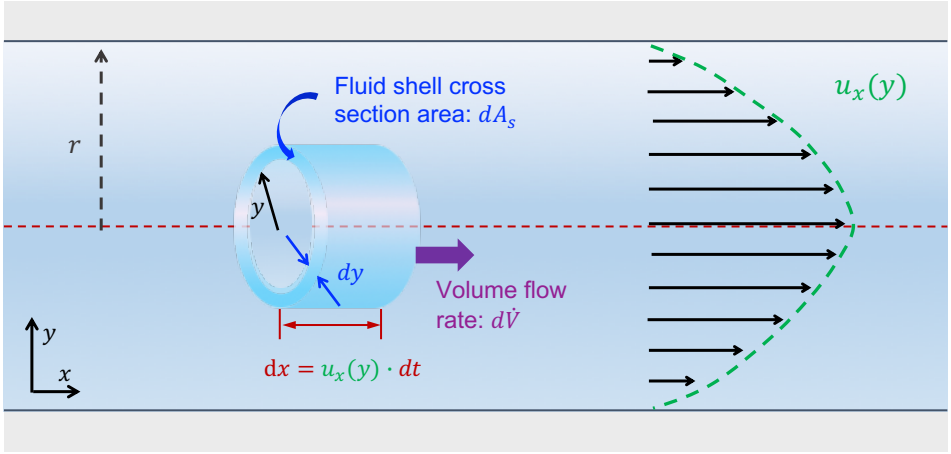

FIGURE 2.19: A fluid shell is taken to analyse the volume flow rate of the flow in a channel. The inner radius of the shell is y, corresponding to a cross-section area dA_s and a flow velocity $u_x(y)$. The distance that the fluid displaces within time dt is dx. Image adapted from [81].

The volume of the fluid shell dV transported within time dt is thus a product of dA_s and the displaced distance by the fluid dx. The speed of the flow at a distance y to the center axis is delivered by Eq. 2.57 [2], [81].

$$dx = u_x(y) \cdot dt \tag{2.60}$$

$$dV = dA_s \cdot dx \tag{2.61}$$

$$dV = -2\pi y \cdot \left[\frac{1}{4\eta}\frac{dp}{dx} \cdot y^2 + \frac{1}{4\eta}\frac{dp}{dx} \cdot r^2\right] \cdot dy \cdot dt \tag{2.62}$$

The flow rate is calculated by taking the transported fluid volume over the time range:

$$d\dot{V} = \frac{dV}{dt} \tag{2.63}$$

$$d\dot{V} = -2\pi y \cdot \left[\frac{1}{4\eta}\frac{dp}{dx} \cdot y^2 + \frac{1}{4\eta}\frac{dp}{dx} \cdot r^2\right] \cdot dy \tag{2.64}$$

Integrating Eq. 2.64 from $y = 0$ to $y = r$ in terms of y gives the volume flow rate in the entire channel [2], [81]:

$$\dot{V} = \int_0^R -2\pi y \cdot \left[\frac{1}{4\eta}\frac{dp}{dx} \cdot y^2 - \frac{1}{4\eta}\frac{dp}{dx} \cdot r^2\right] \cdot dy \tag{2.65}$$

$$\dot{V} = -\frac{\pi r^4}{8\eta}\frac{dp}{dx} \tag{2.66}$$

The flow rate through the channel is proportional to the pressure gradient in the flow direction and the fourth power of the radius.

2.3.5 Pressure Drop

To drive the fluid flow, a pressure gradient $\frac{dp}{dx}$ is required. To achieve a desired volume flow rate, the required gradient is given as [2], [81]:

$$\frac{dp}{dx} = -\frac{8\eta}{\pi r^4}\dot{V} \tag{2.67}$$

The pressure drop Δp_d over a channel section with the length L is then:

$$\Delta p_d = -\frac{8\eta \cdot L}{\pi r^4}\dot{V} \tag{2.68}$$

The pressure gradient that the fluid takes to achieve a volume flow rate $\dot{V}$ is the same as the pressure loss that the fluid experiences. When reducing the channel radius by a factor of 2, the pressure gradient required to pump the same volume flow rate increases by $2^4 = 16$, as does the mechanical power required, since the mechanical power P is proportional to the pressure gradient with the following equation [2], [81]:

$$P = \Delta p_d \cdot \dot{V} \tag{2.69}$$

$$P = -\frac{8\eta \cdot L}{\pi r^4}\dot{V}^2 \tag{2.70}$$

2.3.6 Flow in Rectangular Cross-Section Channel

Although the 2D analysis for rectangular cross-section microchannel is complex due to the partial differential equation (PDE), the analytical modelling and solution are still needed since the microchannels are usually fabricated with rectangular cross-section [78], [79], [82], [83]. One approach is to model the flow numerically [84]. Another is to seek an easier mathematical solution. In all of the methods, eigenfunction expansion

is considered to be a simple method of solving the partial differential equation [78], [85].

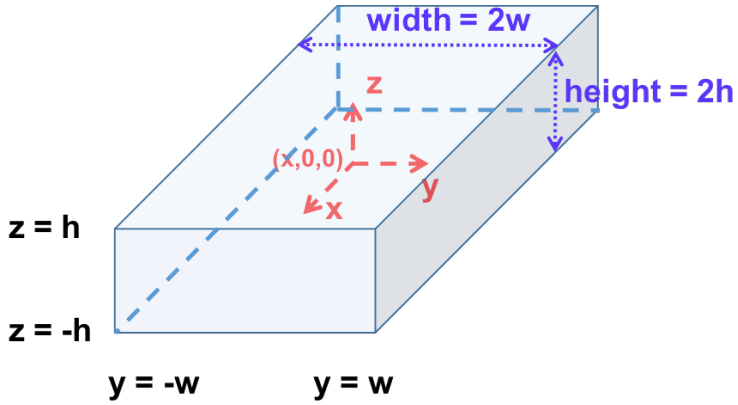

FIGURE 2.20: Schematic illustration of the coordinate system for the 2D analysis of a rectangular cross-section microchannel. At each cross-section plane, the center point of the rectangle is defined with y = 0, z = 0. The width, height and length of the microchannel is 2w, 2h and L, respectively.

The stokes equation describing the flow is formulated as [78]:

$$\frac{\partial^2 u}{\partial y^2} + \frac{\partial^2 u}{\partial z^2} = -\frac{\Delta p}{\mu L} \tag{2.71}$$

where u is the fluid velocity, μ is the dynamic viscosity of the fluid. The boundary condition of the microchannel is:

$$u(x,0,z) = 0; \quad u(x,2w,z) = 0 \tag{2.72}$$

$$u(x,y,0) = 0; \quad u(x,y,2h) = 0 \tag{2.73}$$

In the eigenfunction expansion method, if a function ψ satisfies $\nabla^2\psi = \lambda \cdot \psi$ with the boundary condition 2.72, 2.73, where ∇^2 is the Laplacian operator, λ the eigenvalue, it's called the eigenfunction. A typical 2D form of the solution can be written as [78], [85]:

$$u(y,z) = \sum_{n=0}^{\infty} A_n(y) \cos[\frac{(2n+1)\pi z}{2h}] \tag{2.74}$$

The final 2D analytical solution for the rectangular cross-section microchannel is [78], [85], [86]:

$$u(y,z) = \frac{16\Delta p h^2}{\mu L \pi^3} \sum_{n=0}^{\infty} \frac{(-1)^n}{(2n+1)^3} [1 - \frac{\cosh[\frac{(2n+1)\pi y}{2h}]}{\cosh[\frac{(2n+1)\pi w}{2h}]}] \cos[\frac{(2n+1)\pi z}{2h}] \quad (2.75)$$

Simplifying the term only relates to z at the right-hand side of Eq. 2.75, Eq. 2.75 can be reshaped in the form:

$$u(y,z) = \frac{\Delta p}{2\mu L}(1 - \frac{z^2}{h^2}) - \frac{16\Delta p h^2}{\mu L \pi^3} \sum_{n=0}^{\infty} \frac{(-1)^n}{(2n+1)^3} \frac{\cosh[\frac{(2n+1)\pi y}{2h}]}{\cosh[\frac{(2n+1)\pi w}{2h}]} \cos[\frac{(2n+1)\pi z}{2h}] \quad (2.76)$$

The first term at the right side of Eq. 2.76 $\frac{\Delta p}{2\mu L}(1 - \frac{z^2}{h^2})$ delivers the fluid profile equation along the z-direction, which shows a parabolic profile.

The volumetric flow rate Q is calculated by:

$$Q = \int dy\, dz\, u(y,z) \quad (2.77)$$

An analytical solution can hardly be found. Instead, an approximation form is given by [86].

$$Q \approx [1 - 0.630\frac{h}{w}]\frac{4h^3 w}{3\mu L}\Delta p, \quad h < w \quad (2.78)$$

Chapter 3

Spontaneous Symmetry Breaking Chemical Micromotors

This chapter is based on and contains excerpts and figures from the article "Chemical micromotors self-assemble and self-propel by spontaneous symmetry breaking" [87]. Contributions of coauthors are indicated.

In this chapter, we present a unique novel route to form reconfigurable chemical motors by spontaneous symmetry breaking of the chemically active colloids in the system when mixed with passive colloids.

3.1 Motivation

Artificial microswimmers show great potential to address a wide range of problems. These range from fundamental questions related to the understanding of the self- organizational behavior of the living world to important applications like, the development of new materials with self-healing and reconfigurable features. Microswimmers can act as autonomous carriers or motors to localize, pick-up and deliver nano- and microscopic objects[88], [89], *e.g.*, in novel lab-on-a-chip microfluidic devices. I have introduced different types of artificial microswimmers in previous sections, the fabrication of which is summarized in table 3.1. These techniques enable the symmetry breaking of a microstructure. One type of artificial microswimmers are chemically active colloids that operate by converting chemical energy into translational motion via a surface chemical reaction. There an asymmetric distribution of chemical reactant or product around the colloid drives the self-phoretic flows that cause the colloid to swim. Symmetry breaking is essential for swimming. The conventional way to attain a symmetry-broken structure is to fabricate Janus colloids with two opposite surfaces of different chemical activity. However, the limitations of the microscale fabrication techniques prevent the large scale

production of these chemical motors. It is interesting to explore novel ways to break the symmetry to enable larger scale applications.

Since the chemical gradient surrounds an isotropic chemically active particle, it should in principle be possible for a passive isotropic particle to experience this chemical gradient, which can lead to phoretic interactions between it and the active particle. If the interaction is atrractive, then the active and passive particle can form a dimer. The structure of the dimer is then no longer isotropic but has an asymmetric conformation (one active and one passive side). The dimer is asymmetric and thus able to self propel under certain conditions. In this way, fabrication techniques are no longer needed to obtain microswimmers. Chemical micromotors can be fabricated with this spontaneous symmetry breaking mechanism on a larger scale and directly in a fluid.

TABLE 3.1: Symmetry-broken structure and the fabrication method.

	Size	**Fabrication method**
Janus particles	0.1-10 μm	Thin film sputtering, PVD
Chiral helixes	2 μm (length) 250 nm (width)	GLAD deposition

The active colloids used for the spontaneous formation of dimers are photocatalytic microspheres that form a uniform chemical gradient around the surface by decomposing the fuel when illuminated with UV light. They are responsive to the light with a wavelength of 365 nm in H_2O_2 solution. The symmetric chemical distribution due to the isotropic shape of the colloids keep the isolated microspheres immotile. However, when a passive particle enters the region of the catalytically active colloid, the phoretic interaction between the active and the passive particles leads to the formation of a dimer. The dimer shows a symmetry-broken structure and starts to swim in the aqueous medium. The active colloids are photochemically active. The swimming of the dimers can be dynamically fully controlled with an external UV light source. When the illumination is on, the active dimers remain stable and motile until the light is turned off, when they fall apart. The sequence of light driven dimer formation is schematically shown in Fig. 3.1.

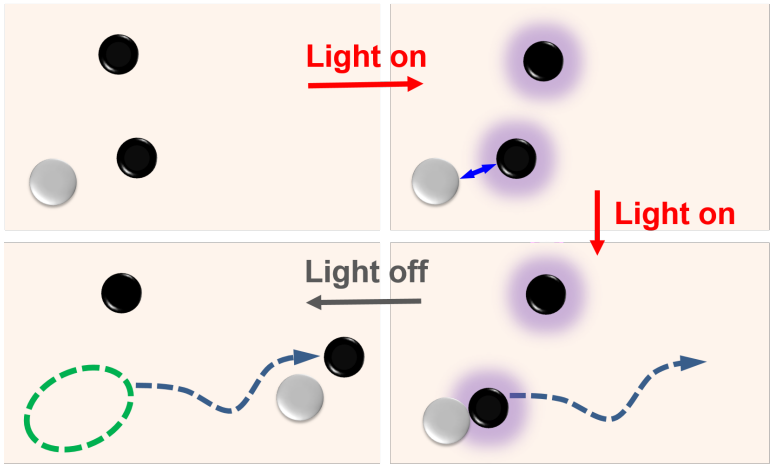

FIGURE 3.1: Schematic illustration of self-assembled motors which can self-propel under light illumination. Black: chemically active particles, white: passive particles. Image taken from [87].

3.2 Dimer Formation of Isotropic SiO_2 and TiO_2 Colloids

3.2.1 Dimer Formation

The isotropic active TiO_2 and passive SiO_2 microspheres are purchased from EPRUI Biotech Co.. The diameter of TiO_2 particles is 1.2 μm and of SiO_2 is 2 μm in the first experiments. The TiO_2 particles are in the anatase state and show photoactivity in a dilute H_2O_2 solution. The SEM images of both particles are shown in Fig. 3.2 and 3.3.

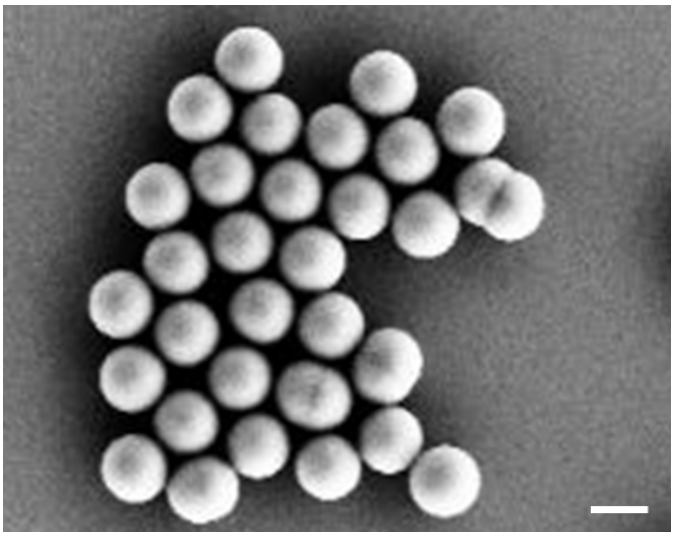

FIGURE 3.2: SEM image of SiO_2 microspheres of 2 μm diameter. Image taken from [87].

Active particles are mixed with passive particles in a 2.5 % aqueous H_2O_2 solution, the pH of which was adjusted with $1x10^{-3}M$ Tetramethylammonium hydroxide

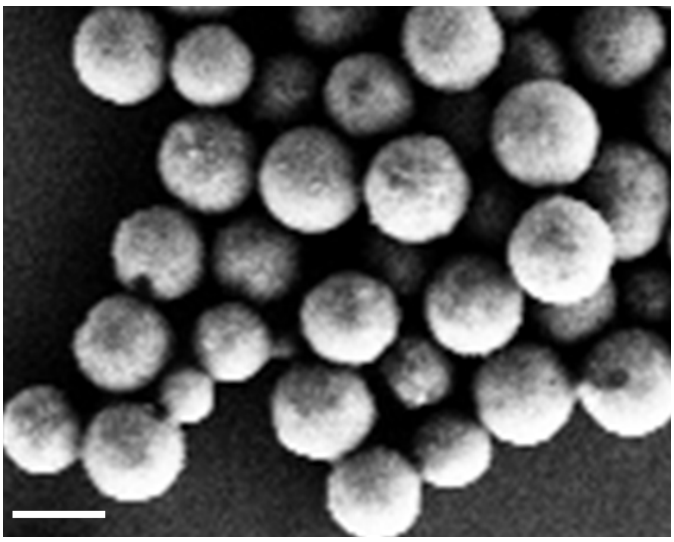

FIGURE 3.3: SEM image of TiO_2 microspheres of 1.2 μm diameter. Image taken from [87].

(TMAH) to approximately neutral. This mixture was prepared shortly before use. 35 μl of the mixture was pipetted onto a plasma cleaned cover glass and covered with a cover slip on top. The sample was transferred to the sample holder of an inverted microscope (Zeiss Axio Observer). White light illuminates from top through the sample, objective at the bottom and imaged by a camera (Andor Zyla 5.5) connected to the observation path. A UV light emitting diode was mounted through another light path through the bottom slide. The UV light travels through a UV dichroic mirror in the filter cube sitting in middle of the light path and objective lens and reaches the sample from the bottom. The maximum UV intensity was measured by a photometer and was 320 mW/cm^2 in the sample plane. The videos were recorded using a 63x objective lens with a framerate of 10 fps. The dimers were tracked for at least 30 s. For each dimer formation experiment, both UV off and UV on states were captured for comparison.

One factor that determines the degree of dimer formation is the average separation of the particles, which can be tuned by changing the particle density. In our experiment, particles assemble to a dimer in a time of approximately 3 s at a particle density of 2 %. At higher densities, more than one passive particle will on average be attached to the active particles and clusters will form, as shown in Fig. 3.4.

If the size of passive particle is more than double the size of active particle and meanwhile the passive to active ratio is lower than 1:3, more active particles will be attached to one passive particle and undertake no symmetry breaking like can be seen in Fig. 3.5.

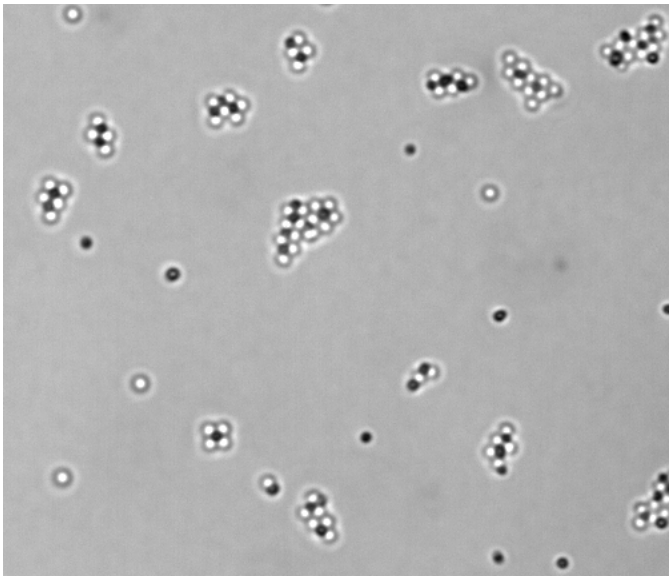

FIGURE 3.4: Cluster formation with too high passive to active particle ratio of 2:1. The diameters of the black TiO_2 particles are 1.2 μm.

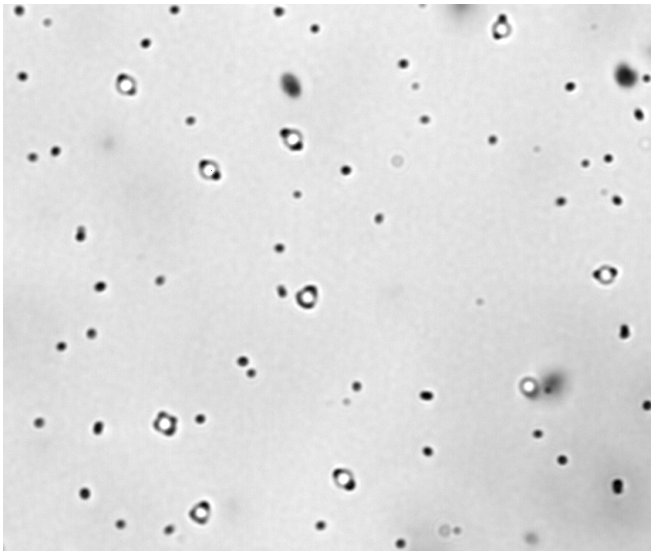

FIGURE 3.5: More active particles on one passive particle with no symmetry breaking with too low passive to active particle ratio of 1:6. The diameters of the black TiO_2 particles are 1.2 μm.

A passive to active particle ratio is optimised for the dimer assembly experiment and an optimum size ratio of 1:3 was found. More discussion on the particle ratio can be found in Section 3.6. The particles are allowed to sediment in the chamber for several minutes. Under no UV illumination, both the colloids remain inactive and exhibit normal Brownian motion. When the UV-light (365 nm) is turned on, the photocatalytic decomposition of H_2O_2 at the TiO_2 surface makes the TiO_2 colloids chemically active

[66], [67], [90].

$$2H_2O_2 \rightarrow O_2 + 2H_2O \tag{3.1}$$

Most active colloids remain immotile. However, those close to the passive silica colloids exhibit an attractive interaction to each other and therefore, join to form dimers. Fig. 3.6b shows such dimers within a few seconds after the light is turned on. Once the dimers are formed, the symmetry is broken and the condition for a microswimmer is satisfied and self-diffusiophoresis is obeserved (see Fig. 3.6c). The average speed of dimers was measured to be 2.2 μm/s average over 15 particles. The single active particle highlighted by a red dashed circle is tracked for the same period of time. The trajectory represents Brownian motion with no propulsion. When one switches off the UV light (Fig. 3.6d), the dimer instantly separates into an active and a passive particle that show Brownian motion. The formation and separation process is reversible with the control of light.

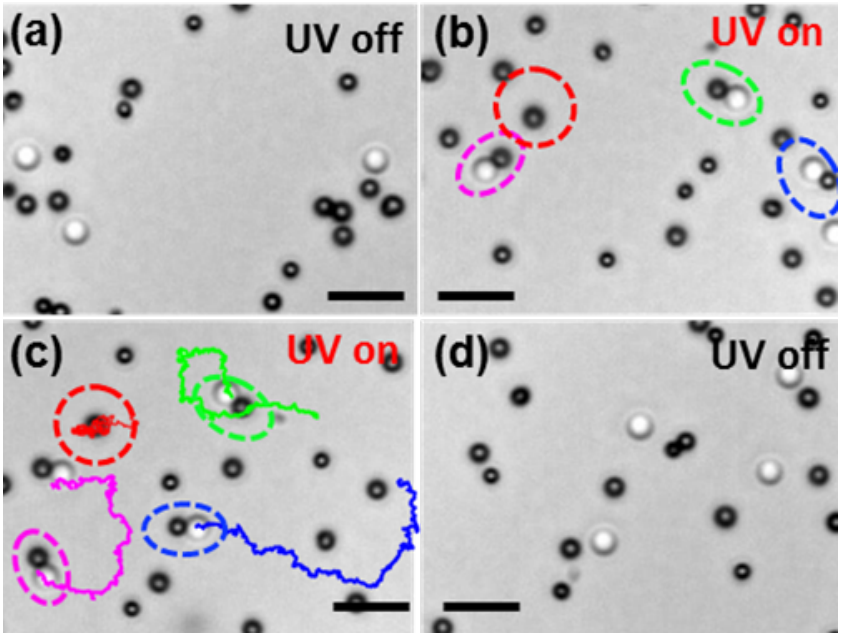

FIGURE 3.6: Dimer formation of passive SiO_2 (white) and active TiO_2 (black) colloids. The trajectories are taken for 28 s. The scale bar indicates a length of 5 μm. Image taken from [87].

The speed of the dimer propulsion can be fully controlled by adjusting the UV light intensity. We measured the speed of at least 6 dimers over 30 s under different UV illumination intensity. The speed is averaged over all the tracked dimers at each intensity and is plotted with standard deviation against the UV intensity as a percentage to the

maximum light intensity in Fig. 3.7.

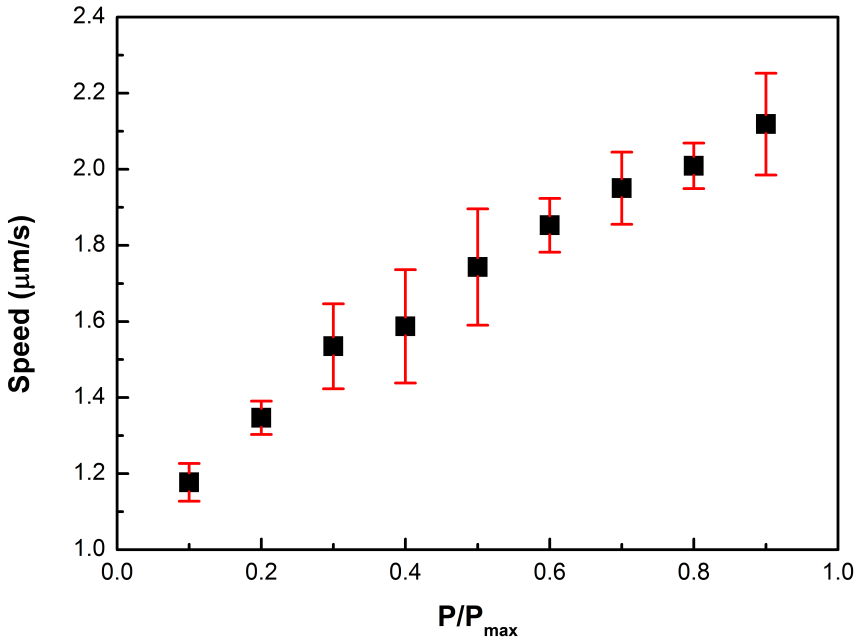

FIGURE 3.7: Dependence of the propulsion speed of dimers on the UV light intensity. P is the applied UV light power intensity. P_{max} is the maximum light power intensity used in the experiment, which is 320 mW/cm^2. Image taken from [87].

3.2.2 Mechanism of Dimer Formation

The formation of the dimers observed in the experiments may be explained in the context of diffusiophoresis [58], [91], [92]. Control experiments are conducted to rule out thermophoresis and other optical effects. A mixture of passive SiO_2 particles and active TiO_2 particles with a ratio of 1:3 is prepared except that the 2.5 % H_2O_2 solution and TMAH is replaced by pure water. This mixture is transferred to a sample cell with a height of 300 μm shortly before observation. Under same microscopy and illumination conditions as in section 3.2.1, the particles are observed. It can be seen that the particles remain immotile and perform purely Brownian motion in water under UV illumination. Snapshots are taken and shown in Fig. 3.8.

Now, the role of TMAH was examined. A control experiment to test if TMAH is photocatalytically active was done in [90]. SiO_2/TiO_2 Janus particles were immersed in TMAH and illuminated. No activity is obeserved. Only when TMAH and H_2O_2 is

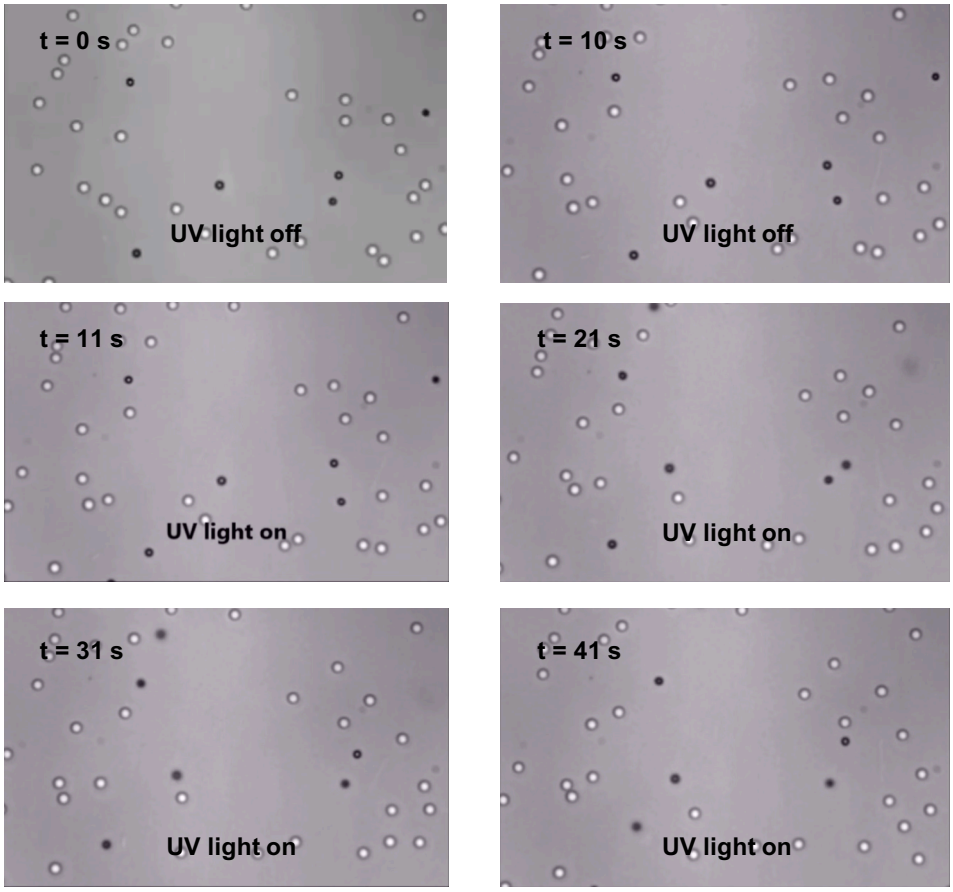

FIGURE 3.8: No dimer is formed in H_2O (instead of H_2O_2) with UV illumination on for 30s.

added and the colloids are illuminated with UV light is the dimer formation observed.

Only by adding the TMAH, is the phoretic interaction direction reversed and the attachment between passive and active particles is observed. The understanding of this phenomenon is that the phoretic mobility of the particles are changed under different pH values [90]. TMAH does not only change the direction of interaction between passive and active particles, but also reverses the direction of propulsion. In Fig. 3.9, the last frame of tracked motion of SiO_2/TiO_2 Janus particles in H_2O_2 without TMAH (a) and of SiO_2/TiO_2 dimers in H_2O_2 with the presence of TMAH (b) are shown together. It is seen that the Janus particles propel towards the white SiO_2 end while the dimer motion is led by the black TiO_2 end.

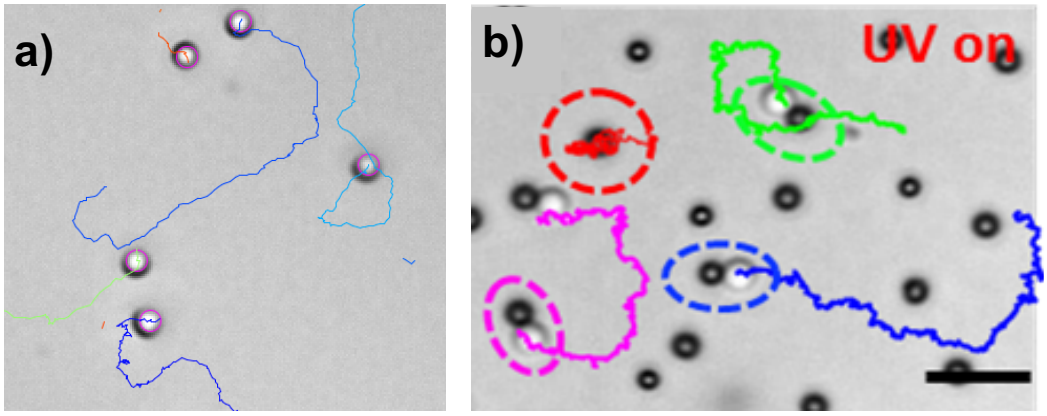

FIGURE 3.9: The propulsion direction is reversed by adding TMAH to the fuel. Last frame of the tracked trajectories of (a) Janus SiO_2/TiO_2 particles propels facing the SiO_2 half in H_2O_2 without TMAH. (b) SiO_2/TiO_2 dimers facing the TiO_2 half in H_2O_2 with TMAH. Images taken from [90][87].

To examine the dimer formation is due to self-diffusiophoresis or self-electrophoresis, additional experiments were executed. A series of samples with active SiO_2/TiO_2 Janus particles was prepared by additionally dissolving a concentration series of NaCl 10^{-5} mM, 10^{-4} mM, 10^{-3} mM, 10^{-2} mM, 10^{-1} mM, and 10^{0} mM. Fig, 3.10 shows the average speed of the Janus particle as a function of the NaCl concentration.

By adding salt up to a concentration of 10^{-1} mM, the propulsion speed of Janus particles almost remain at the same level, a noticeable reduction in particle speed occurs only at high salt concentration of 1 mM [93].

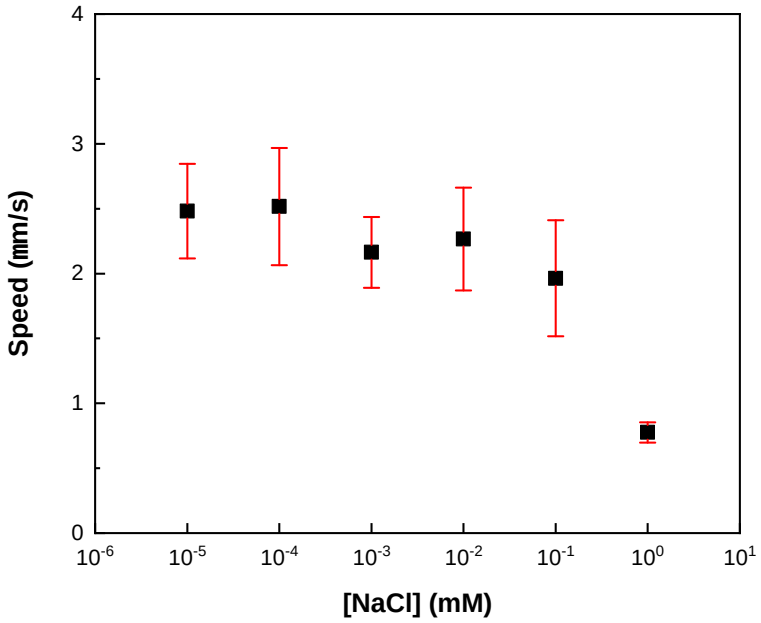

FIGURE 3.10: Average speed of 2 μm SiO_2/TiO_2 Janus particles in H_2O_2 with different concentration of NaCl to evaluate the ionic effect on the system. Image taken from [87].

In a bimetallic Janus system, the electrophoretic motion is induced by the electric field generated by an ionic current leading to a particle propulsion with a speed [15]:

$$v = \mu_E E \tag{3.2}$$

where μ_E is the electrophoretic mobility, E is the electric field. The generated electric field in the above equation correlates to the current density j, and the conductivity of the solution K:

$$E = j/K \tag{3.3}$$

while the expression of a particle of electrophoretic mobility is:

$$\mu_E \propto \zeta\epsilon/\eta \tag{3.4}$$

where ζ is the zeta potential, ϵ is the dielectric constant, η is the dynamic viscosity of the dispersion medium. Eq. 3.2, 3.3, 3.4 give a scaling relationship for the speed v where the prefactor will be decided with more geometric details of the current flow [94]:

$$v \propto \frac{j\zeta\epsilon}{\eta K} \tag{3.5}$$

The speed is inversely proportional to the conductivity, which does not match the case shown in Fig. 3.10. We can therefore rule out electrophoretic interactions in our experiment, and confirm that diffuiophoresis is the cause of the dimer formation.

3.3 Dimer with Different Passive Particle Size

The dimer system is further investigated by changing the size of the passive SiO_2 particles to identify the optimal size ratio or combination for propulsion. We kept the size of active TiO_2 particles constant, and only varied the size of the SiO_2 particles from 300 nm, 500 nm, 1 μm, 1.5 μm, 2 μm, 3.18 μm to 4 μm. Some experimental details and observations are summarised in Table 3.2. The dimer formation is a combined result of phoretic interaction and Brownian motion of each isotropic particle. When the phoretic interaction is not dominating but comparable to the Brownian diffusivity, the dimer formed is not always that stable and can fall apart and reform again. The speed is the average over several dimers at their stable state.

TABLE 3.2: Experimental parameters and observation for different mean passive particle sizes determined from an average of approx. 10 particles.

	300 nm	500 nm	1 μm	1.5 μm	2.1 μm	3.2 μm	4 μm
Objective	100x	63x	63x	63x	63x	63x	63x
Dimer formation	no	yes	yes	yes	yes	yes	no
Dimer stability	–	middle	high	high	high	high	–
SiO_2 formed dimer [%]	–	50	67.3	72	85.7	40	–
Speed of formed dimer $[\mu m/s]$	–	2.14 ± 0.14	4.18 ± 0.40	4.48 ± 0.47	2.96 ± 0.34	1.35 ± 0.20	–

With too small (300 nm) and too large (4 μm) passive particles, no attachment between active and passive particles was monitored. For 300 nm particle, the Brownian motion dominates over phoretic interaction, while for 4 μm particle, the phoretic force

is not high enough to drive the passive particle out of its equilibrium state. In the size range for passive particles of 500 nm to 3.2 μm, a dimer is formed. The images of the formed dimer with different size of SiO_2 particles are shown in Fig. 3.11.

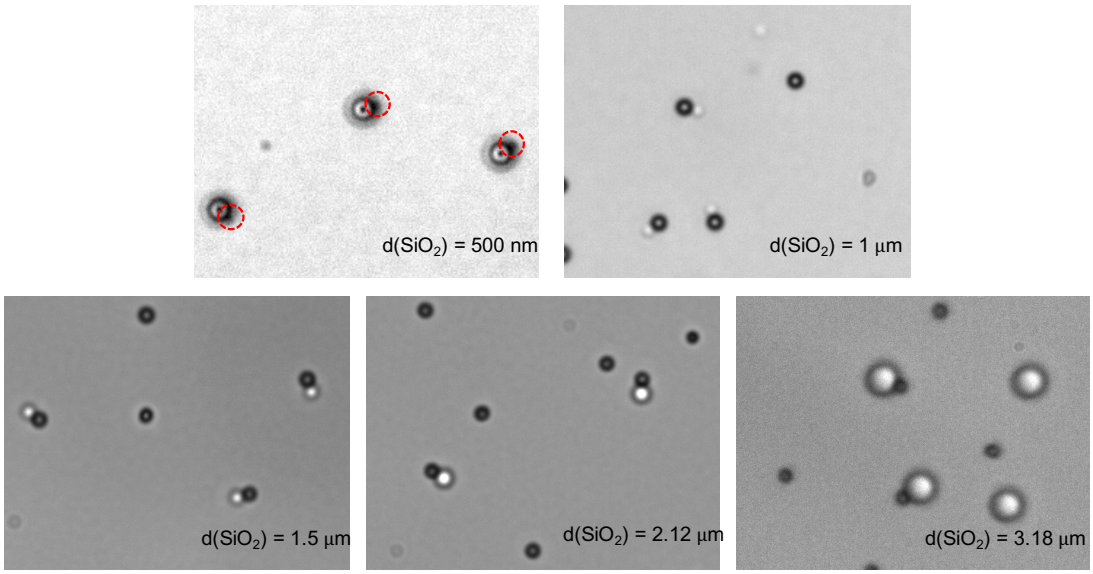

FIGURE 3.11: Images of formed dimers with different sizes of SiO_2 particles. Red dashed circle in the first image shows where the 500 nm SiO_2 particle is.

The dimer forming ratio increases from 500 nm to 2.12 μm, and drops from 2.12 μm to 3.18 μm. The propulsion speed reaches maximum with a particle size of 1.5 μm. Both relationships are presented in Fig. 3.12 and 3.13. The dimer consisting of an active particle and a small sized passive particle, the disturbance that the passive particle introduces to the chemical distribution is weaker than with a larger passive particle. In other words, the chemical gradient that causes the motion of the dimer with too small passive particles is lower than with a larger particle and leads to a slower motion of the dimer. When the passive particle is much larger than the active particle, it behaves like a wall to the small sized active particle and thus slowed down the propulsion of the dimer.

3.4 Dimer Formation of PS and TiO_2 Particles

The mechanism of dimer formation and propulsion is explained as self-diffusiophoresis in section 3.2.2. Therefore, this scheme is not a specific case to the SiO_2/TiO_2 system. It can be generalized to other types of passive particles. We tried 2 μm polystyrene (PS)/TiO_2 system with no change of other conditions, see Fig. 3.14.

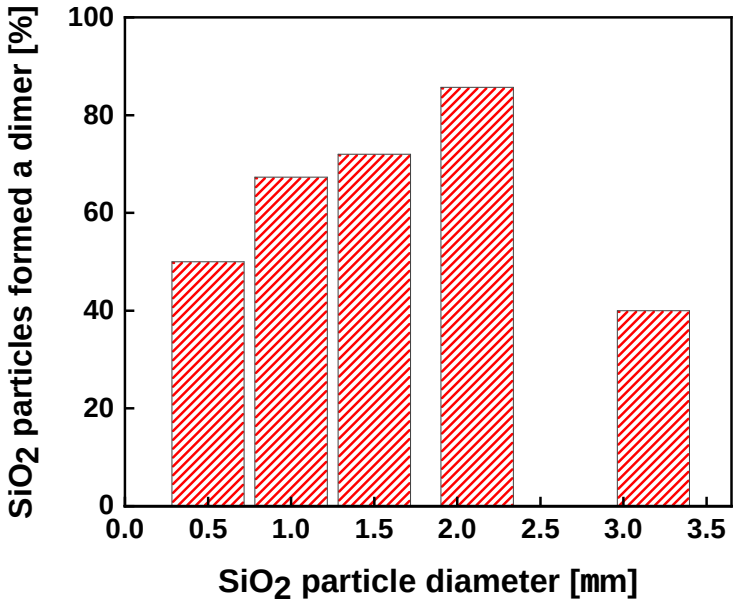

FIGURE 3.12: Dimer forming ratio out of passive SiO_2 particles under UV illumination after 100 s as a function of SiO_2 particle size.

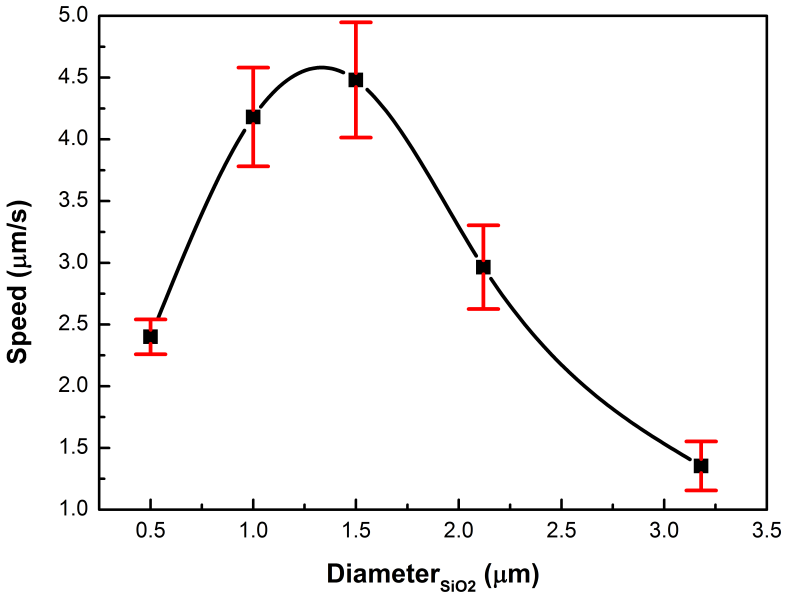

FIGURE 3.13: Propulsion speed of dimer as a function of SiO_2 particle size.

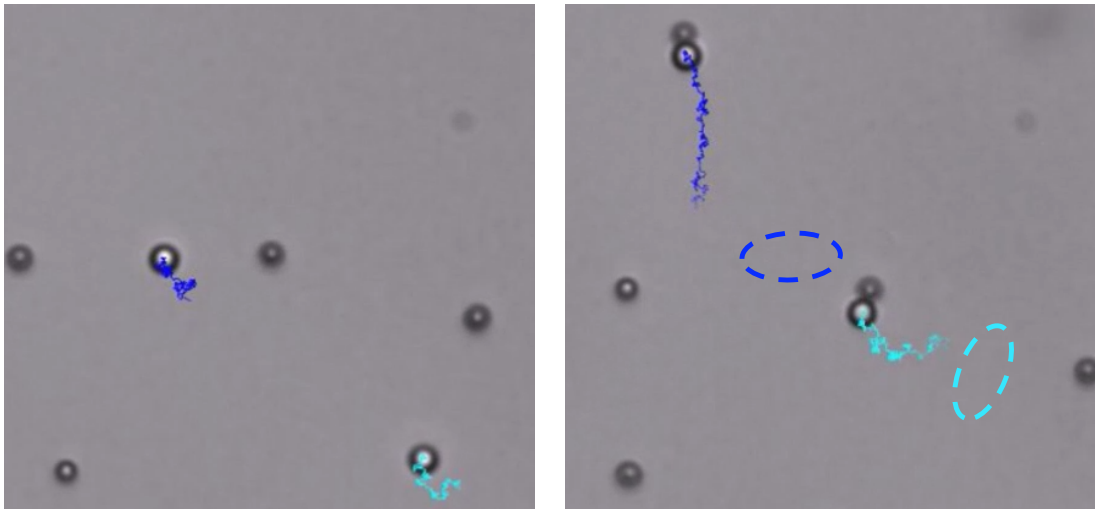

FIGURE 3.14: Dimers formed with PS and TiO_2. Left: Brownian motion of PS particles when UV is off for 15 s. Right: Active motion of dimer when UV is on for 21 s. Dashed circle marked the position where the dimer is initially formed.

The active and passive colloids form heterodimers and conduct active motion under UV illumination. We tracked the PS/TiO_2 dimer for more than 20 s, and averaged over all the dimers. The average speed is compared with the average speed of dimer consists of SiO_2 and TiO_2 with the same size of passive particle in Fig. 3.15. It is noticeable that the speed of the PS/TiO_2 is slower than the SiO_2/TiO_2 dimer. It can be understood from two aspects. First possibility could be the different phoretic mobility of the dimers due to the different materials. The other point could be that the PS particle in the dimer is not at the same plane as the TiO_2 particle due to the lower density of PS, so that the chemical gradient direction is not exact along the propulsion orientation of the dimer, while the propulsion orientaion of the dimer is constrained by the wall. Both potential reasons lead to the slower motion speed of the PS/TiO_2 compared to the SiO_2/TiO_2 dimer.

3.5 Theoretical Modelling of the Dimer Formation and Propulsion

In section 3.2.2, we explained the formation of the dimers with a diffusiophoretic mechanism. Based on the experimental observed diffusiophoretic mechanism, mesoscopic simulations were conducted by Prabha Chuphal, Snigdha Thakur and Shang Yik Reigh. A particle-based simulation method combining molecular dynamics (MD) and multiparticle collision dynamics (MPCD) for the interaction with the fluid [95] is used to map

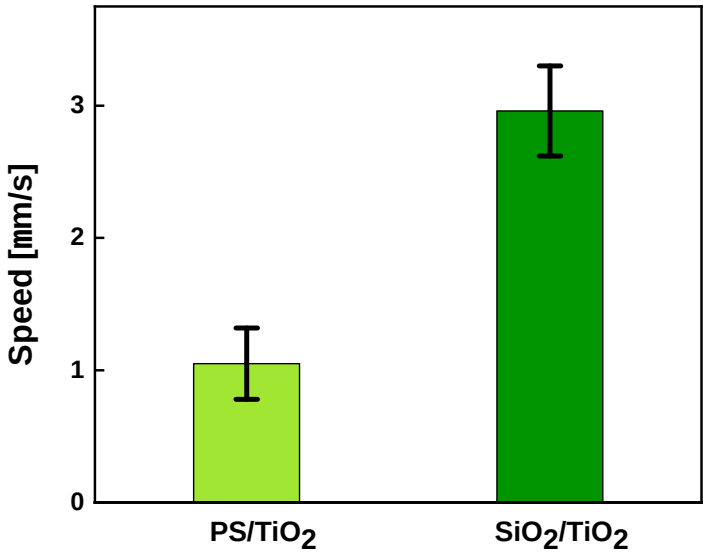

FIGURE 3.15: Speed comparison of PS/TiO_2 and SiO_2/TiO_2 dimers propulsion under same condition. The sizes of the PS and SiO_2 particles are about 2 μm.

the motion, the hydrodynamic interactions and to capture the thermal fluctuations. In what follows the simulation model is described, a catalytically active sphere (S_a, TiO_2) with a radius R_a is separated with a passive sphere (S_p, SiO_2) with radius R_p with distance L. The solution around the spheres contains two catagories of solutes, reactant A H_2O_2 and product B (*e.g.* O_2, H_2). The reaction takes place on the active catalytic half with a reaction rate constant:

$$\mathrm{A} \xrightarrow{S_a} \mathrm{B} \tag{3.6}$$

A repulsive Lennard-Jones (LJ) potential is applied to describe the interactions between the spheres and the fluid (A and B).

$$U = 4\varepsilon[(\sigma/r)^{12} - (\sigma/r)^6] + \varepsilon, \qquad r < 2^{1/6}\sigma \tag{3.7}$$

$$U = 0, \qquad r \geq 2^{1/6}\sigma \tag{3.8}$$

Where ε is the parameter of interaction energy and σ is the distance. The size of the passive particle is twice as the active particle corresponding with the experimental setup.

The results of the simulation show that passive particles are attracted by diffusiophresis and active particles repel each other. Snapshots are taken from the simulation with and without UV illumination and shown in Fig. 3.16. The chemical reaction $A \rightarrow B$ is triggered by UV light at the surface of the catalytically active particles, which leads to a concentration field distribution. A passive particle nearby senses the concentration field and moves towards the active particle. Meanwhile, the active particle moved towards the passive particle due to a flow drag induced by the passive particle [96]. When the UV light is off, the active and passive particles show Brownian motion. Once the light is on, they start to approach each other (Fig. 3.16a) and finally form a dimer (Fig. 3.16b). The formed dimer is stable, and can propel for a long time and distance towards the active end (Fig. 3.16c). Switching off the UV, the particles fall apart and revert back to the Brownian state (Fig. 3.16d).

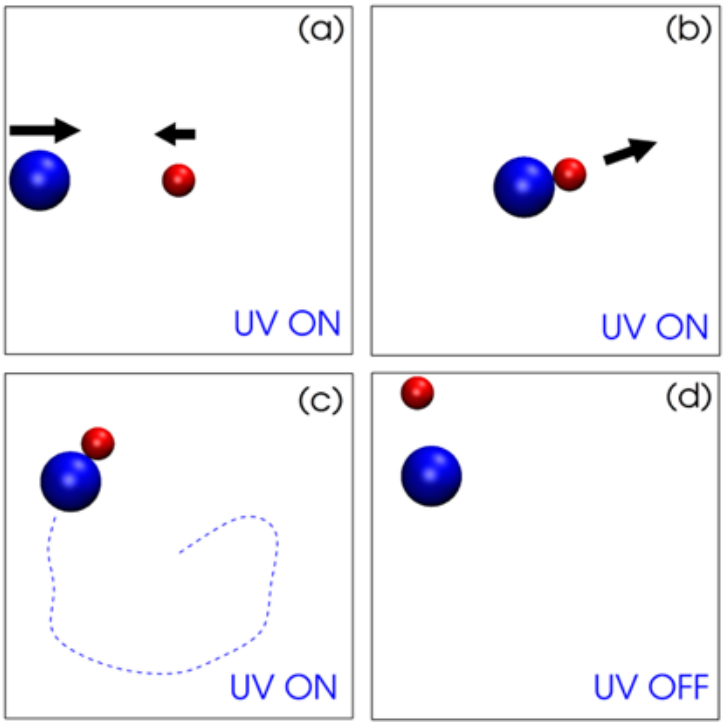

FIGURE 3.16: Simulation snapshots showing the formation and propulsion of the dimer. Red spheres: TiO_2, blue spheres: SiO_2. (a) Active and passive particles approach each other when UV is on. (b) The dimer forms. (c) The dimer propels over a trajectory which is marked with dashed line. (d) When the light is switched off, the dimer split into two particles which conduct Brownian motion. Image taken from [87].

The resulting concentration field of B converted from A which in turn attracts passive particles nearby is illustrated in Fig. 3.17. The computed quantities are dimensionless.

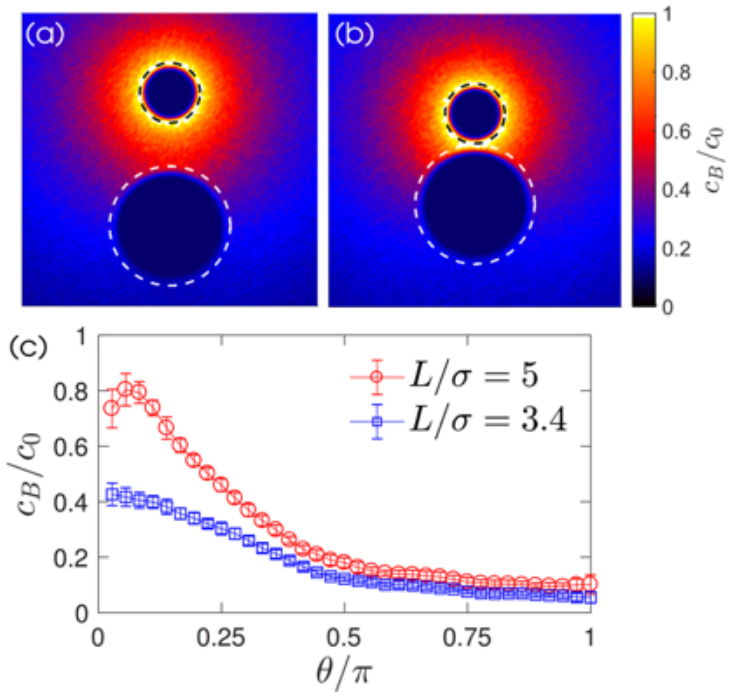

FIGURE 3.17: Normalized concentration field c_B/c_0 for the two particles at a separation distance (a) $L/\sigma = 5$ and for (b) $L/\sigma = 3.4$ (dimer). Black and white dashed line represent the size of the active and passive particles with a radius $R_a = 2^{1/6}\sigma$ and $R_P = 2^{1/6}(2\sigma)$, respectively. (c) c_B/c_0 along the polar angle θ at the surface of the passive particle. The polar angle starts from the axisymmetric axis, the line joining the center of two particles; $\theta = 0$ indicates the position near the active particle. Image taken from [87].

When the passive particle sits close to an active particle, the chemical gradient generates a slip flow around the passive particles. The system follows the conservation of momentum since there is no applied external force and propels oppositely to the slip flow direction. The motion of the passive particle towards the active particle changes the flow dynamically that a part of the flow is directed from the active to the passive particles which drags the active particle to the passive particle at the same time. The two particles appear to approach each other in the induced flow field (see Fig. 3.18 from reference [96]) and finally form a dimer.

When two active and passive particles are approaching, the velocity is altered at different separation distances. The velocity at different separation distances is an important index to study the dimer formation process, since it is a reflection and result of the combined effect of the chemical gradient distribution and the induced hydrodynamic flow. We sampled and averaged the approaching velocity as a function of separation distance over 10 dimer formation processes from experimental data and plotted with the computed velocity at each position along the approaching trajectory from simulation in Fig. 3.19.

A same trend is found in both experimental and simulation results. After the formation of the dimer, the particles propel with a constant average velocity V_d since the concentration gradients remain stable during propulsion. A related separation distance-time plot with both experimental and simulation data is shown in Fig. 3.20.

3.6 Feasibility and Stability of the System

As in subsection 3.2.1 discussed, the dimer formation is affected by the average separation of the particles, which is set by adjusting the particle density. When the ratio of passive to active particles is higher than 1:3, more passive particles bind to one active particle and thus form clusters. The clusters show different swimming behaviour than dimers with their different structures. They are more symmetric and less motile. With an optimised particle density and particle ratio, the dimer will be surrounded by more active particles. Once a dimer swims towards an active particle, a repulsion interaction from the chemical gradient of the active particle and the active end of the dimer arises, which in turn leads to a repulsive motion of the dimer. A collision between the dimer and an active particle is avoided in this way. An example of a u-turn is captured and illustrated in Fig. 3.21. One notices that not only the dimer is repelled by the active

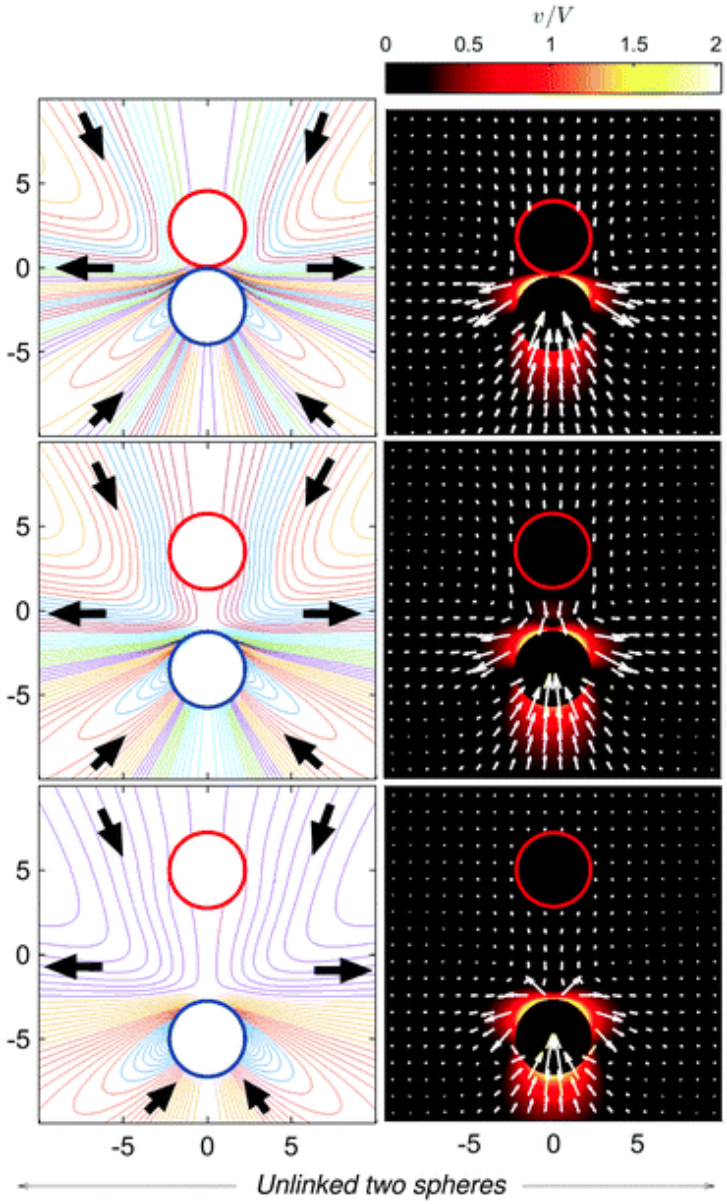

FIGURE 3.18: The streamlines and flow fields for a catalytically active particle with ongoing chemical reaction and a catalytically passive particle close by. The top, middle, bottom panels present the flow field with a distance between the active and passive particle $L/\sigma = 2.3, 3.5, 5$ respectively. Red: chemically active particle, blue: chemically inert particle. Image taken from [96].

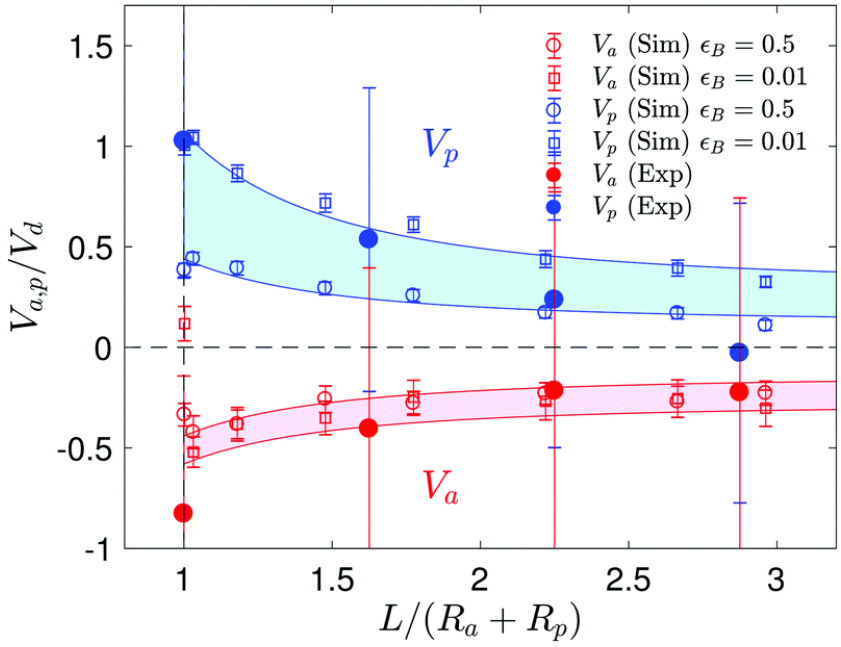

FIGURE 3.19: The velocity of catalytically active particle V_a and catalytically inert particle V_P as a function of separation distance L before they form a dimer. The unfilled circles and squares are simulation results and the filled circles are from experiments. The light blue and red aeras enclosed by L^{-2} lines correspond to that ε_B varies from 0.01 to 0.5 when $\varepsilon_A = \varepsilon_A^{cat} = \varepsilon_B^{cat} = 1$. The opposite signs of the velocity relate to the fact that the active and passive particles move in opposite directions. Image taken from [87].

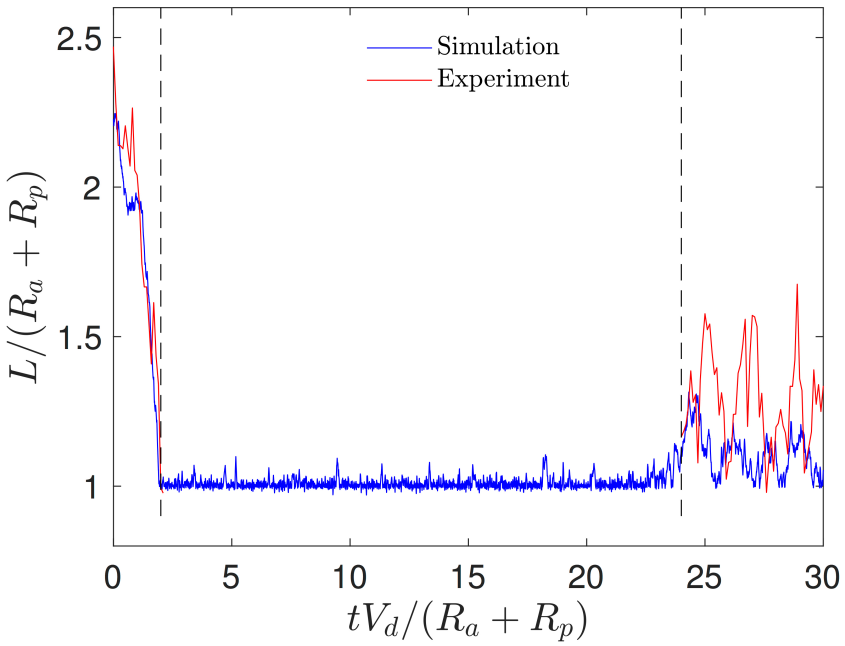

FIGURE 3.20: The dynamic of dimer formation presented with the separation distance as a function of time. t = 0 corresponds to the moment light is switched on, catalytically active and inert particles approach each other and meet to form a dimer, when the separation distance decreases to the length of the sum of the radius of both particles $(R_a + R_p)$. The dimer propels with a velocity V_d. When the light is switched off, the dimer dissolves into two particles, which conduct Brownian motion. Image taken from [87].

particle, the active particle (red dashed circle) is also pushed back by the active head when contact is about to occur.

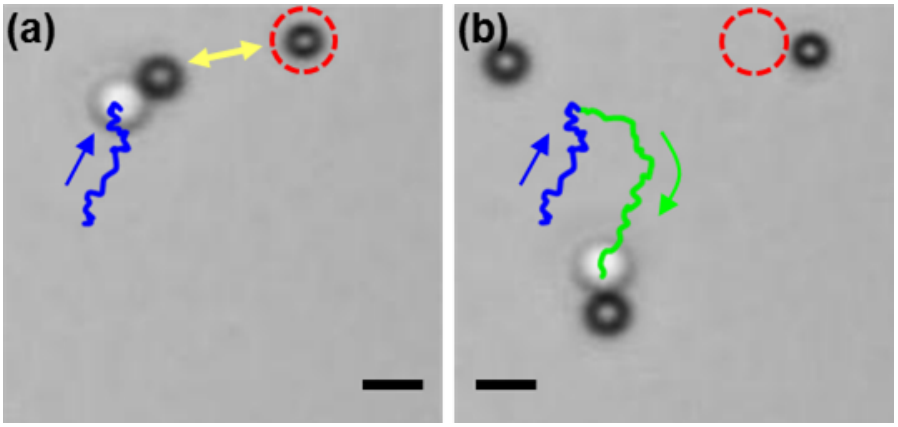

FIGURE 3.21: Repulsion interaction between dimer head and active particles. (a) A dimer propels towards an active particle (marked with red dashed circle). (b) The dimer active head is repelled from the active particle. The dimer turned around and continued propelling. The trajectory of the dimer before and after turning is presented in blue and green, respectively. The scale bar indicates 2 μm. Image taken from [87].

The repelling interaction between active particles is observed in simulation as well, and is demonstrated with the snapshots taken from the simulation in Fig. 3.22.

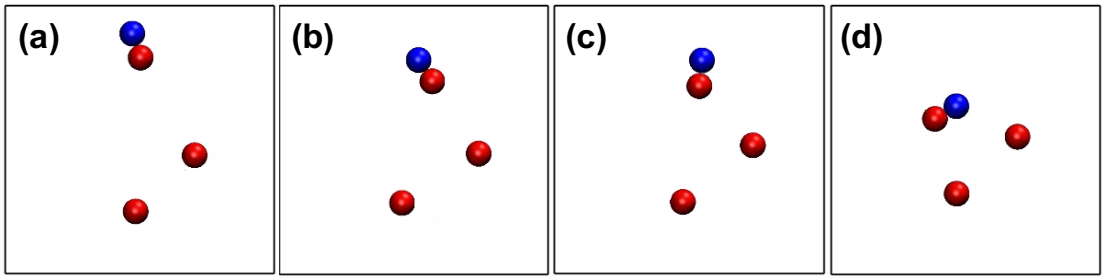

FIGURE 3.22: Snapshots from simulation showing repulsion between dimer head and active particles. Red: active particle, blue: passive particle. (a) A dimer propels. (b) The dimer active head is moving towards an active particle. (c) The dimer gets repelled and turned around. (d) The dimer continued propelling after the propulsion direction is changed. Snapshot taken from [87].

We have so far shown the factors that can influence the dimer formation and dimer stability. By choosing an appropriate particle density and particle ratio, the dimers can be effectively assembled and the stability of their motion is ensured. Finally, we evaluate the robustness of the system by collecting the statistics of the ratio of formed dimers, the motion of which sustained for more than 20 s. The active dimer ratio after dimer

formation for 20 s is plotted against the particle density in Fig. 3.23.

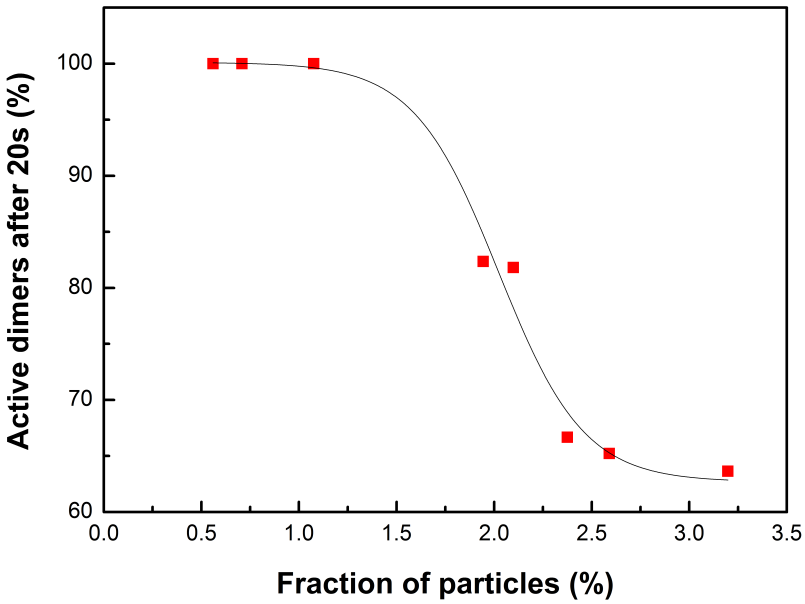

FIGURE 3.23: Not only dimers, but multimers will be formed with increasing number of particles. The ratio of active motile dimers that survive after 20 s is plotted against the overall fraction of particles for a fixed passive to active ratio of 1:3. Black curve is a fitting to the data. Image taken from [87].

As a new route for fabrication of Janus micromotors, we have presented that the dimer formation can be controlled with UV light. Switching on the light, dimers form and propel. Switching off the light, the dimer falls apart and the individual isotropic particles undergo Brownian motion.

3.7 Fusion of the Dimers

How to keep the formed dimers assembled once they are formed so that they can be used for further applications remains an untackled question. To realise the permanent assembly of this self-assembled dimer, we turned to an organic compound dopamine, which is found to be a widely used adhesive material. The adhesion property of dopamine originates from its chemical structure. There are different theories to explain the adhesion mechanism (See Fig. 3.24 from [97]). The two hydroxyl groups can build up hydrogen bonds with certain material surfaces or form coordination bonds after losing two hydrons at high pH value, or the hydroxyl groups are oxidized to carboxyl groups,

which are responsible for the adhesion.

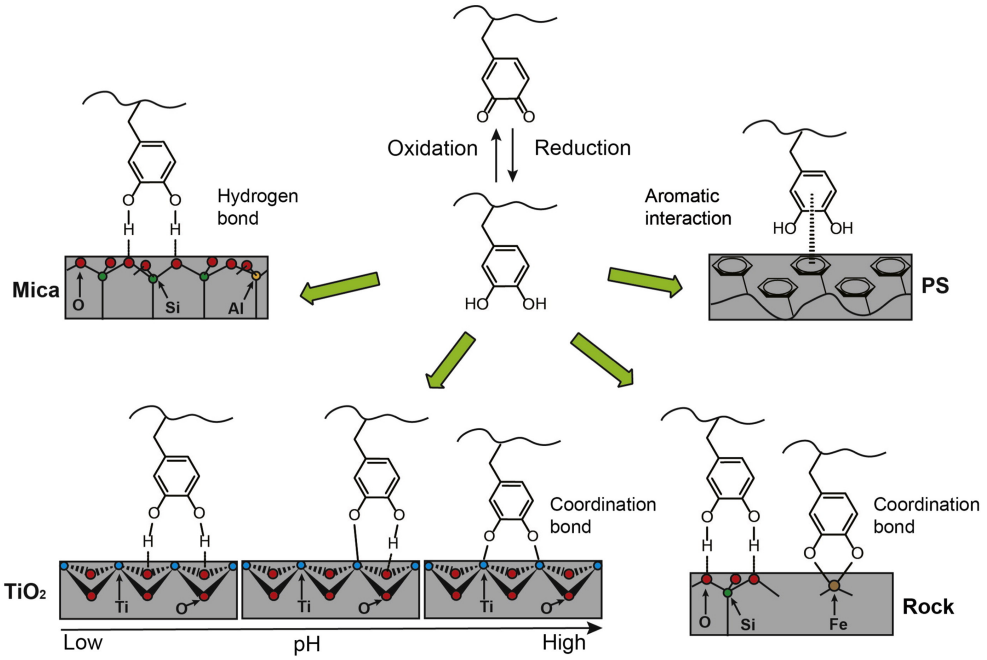

FIGURE 3.24: Mechanisms to explain the adhesion behavior of dapoamine or DOPA-mediated adhesive to different substrates. Image taken from [97].

We prepared a dopamine solution with a concentration of 1 mg/ml and run the same experiment described in previous sections. When the dimers are formed under UV illumination. 1 µl of dopamine solution is gently added to the dimer mixture. The dopamine soaked the solution and the mixture is dried. The active and passive particles which formed the dimers are found adhered together after few seconds after adding the adhesion material. The process is shown with microscope images captured in Fig. 3.25.

3.8 Conclusion

In this chapter, we have reported a new route to form Janus particles with an asymmetric catalytic dimer structure. The assembly starts with a colloidal mixture with two simple, isotropic SiO_2 and TiO_2 colloids in 2.5 % H_2O_2. The pH of the mixture is adjusted to neutral with TMAH. Owing to the photocatalytic activity of TiO_2 in hydrogen peroxide, a chemical gradient is generated around the active TiO_2 particles under UV illumination. A passive SiO_2 particle nearby experiences a diffusiophoretic attraction such that the passive SiO_2 and TiO_2 particles move towards each other until they finally meet and form a dimer. The motion of the active TiO_2 particle towards the passive SiO_2 particle

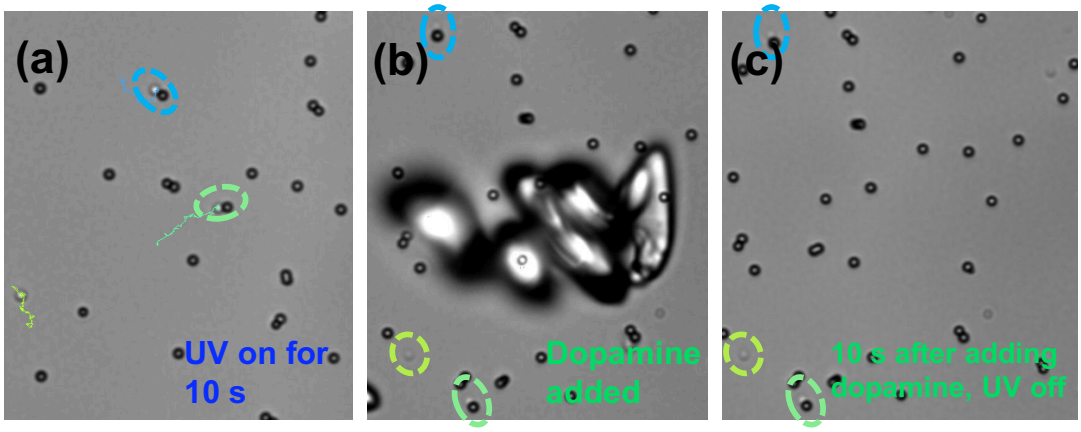

FIGURE 3.25: Dilute dopamine solution adheres the individual particle together in the formed dimer. (a) Dimer formed and propels for 10 s. (b). 1 mg/ml dopamine solution is added to the mixture tank, and freezes the formed dimer. The bubble-like phase is the mixing of the dopamine solution and the colloidal solution. (c) The dimers remain assembled when UV is off and 10 s after adding dopamine.

is a result of the combination of the attractive interaction between the active and the passive particles and the fluid flow generated by the chemical gradient. The motion of SiO_2 towards TiO_2 changes the chemical gradient distribution around the TiO_2 particles. As a consequence, the TiO_2 particles are observed to move to the SiO_2 particles. The chemical distribution at the dimer is not geometrically symmetric so that the formed dimer retains its structure stably and self-propels until one switches off the UV illumination. The dimer will then split into two particles and undergo Brownian motion. This process is reversible by switching UV light on and off. The propulsion speed of the dimer is linearly dependent on the UV light intensity applied.

By validating with an ionic experiment and varying passive material, the mechanism of the dimer formation is understood to be caused by the diffusiophoretic interaction. Therefore, the system is material independent and offers more material combination options to Janus structures such as biphasic TiO_2/PS dimers. The lower propulsion speed of TiO_2/PS than the TiO_2/SiO_2 dimer is observed and could be due to the different phoretic mobility of the different materials and the misaligned chemical gradient and propulsion orientation of TiO_2/PS because of the lower density of PS than SiO_2. The efficiency of the system is examined by tuning the particle ratio and density. An optimal active to passive particle ratio of 3:1 and a optimal particle density of 2% are found. A diffusiophoretic repelling interaction between the active particles is noticed. Having more active particles present in the mixture so that when a formed dimer propels with its active end heading toward the redundant active particle, collision can be avoided by the repulsion interaction between the head of the dimer and the active particle roadblock.

In this work, a spontaneous symmetry breaking is realised by a light-induced phoretic interaction between isotropic photochemically active and passive particles, and thus forms an asymmetric dimer which can self propel. This route enables the self-assembly and self propulsion of Janus structures. In comparison to conventional fabrication methods, this process provides the possibility of larger scale fabrication, and meanwhile simplifies the fabrication equipment and setup.

Chapter 4

Microchannels with Self-Pumping Walls

This chapter is based on and contains excerpts and figures from the article ”Microchannels with self-pumping walls” [98]. Contributions of coauthors are indicated.

4.1 Motivation

Chemically active Janus micromotors conduct active motion in a chemical solution, like Pt/SiO_2 in H_2O_2 [18], [99] and Pt/Au nanorods in [14]. This motion is defined as self-diffusiophoresis and self-electrophoresis, which is caused by the fluid motion in the boundary layer of the Janus particles where the chemical gradient is generated. Compared to biological microswimmers, these artificial micromotors can be fabricated and externally controlled. They are intensively studied since they are a model system to study collective behaviour, such as swarms. To understand how the micromotors interact with each other when they interact or perform self-assembly, the fluid motion plays an important role.

It has been noted very early in the development of such self-propelled Janus particles that the reciprocal situation, in which a catalyst patch is imprinted on a support that is fixed, rather than being free to move, will lead to hydrodynamic flow in the vicinity of the patch [13]. By fixing asymmetric Janus micromotors on a surface, the motion of the motors can lead to the fluid flow pumping. A conceptually novel and very promising direction of development is therefore to employ “active surfaces” to achieve autonomous micropumping, an idea that connects with a variety of chemically active, self-propelled particles [65], [90], [100]–[102].

Pervious studies have shown that a Janus (2-patch) structure can chemically drive local recirculating flows, for instance gold patches with 6-120 μm diameter on silver in H_2O_2 [16] or with 30 μm diameter on platinum substrate [103], 30-50 μm platinum disks on doped Si [104], enzyme functionalized patch on glass substrate [105]–[107] and ion-exchange resins on glass [108]. Two- or three-dimensional convective flows, owing to the patch creating chemical or electro-chemical gradients along the surface and in the bulk, have been observed. In such configurations the topology of the flow remains that of a recirculating flow towards (or away) for the source/sink represented by the patch; a directional "inlet" to "outlet" linear channel flow based on such patch geometry has so far not be achieved. On the other hand, it has been argued theoretically that it should be possible to drive flow in a channel via chemically active walls for suitably chosen patterns of activity and/or sufficiently asymmetric topography of the wall [107]–[109], such a self-pumping microchannel has been so far not demonstrated experimentally.

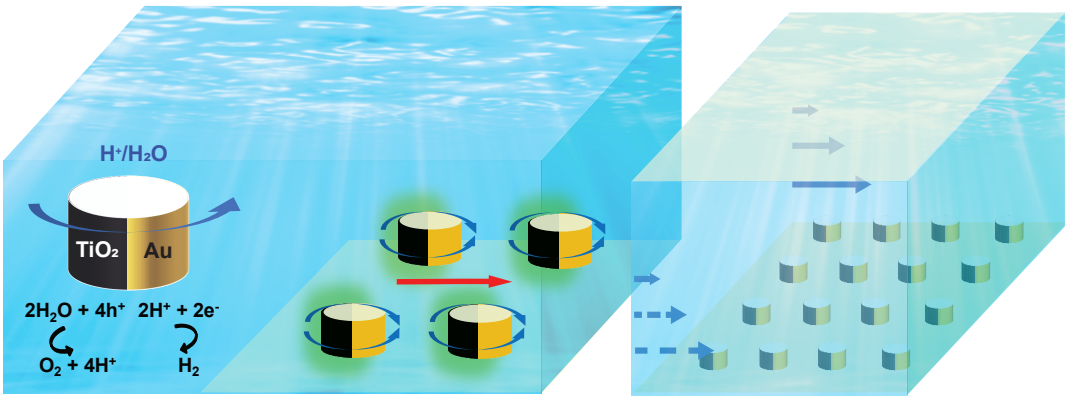

FIGURE 4.1: Left: A Janus pillar catalyzes a water splitting reaction under UV illumination, which gives rise to osmotic flow indicated with blue arrows around the pillar. Center: Within an ensemble of oriented pillars, a cooperative effect of these local osmotic flows leads to an unidirectional macroscopic flow shown in red arrow along the alignment (TiO_2 $\rightarrow$ Au direction) axis of the pillars. Right: Within a microchannel, the active surface provides an active traction and drives bulk fluid flow. Image taken from [98].

Microfluidic devices enable a small volume of samples for chemical and reagents analysis. The application of microfluidic devices varies from toxin detection to DNA sequence analysis. The issue of fluid pumping has been at the core of the development of microfluidic [110], [111] devices because ensuring the portability and autonomy of the device is essential for translating the lab "proof of concept" into an economically viable product. While in certain cases it is possible to exploit simple physical principles, like capillary imbibition, to achieve a functional device (e.g, the blood imbibition into the stripes of modern glucose meters), micropumping remains essential for the development

of any continuous flow operating device. Many of the currently employed microfluidic pumping methods require fluid lines and syringes (mechanical, pressure pumping) [111] or wires, batteries, and field generators (electro- or magneto-kinetic pumping) [112]–[114]. This has been long recognized as a major hindrance, as the extreme miniaturization of the "lab on a chip" architecture is washed out by the (comparatively) huge size of these auxiliary parts. Accordingly, various alternative means of achieving contactless micropumping have been proposed. For example, "acoustic" pumping has been realized by inducing – via sound waves of suitable intensity and frequency spectrum – fast, complex patterns of oscillation into elastic, sharp edge structures grafted onto the walls of the microfluidic device [115]; additionally, this allowed the development of a chaotic mixing pattern of flow within the channel, which could be very useful in applications based on two-phase flow interfacial chemical reactions. Although such methods remove the need for fluid lines and wires, they provide only a marginal improvement since their functionality remains dependent on bulky generators.

In this chapter, a chemically active surface was fabricated by photolithography and GLAD deposition, with which a robust large area of Janus structure array can be prepared with a precisely controlled structure size, height and spacing down to submicrometer. Two systems were tested for the pumping behaviour. One is with SiO_2/TiO_2 Janus structures in H_2O_2, the other is with SiO_2/TiO_2/Au in H_2O. We evaluated the effect of topological structure on pumping with three topological structures for the SiO_2/TiO_2/Au micropillar array. The first structure we studied was micropillars. Under suitable UV illumination, the micro Janus pillars promote the photochemical water splitting reaction to oxygen and hydrogen, and the local osmotic flows around the micropillars connect to drive macroscopic flow, through a significant part of the cross section of the channel, along the whole length of the channel as discussed below and as illustrated in Fig. 4.1.

In contrast, no pumping is observed when the topography of posts is replaced by arrays of TiO_2-Au micro-disks on the glass wall, which highlights the crucial role played by the 3D pillar structures, for which the local osmotic flows are mainly along the lateral surface of the pillars. The active microfluidic pumping achieved this way is stable, uniform along the channel, "green" (only water splitting is involved), and can be switched on and off simply by turning on and off the illumination. Furthermore, we show that by varying the spacing of the array of micropillars it is possible to optimize the microfluidic pumping, in the sense of achieving a maximal flow speed right above an active wall. Finally, by combining such active surfaces to create top and bottom walls with different alignments of the $TiO_2 \rightarrow$ Au direction, or simply different activity, various

flow profiles can be created inside the channel. We used a simple fluid dynamic model of an active channel, in which a wall-slip velocity is provided by the active surface, to describe the experimentally observed flow profiles within the channel. Combination of active top and bottom walls with different orientations of the pillar arrays leads to linear or parabolic flow profiles across the channel.

4.2 Pumping of SiO_2/TiO_2 micropillar array with H_2O_2

To validate the assumption if an immobilised array of Janus particles or structures can drive fluid flow, we started with a well-established photochemical system SiO_2/ TiO_2.

A 2 μm diameter hole array was templated by photolithography on a cover slip. The sample was then exposed to a SiO_2 flux in a Glancing Angle Deposition (GLAD) chamber at an incidence angle $\alpha = 0^\circ$ for a 1 μm thick deposition. The photoresist was dissolved in acetone. A SiO_2 micropillar array remained on the substrate as the SEM image indicates in Fig. 4.2a. The symmetry of the SiO_2 array is broken by evaporating a thin layer of another material TiO_2 at an incidence angle of 40°. The resulting structure is to be seen in Fig. 4.2b. Since the shadow effect took place only in the direction of the sample-flux alignment, the regions between the pillar lines were coated with TiO_2 as well. The sample was then rotated by 180° with the same α angle and coated with a thin film of SiO_2. From the SEM images of top view of one single pillar, one can easily distinguish two different materials on two sides of the pillar, namely SiO_2 and TiO_2 (Fig. 4.3).

Covering the fabricated patterned surface with 300 μm thick 2% H_2O_2, a fluidic chamber was formed with a spacer. The fluid flow was visualised by adding 1 μm polystyrene beads into the solution. The motion of the tracer particles was observed and recorded with an Andor 5.5 camera with a framerate of 20 frames per second. In each observation two states were recorded, with UV light illumination off, and with it on. When the UV illumination was off, all tracer particles undergo Brownian motion. Once the UV is turned on, the tracer particles start to move in one direction. We tracked the tracer particles and deduce a pumping velocity of 3.6 ± 0.4 μm/s. The tracked trajectories of the tracer particles are presented in Fig. 4.4. The image on the right in Fig. 4.4 was processed in Matlab to subtract the fixed micropillars as background. The green and blue lines on the right image of the figure are the tracked trajectories of the tracer

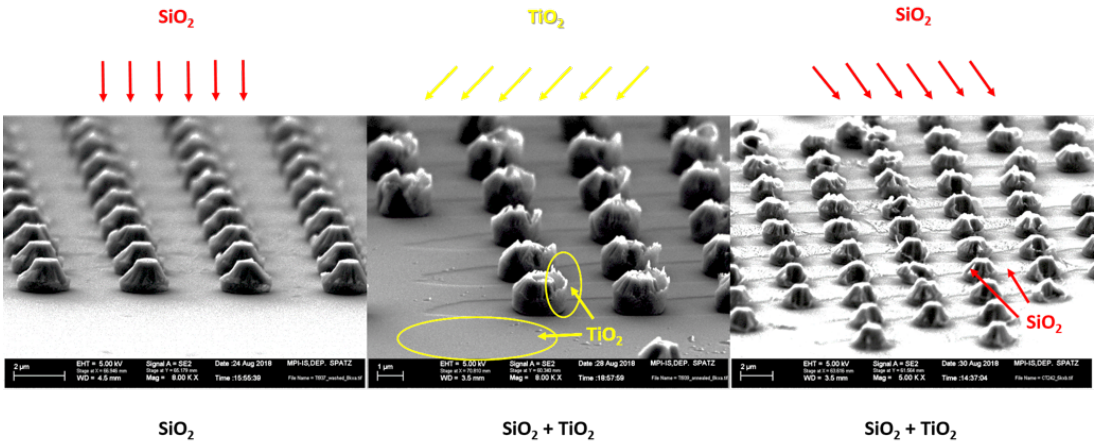

FIGURE 4.2: Fabrication of active surfaces by shadow deposition onto photolithographically patterned substrates. (a) Deposition of SiO_2 under normal incidence, followed by lift-off of photoresist and (b) glancing angle deposition of TiO_2 and (c) SiO_2.

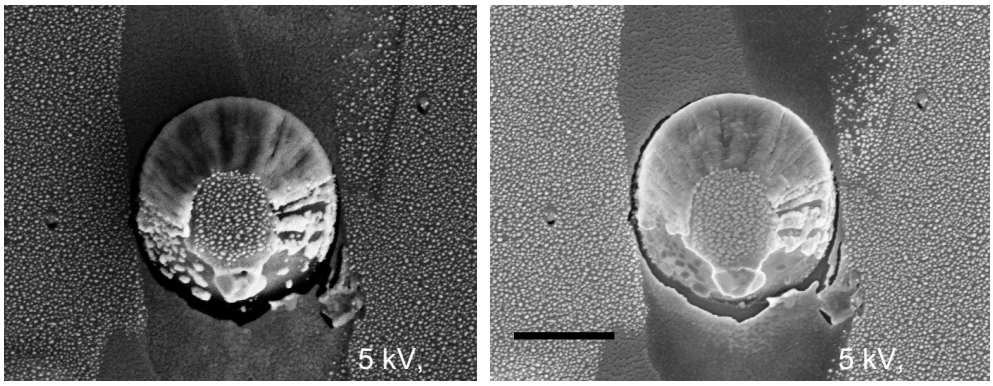

FIGURE 4.3: Top view SEM images of a single pillar with left: SE2 detector; right: InLens detector. Both clearly show two different materials deposited on two sides of the pillar. Scale bar represents 1 μm.

particles for 10 s.

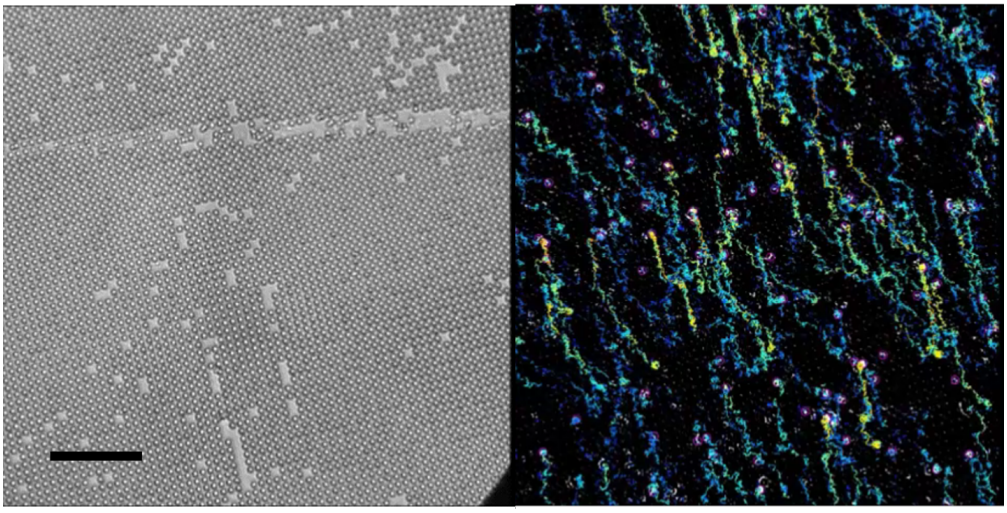

FIGURE 4.4: Left: Image taken from a recorded video to observe the pumping behaviour of the active surface. Right: Tracer particles are tracked and indicate an active pumping of the surface. Background has been subtracted

The pumping of the SiO_2/TiO_2 micropillar array proves the principle that a photochemically active diffusiophoretic structure can drive fluid flow, and by constructing an array, the microscopic flow should be able to form a macroscopic fluid flow.

4.3 Pumping with H_2O: Fabrication and Characterization of Photochemically Active Patterned Surfaces

Now that it has been established that H_2O_2 can be pumped with a SiO_2/TiO_2 micropillar array, it is interesting to ask if the system can pump water with another photocatalytic system that does not need H_2O_2. In this thesis, a material combination of TiO_2/Au was chosen for its high efficiency in catalyzing the decomposition of water under UV illumination.

4.3.1 Fabrication of the Micropillar Array

The Janus micropillar array is fabricated on a cover glass using photolithography and GLAD deposition. The first step is to make a hole array pattern with adjustable diameter and spacing using photoresist maP1215 (MicroResist Company). The cover glasses

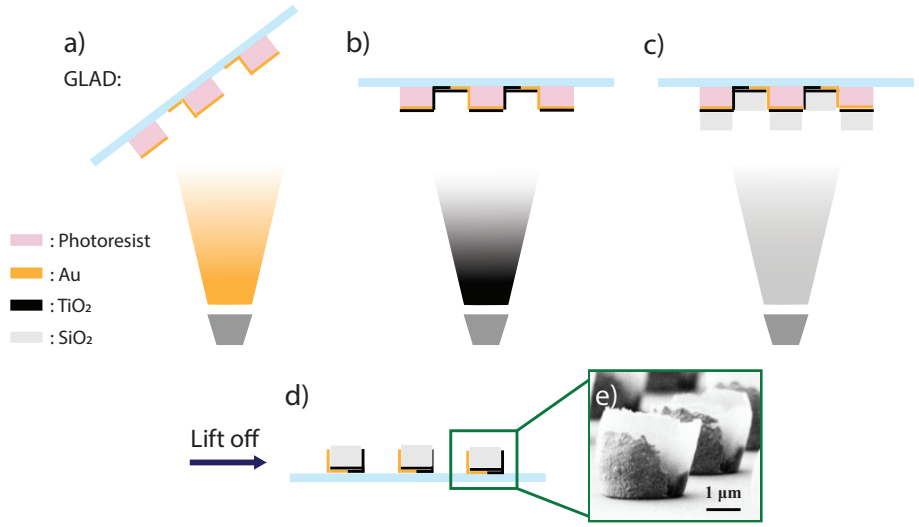

FIGURE 4.5: Fabrication of active surfaces by shadow deposition onto photolithographically patterned substrates. (a) Glancing angle deposition of Au, followed by deposition under normal incidence of (b) TiO_2 and (c) SiO_2. (d) Lift-off of the photoresist results in the TiO_2 - Au micropillars as shown in the SEM image in e. Image taken from [98].

are piranha cleaned, dried with nitrogen gas and a hot plate at 200 °C for 2 min. A layer of adhesion primer Hexamethyldisilazane (HMDS) and maP1215 are spin coated sequentially with the same acceleration and rotation speed, which results in a 1.5 - 2.8 µm thick photoresist layer. This is then soft baked at 100 °C for 90 s, followed by a 85 s of exposure with a UV flux intensity of 4 mW/s with the SUSS microTec mask aligner. The samples are developed with developer maD-331 for 60s and rinsed with water to terminate the development. After the samples are dried at room temperature, the thickness of the 2 µm diameter hole structure array is characterised with a profilometer (see SEM image in Fig. 4.6). With the prepatterned hole array, the sample is loaded in the vacuum chamber for the next GLAD deposition. For a hole array sample with a thickness of 1.6 µm, the α angle of the GLAD substrate holder is set to 18 °. 80 nm thick Au was deposited by e-beam evaporation. 100 nm TiO_2 and 1400 nm SiO_2 was evaporated on top of Au at 0 °. A lift-off process in aceton to remove the photoresist and air plasma cleaning were executed before placing the sample for TiO_2 annealing at 450 °C for 2h in air. The SEM and EDX image of a SiO_2/TiO_2/Au micropillar array after annealing is shown in Fig. 4.6 (right) and Fig. 4.7.

4.3.2 Fabrication of the Microdisk and Microbar array

The steps in fabricating the two-dimensional micro-disk arrays were identical to the fabrication of the micropillar array. The only difference is that a 100 nm of TiO_2 layer

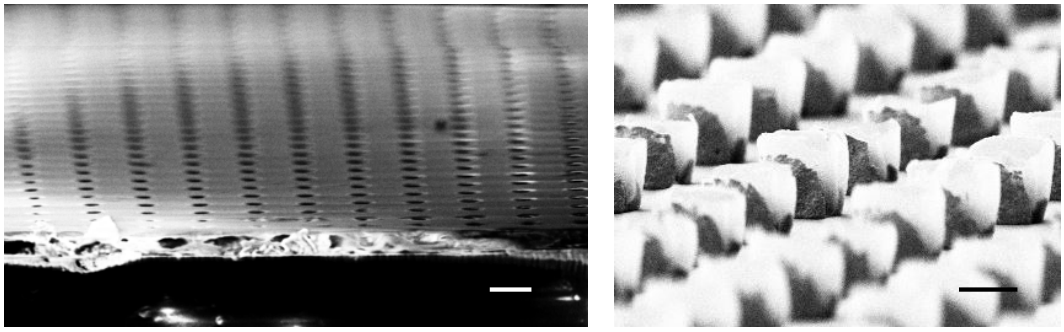

FIGURE 4.6: SEM image of a microhole array of photo resist maP1215 (left), and a SiO_2/TiO_2/Au micropillar array (right), scale bars represent 5 μm and 1.5 μm, respectively. Image (right side) taken from [98].

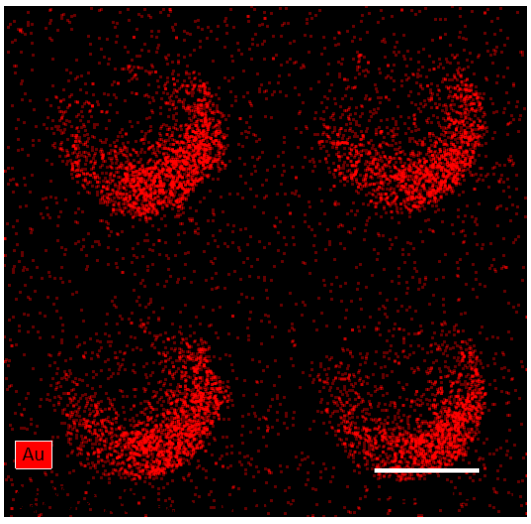

FIGURE 4.7: EDX image (top view) of a SiO_2/TiO_2/Au micropillar array, scale bar represents 1.5 μm. Image taken from [98].

was evaporated first at 0 °, and 20 nm of Au deposited at $\alpha = 32$ °.

The fabrication of a microbar array is the same as the procedure used to realize the micropillar array. The SEM images of a microdisk array and a microbar array are shown in Fig. 4.8

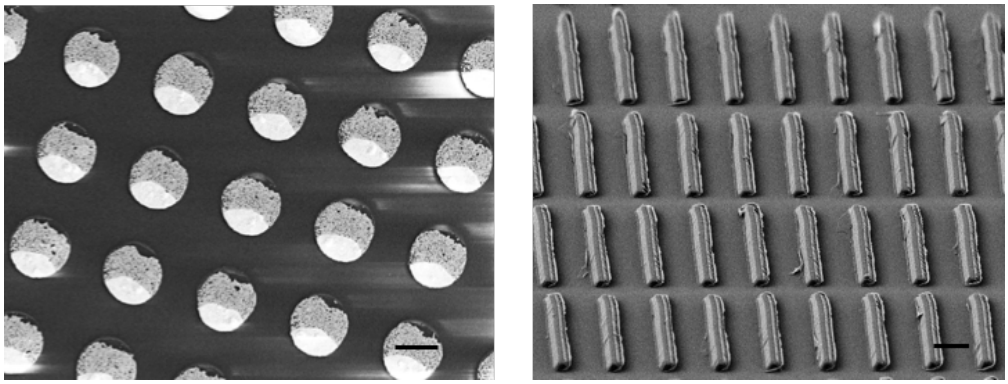

FIGURE 4.8: SEM of a TiO_2/Au 2D microdisk array (left) and a SiO_2/TiO_2/Au 3D microbar array (right), scale bars represent 1.5 μm. Image adapted from [98].

4.4 Active Wall Pumping

4.4.1 Mechanism of Pumping

A photocatalytic decomposition reaction of water can be achieved with a material combination of TiO_2 and Au. At the semiconductor (TiO_2) side, electron-hole pairs are generated. The holes can react with H_2O to produce O_2 and H^+, which dissolves in small amounts in H_2O, while the electrons are transferred to the metal (Au) side, and recombine there with H^+ to produce H_2, which dissolves in H_2O. Accordingly, there is an electrokinetic flux of H^+, through the solution and around the pillar. Gradients in chemical composition (depicted in the Fig. 4.1 center as the green clouds around the pillars) develop in the vicinity of the pillar due to the release in the solution of O_2 and H_2 at the opposite sides of the Janus pillar, and diffusioosmotic flows develop around the pillar. The superposition of the two effects leads to a net "osmotic slip" along the lateral surface of the pillar, as schematically indicated by the arrows in Fig. 4.1. The two effects are illustrated in greater detail in Fig. 4.9. The final flow is composed of two parts of flows as a consequence of two effects. The green arrows indicate the fluid flow induced along with the electrophoretic proton flow from the TiO_2 side to the Au side. The red arrows show a diffusiophoretic interaction. This interaction is coupled with a

resultant hydrodynamic flow. The direction of this osmotic slip is inferred to be from the TiO_2 side towards the Au one (see also experimental results below). To avoid the interaction between the particles and the TiO_2 end due to the diffusiophoretic interaction, 1 μm PS beads which suspend well are taken as tracers instead of 1 μm SiO_2 beads. The tracer particles are used to visualize the fluid flow.

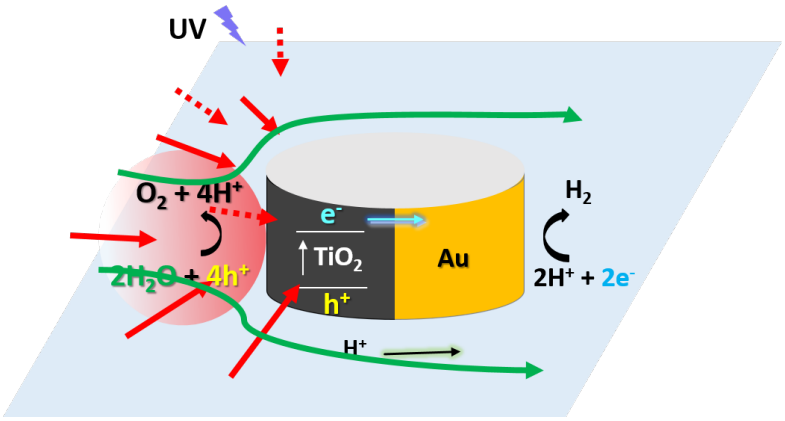

FIGURE 4.9: Illustration of the mechanism of fluid flow generation around a Janus micropillar. Electroflux of H^+ induced flow is represented in green arrow, while diffusioosmoic slip flow as a result of the diffusiophoretic interaction in red arrow.

4.4.2 Active Wall Pumping Performance Optimization

The micropillars on the wall have a height of 1.5 μm and a diameter of 2 μm (see Fig. 4.1d). There are several factors that can affect the performance of the active wall pumping, and two are investigated in this thesis as suggested by the mechanism explained in section 4.1, a cooperative effect between the osmotic flows around the pillars: the spacing between the micropillars and the topological chemical structure on surface.

In all the experiments, the pumping velocity is measured with the aid of 1 μm polystyrene tracer particles in the fluid. The motion of the particles is recorded with an Andor CMOS camera attached to an inverted optical microscope. The white light source is from the top, and the UV light with a wavelength of 365 nm is used to control the pumping. The maximum UV light intensity used for pumping is 320 mW/cm^2. An image processing step is performed with ImageJ to track the tracer particles.

Two methods are used to map the cross sectional flow profile of a microfluidic channel; a defocusing method, and imaging with confocal microscopy.

Confocal microscopy

Compared to a widefield fluorescence microscope, pinholes are introduced to a confocal microscope as seen in Fig. 4.10.

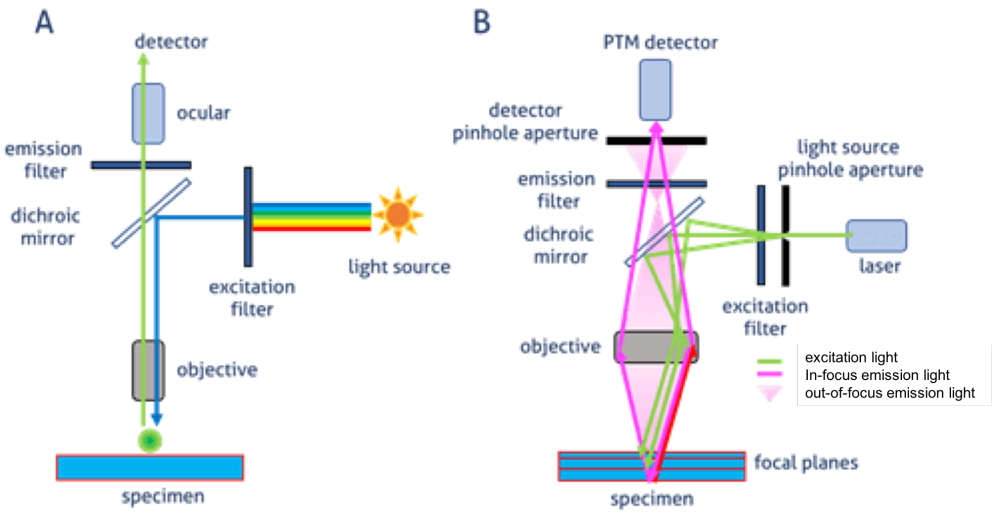

FIGURE 4.10: Comparison of the structure between (A) a widefield fluorescence microscope and (B) a confocal microscope. Image taken from [116].

The pinhole allows the light with selected wavelength to pass from the focal plane. In this way, any light from the out-of-focus plane is filtered out. By adjusting the pinhole, the sample can be scanned along the z direction. With the help of the confocal microscope, we were able to map the cross sectional flow profile of a pressure-driven microfluidic channel with a height of 60 μm and a width of 100 μm. In Fig. 4.11, an image taken from the measurement of the flow using 1 μm fluorescent particles with a confocal microscope is shown with a bright field view for reference.

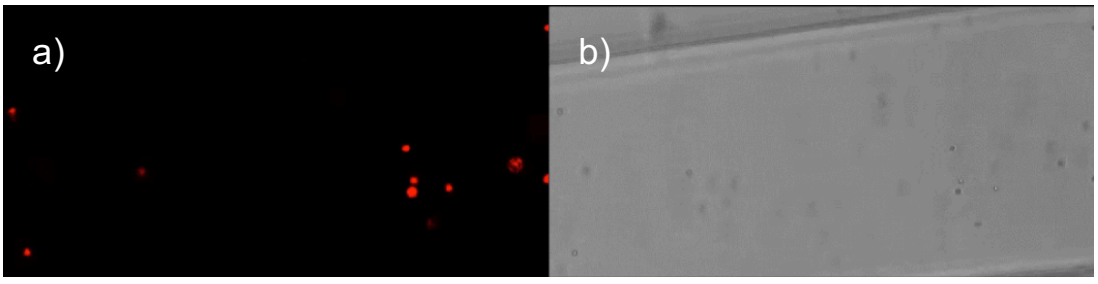

FIGURE 4.11: 1 μm fluorescent PS particles in a normal microfluidic channel driven by an external syringe pump to map the flow at each height of the cross section of the channel. (a) An image take at the height of z = $\sim$ 12 μm with confocal mode, (b) with bright field mode for comparison.

A video stack over the whole cross section is taken. An example of images in two planes with z = 0 μm and z = 28 μm is shown in Fig. 4.12. The flow velocity of each plane is calculated by tracking the (red) particles, and taking an average. The resultant flow profile of a parabolic flow in a pressure-driven microfluidic channel is shown in Fig. 4.13.

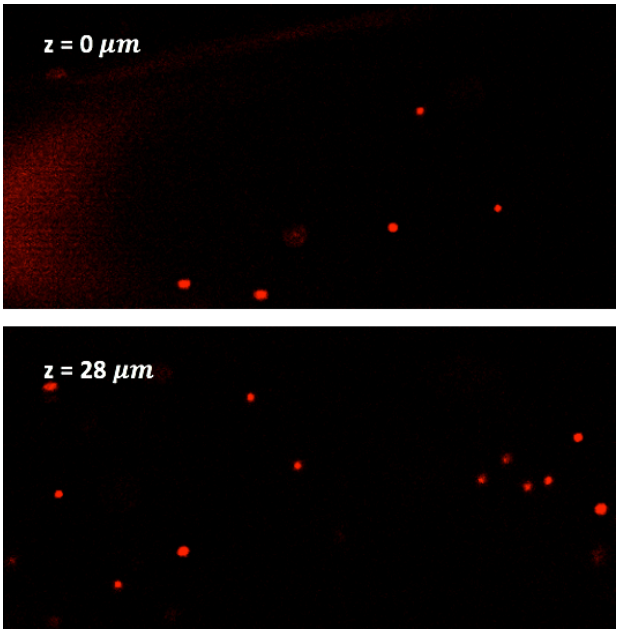

FIGURE 4.12: Images taken with a confocal microscope. Tracer particles in two planes in a microfluidic channel.

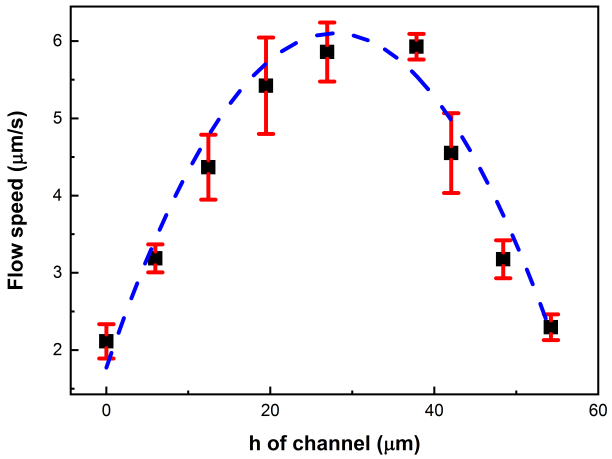

FIGURE 4.13: Cross section of the flow profile of a pressure-driven microfluidic channel measured with a confocal microscope.

Defocusing method

The flow profile is also determined using a defocusing method from reference [117]. In this method, we first calibrate the height by adjusting the z position of an optical microscope with a sample prepared by immersing and immobilizing 1 μm PS spheres in a 3 % polyacrylamide (PAC) gel. The diffraction pattern is taken and analysed at different heights (z levels). The reference stacks are shown in Fig. 4.14a, and the corresponding diffraction pattern vs. defocusing height is plotted in Fig. 4.14c. The tracers in the desired plane above the wall can be identified by adjusting the z-position of the microscope stage.

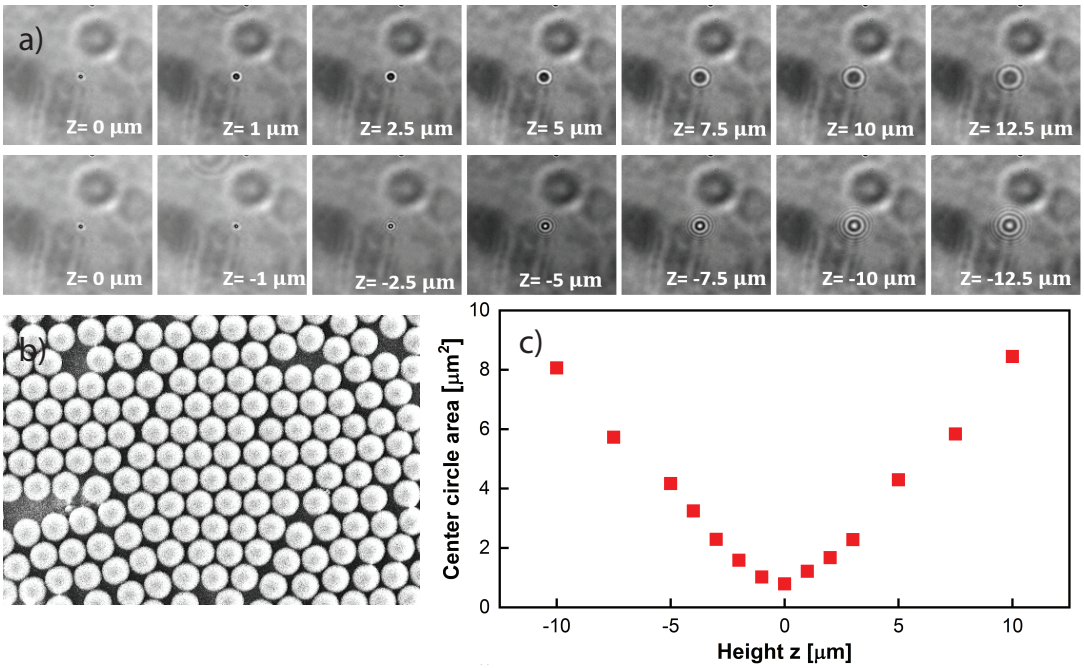

FIGURE 4.14: (a) Reference stacks of 1 μm PS spheres at different height z relative to the focal plane. (b) SEM image of 1 μm PS spheres used for fluid tracking. (c) Relationship between the calculated diffraction pattern area and the height relative to the focal plane. Image taken from [98].

The pumping performance is presented in Fig. 4.15 for a single active surface with micropillars with a spacing of s = 2 μm. The sample is assembled with an active surface and a 300 μm thick spacer. The 300 μm thick chamber is filled with milliQ water containing tracer particles and covered with a cover slip. Tracer particles at a height of z = 1.5 μm above the structures are observed and used to visualise the macroscopically directed flow. By tracking the speed of the tracer particles, the osmotic slip velocity is measured and defined at the active surface. In the absence of the UV illumination, no flow on the surface takes place and the tracer particles exhibit normal Brownian

diffusion as indicated in Fig. 4.15a. Once the UV illumination is turned on, one observes the directed motion of the PS (see the Fig. 4.15b), along the direction defined by the orientation of the Janus pillars. When the UV light is switched off, the flow directed motion instantly stops, and the PS particles switch back to Brownian motion (Fig. 4.15).

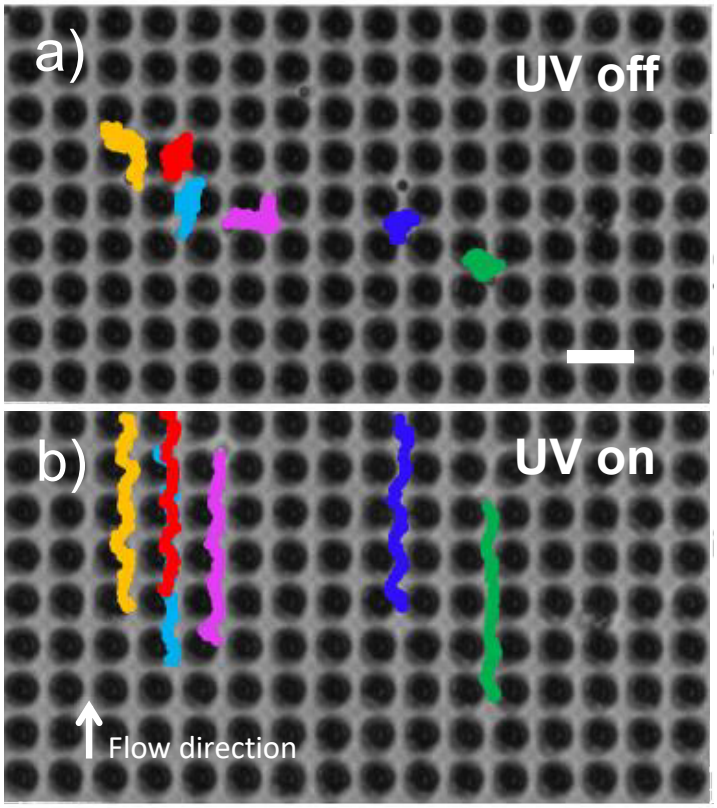

FIGURE 4.15: (a), (b) Trajectories of few tracer particles, distinguished by different colors, showing directional motion above the Janus micropillar array, when the UV light is on. The active surface is covered by a 300 μm thick liquid film. Image adapted from [98].

Furthermore, the fluid pumping speed can be adjusted simply by changing the incident UV light intensity. The dependence is found to be linear, to a good approximation (see the Fig. 4.16), which is compatible with a mechanism driven by the self-generated osmotic flows via photocatalytic chemical activity as long as the catalytic reaction does not saturate.

The effect of the pillar spacing on pumping performance is studied by fabricating grids of pillars with spacings between 2 and 18 μm. As indicated in Fig. 4.17, an optimal spacing corresponds to a pillar spacing of $s \approx 2$ μm, which is comparable to the pillar diameter at this spacing, the maximal wall-slip velocity is obtained. The flow velocity vanishes both at very large and very small values of s, and reaches a maximum

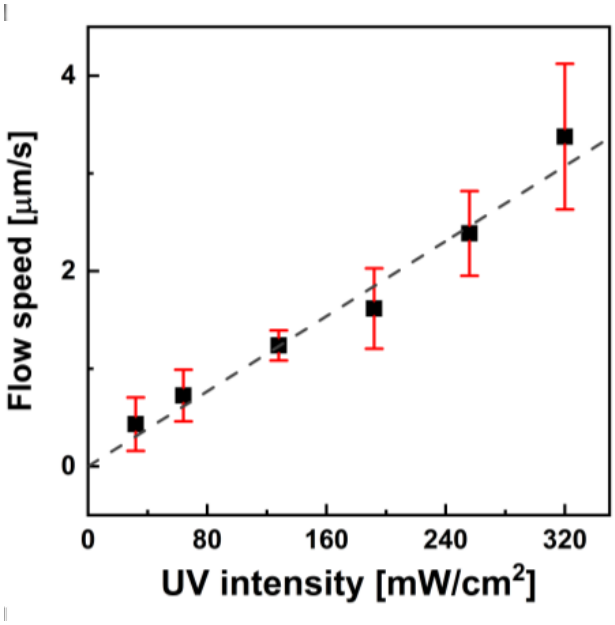

FIGURE 4.16: The average fluid speed within the plane located at 3 μm above the glass surface at roughly 1.5 μm above the top of the micropillars as a function of the UV light intensity (measured as fraction of the maximum available irradiance Pmax = 320 mW/cm^2). The dotted line shows a linear fit to the data. Image taken from [98].

for s = 2 μm (see the current Fig. 4.3d). When the spacing is increased to 5 μm, the flow speed is reduced by half, while for a spacing of 18 μm directional flow is hardly observable.

The emergence of an optimal spacing, at which the average velocity is maximal, can be understood as follows. In the regime of medium to large separations, increasing the spacing in the array translates into a decrease in the energy density of the pumping surface, and accordingly, a decrease in the flow magnitude. The regime of small separations is more subtle. Here, the pillars are no longer independent as the cross-talk between their chemical activities becomes significant. For example, using the illustration in Fig. 4.17, when the pillars are very close to each other, the chemical inhomogeneity produced by the Au side (black area) of one pillar produces similar gradients, but opposite to those of the TiO_2 region of the adjacent pillar. The net result is that the effective osmotic slip around each post is strongly reduced, and, accordingly, a decreased magnitude of the flow. Therefore, the optimal separation corresponds to the minimal one for which the chemical cross-talk between neighbouring pillars remains small compared to the self-sourced chemical inhomogeneities.

To examine the role of the topology of the chemical structure on pumping performance, the pumping experiments are conducted with a flat microdisk array as well

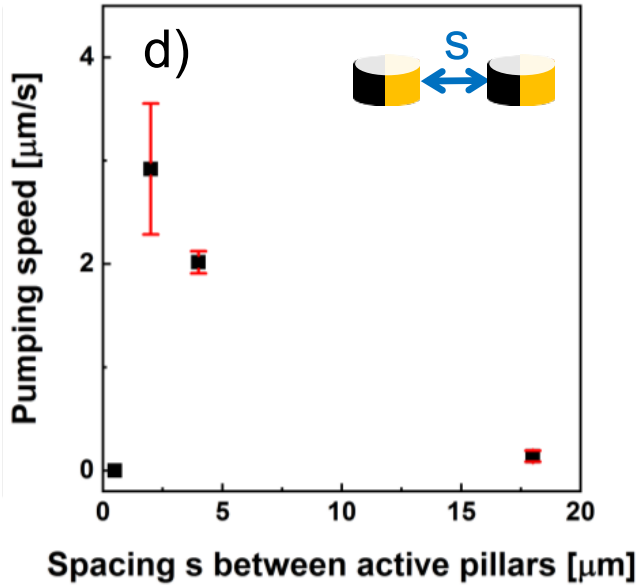

FIGURE 4.17: Dependence of the average flow speed slightly above the top of the pillars as a function of the spacing s of the array. The distinct maximum in the flow speed indicates the existence of a well-defined optimal spacing s $\approx$ 2 μm between the pillars. Image taken from [98].

as a 3D microbar array. The tracer particles in the plane above microdisk structures experience no directional transportation with the fluid, while a slip velocity, which is smaller than the micropillar pumping is observed above the microbars. The results are listed in Fig. 4.18 and suggest that the 3D geometry of the structures is essential for fluid pumping. The difference between the 3D pillar, 3D bar and 2D Janus structure is the side wall of the structure, which plays a crucial role in driving the fluid. The border of where two materials join on the side wall contributes the most chemical gradient in comparison to the border where the two materials join at the top.

4.5 Pumping in a Microchannel

4.5.1 Microchannel Pumping in a Water Reservoir

As discussed in chapter 2 theory and background, there are laminar flows, transitional flows and turbulent flows in pipe flows. In a microfluidic flow, the Reynolds number is typically in the range of Re $<$ 1, and a laminar flow is expected. The non-slip boundary of the pipe provides a shear stress on the fluid, leading to a parabolic flow profile illustrated in Fig. 4.19. It is of interest for chromatography or micro manipulation to modify the flow profile. Our self-pumping active walls provide the opportunity to adjust

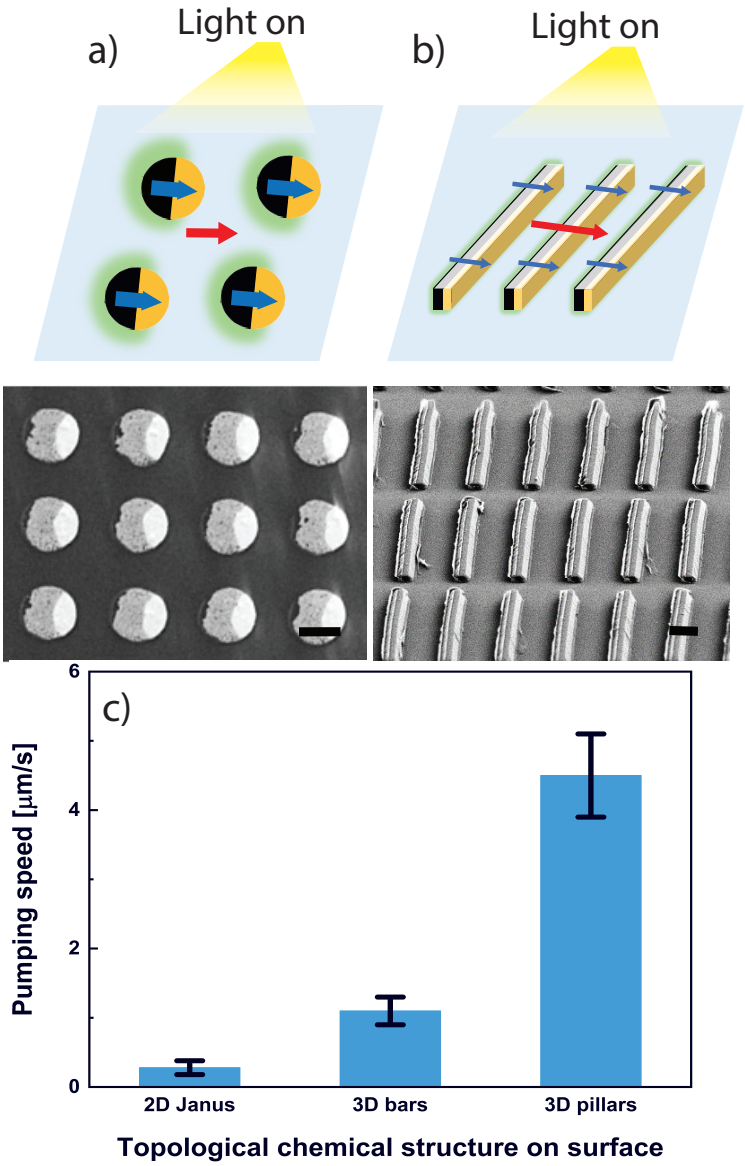

FIGURE 4.18: (a,b) Schematic (top) and SEM images (bottom) of a surface topologically patterned with (a) 2D Janus disks and (b) 3D Janus bar structures, respectively; the scale bars correspond to 1.5 μm. (c) Comparison of pumping behavior between different surface structures. Image taken from [98].

the flow profile via the active surfaces in a microchannel.

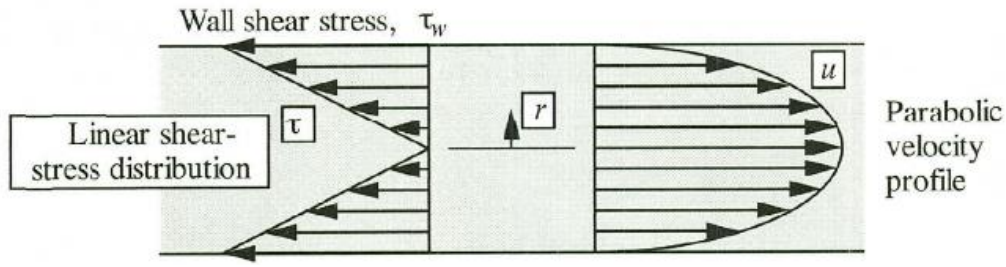

FIGURE 4.19: Shear stress and velocity distribution for a laminar flow in a pipe. Image taken from [118].

In this thesis, we assembled microchannels with active walls in three different configurations and demonstrate three flow profiles, respectively (Table 4.1).

TABLE 4.1: Active channel assembled with active walls.

	single active surface channel	two symmetric surfaces channel	two asymmetric active surfaces channel
top	inert no-slip wall	active surface	active surface
bottom	active surface	active surface	active surface
alignment	-	same direction	opposite direction
height [μm]	110	170	170

In what follows the bottom surface is always kept to be active. On the bottom surface, spacers with different heights are placed and used to control the channel heights. A cover slip or another active surface is placed on top of the spacer to form the channel. As discussed above, this sample is then placed in a 300 μm thick larger water reservoir containing 1 μm PS beads as shown in Fig. 4.20.

The samples are mounted on an inverted microscope (Zeiss Axio) and are observed with a 63x objective lens. Videos were recorded at a rate of 20 frames per second with a CMOS camera (Andor 5.5). The x-y positions of the particles in each 15 μm plane along the z position (the height of the channel) were tracked and averaged over at least 10 particles. An example of the tracked trajectories of particles in two different z planes z = 3 $\sim$ μm and z = 10 $\sim$ μm can be seen in Fig. 4.21.

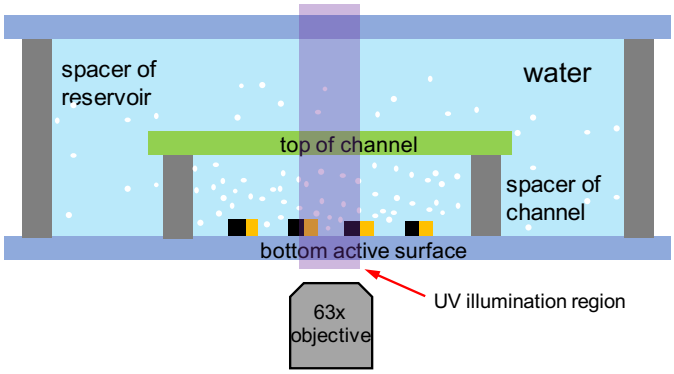

FIGURE 4.20: Side view of the single active surface channel. White dots represent PS tracer particles.

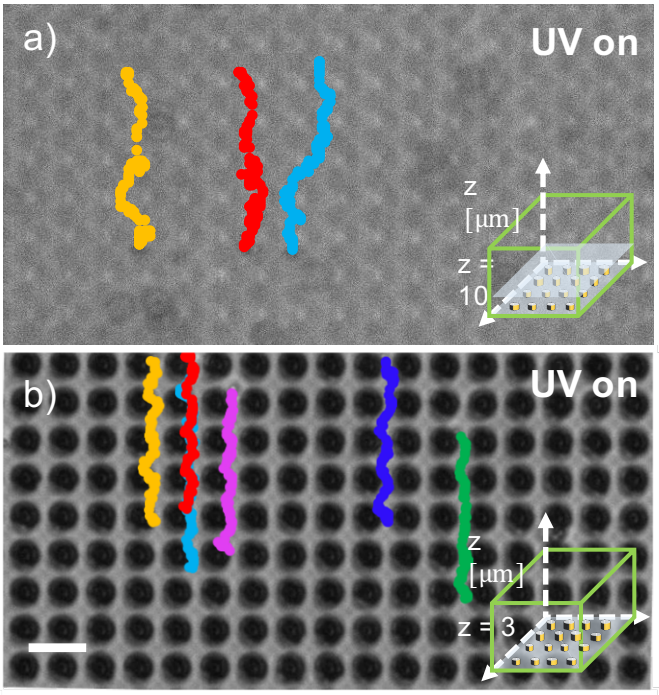

FIGURE 4.21: (a), (b). Trajectories of few tracer particles, distinguished by different colors, showing directional flow (when the UV light is on) at various heights above the Janus micropillar array. The insets illustrate the position of the plane in which the tracked trajectories are located. (c). In the absence of UV illumination, the tracers exhibit Brownian motion. Image adapted from [98].

The data points are plotted as a function of the z height within the channel in Fig. 4.26, the error bars refer to the standard deviation across these measurements. Three different flow profiles are achieved by three different channel designs. These clearly demonstrate microfluidic pumping by active walls when the channel is illuminated. The flow profiles are very different, which highlights the possibility to tune the flow, to a certain degree, simply by adjusting the relative alignment of active ethe two walls. In all cases one observes a significant flow velocity (above 1 μm/s) at a distance of 30-50 μm from the active walls.

4.6 Analytical Model

To predict the flow profile within the channel, a model was developed by Dr. Athanasios G. Athanassiadis. I have numerically analyzed the flow profiles (see section 4.7). Helpful discussion with the co-author is acknowledged, esp. Dr. Mihail Popescu. The schematic of which is shown in Fig. 4.22. In this model, we divided the channel into three sections: an inert inlet section of length L_1 (region 1), an active central section of length L_0 (region 0), and an inert outlet section of length L_1 (region 2). The height is the same for the continuous three sections h. The scale of the length L is generally much larger than the height of the channel. The external pressure at the inlet and the outlet is zero, since the channel locates in a reservoir of water. P_1 and P_2 are the pressure at the inlet and outlet of the active section. G_1, G_0, and G_2 are the pressure drops of the inlet, active and outlet section, respectively.

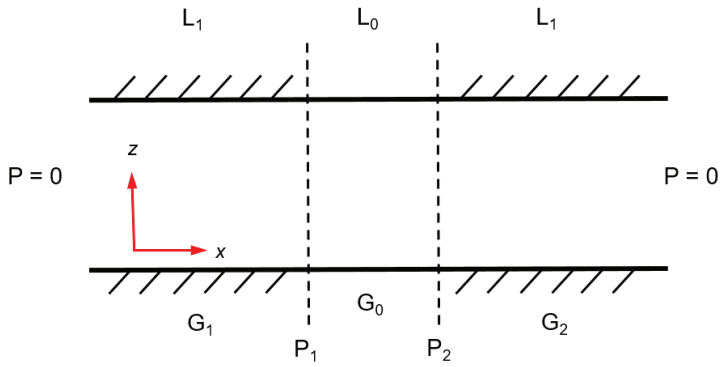

FIGURE 4.22: Parameter used in the analytical model to model the channel geometry. Image taken from [98].

For each section, the fluid flow can be described by the continuity equation 4.1 and the Navier-Stokes equations 4.2.

$$\nabla \cdot (\rho \mathbf{u}) = 0 \tag{4.1}$$

$$\rho \frac{\partial \mathbf{u}}{\partial t} + \rho \mathbf{u} \cdot \nabla \mathbf{u} = -\nabla p + \mu \nabla^2 \mathbf{u} + g \tag{4.2}$$

where μ is the fluid viscosity, $u(z)$ is the velocity of the fluid in the x-direction. In a channel with a geometry $h \ll L$, the fluid flows along the x direction, the $\mathbf{u}$ refers only to the x-component of the velocity. For an incompressible fluid, the equation 4.1 can be rewritten to $\partial \mathbf{u}/\partial x = 0$. The flow is assumed to be steady ($\partial \mathbf{u}/\partial t = 0$) and gravity is negligible within the channel. The Navier-Stokes equation is simplified to the Stokes flow form in a 2D channel:

$$\frac{dp}{dx} = \mu \frac{d^2 u}{dz^2} \tag{4.3}$$

$p(x)$ is the pressure in the channel which is independent of z. The pressure p changes only with x and the velocity u only changes with z, plus the constraints of equation 4.3, $\frac{dp}{dx}$ has to be a constant. This constant is defined as the constant pressure drop $\frac{dp}{dx} = -G$. The pressure drop across each section can be written as:

$$G_0 = \frac{P_1 - P_2}{L_0} \tag{4.4}$$

$$G_1 = -\frac{P_1}{L_1} \tag{4.5}$$

$$G_2 = \frac{P_2}{L_1}. \tag{4.6}$$

The wall velocities at the bottom and the top of the channels $u_{z=0} = u_w^b$ and $u_{z=h} = u_w^t$, respectively. This boundary condition is applied while integrating equation 4.3. The flow profile $u(z)$ obtains the form:

$$u(z) = -\frac{G}{2\mu}\left(z^2 - zh\right) + (u_w^t - u_w^b)\frac{z}{h} + u_w^b. \tag{4.7}$$

The volumetric flow rate $\dot{Q}_i$ (i is the index for each section) is derived by integrating the flow speed over the whole channel height.

$$\dot{Q}_i = \int_0^h u_i(z)dz \tag{4.8}$$

The flow rate through each section is conserved:

$$\dot{Q}_1 = \dot{Q}_2 = \dot{Q}_3 \equiv \dot{Q} \tag{4.9}$$

The boundary condition in the inert inlet and outlet sections is known. Applying $u_w^b = u_w^t = 0$ (non-slip) in the flow rate equation and equation 4.7:

$$\dot{Q}_1 = \frac{1}{12}\frac{G_1}{\mu}h^3 \tag{4.10}$$

$$\dot{Q}_2 = \frac{1}{12}\frac{G_2}{\mu}h^3 \tag{4.11}$$

$$u_1(z) = -\frac{G_1}{2\mu}(z^2 - hz) \tag{4.12}$$

$$u_2(z) = -\frac{G_2}{2\mu}(z^2 - hz) \tag{4.13}$$

The relationship between the pressures in section 1 and 2 is obtained with $\dot{Q}_1 = \dot{Q}_2$:

$$P_1 = P_2 \tag{4.14}$$

$P_2 > 0$ when the fluid flows from the left to the right through the channel. The pressure drop and the flow rate in the active section is:

$$G_0 = -2P_2/L_0 \tag{4.15}$$

$$\dot{Q}_0 = -\frac{P_2}{6\mu L_0}h^3 + \frac{1}{2}\left(u_w^t + u_w^b\right)h \tag{4.16}$$

P_2 is calculated with the conservation of the flow rate in section 1 and 0 with the expression in equation 4.10 and 4.16:

$$P_2 = \frac{6\mu}{h^2}\frac{L_1 L_0}{L_0 + 2L_1}\left(u_w^t + u_w^b\right) \tag{4.17}$$

By inserting P_2 in equation 4.7, we finally get the flow velocity and the flow rate:

$$u(z) = \frac{6L_1}{L_0 + 2L_1}\left(u_w^t + u_w^b\right)\left(\frac{z^2}{h^2} - \frac{z}{h}\right) + \left(u_w^t - u_w^b\right)\frac{z}{h} + u_w^b, \tag{4.18}$$

$$\dot{Q} = \frac{1}{2}\frac{L_0}{L_0 + 2L_1}\left(u_w^t + u_w^b\right)h \tag{4.19}$$

The effect of the micropillars on the active surface introduced a hydrodynamic flow around the pillars which leads to a complex flow profile in the fluid layer containing the micropillars. The flow measurements in a microchannel are thus made in the planes with a distance to the bottom or top wall of more than 5 μm to avoid the underestimation of the flow velocity. Taking this into account, the channel height we use to model the experimental flow profile is smaller than the real channel height, corresponding to the height of the uppermost and lowermost experimental data point. The channel geometry and the wall slip velocity measured as described in section 4.5.1 for each of the three channel configurations are listed in table 4.2.

TABLE 4.2: Parameters used in the theoretical and numerical calculation.

			symmetric	anti-symmetric	skew
active region length	L_0	[μm]	240	240	240
inactive region length	L_1	[μm]	2000	2000	2000
experimental channel height	h_{exp}	[μm]	170	170	110
modeled channel height	h	[μm]	139	155	95
top-wall velocity	u_w^t	[μm/s]	1.74	-1.07	0
Bottom-wall velocity	u_w^b	[μm/s]	2.32	1.81	2.74

Substituting the parameters from the table into equation 4.17, 4.18, 4.19, the flow profile, the flow rate and the pumping pressure for the three channel configurations are obtained.

4.6.1 Symmetric Channel

The flow velocity of the symmetric channel with two active walls facing the same direction:

$$u_{symm}(z) = 12u_w \frac{L_1}{L_0 + 2L_1} \left(\frac{z^2}{h^2} - \frac{z}{h} \right) + u_w \tag{4.20}$$

and the flow rate is:

$$\dot{Q} = u_w h \frac{L_0}{L_0 + 2L_1} \tag{4.21}$$

The pumping pressure is:

$$P_2 = \frac{12u_w\mu}{h^2} \frac{L_1 L_0}{L_0 + 2L_1}. \tag{4.22}$$

4.6.2 Antisymmetric Channel

The flow velocity profile for the antisymmetric channel which consists of two active surfaces facing opposite directions:

$$u_{asymm}(z) = u_w \left(1 - 2\frac{z}{h} \right). \tag{4.23}$$

Because of the oppositely aligned active surfaces, the antisymmetric channel shows no unidirectional pumping and no net flow:

$$P_2 = 0 \tag{4.24}$$

$$\dot{Q} = 0. \tag{4.25}$$

4.6.3 Skew Channel

With one active surface at the bottom and an inert glass slide on top, the channel exhibits a skew parabola profile:

$$u_{skew}(z) = 6u_w \frac{L_1}{L_0 + 2L_1} \left(\frac{z^2}{h^2} - \frac{z}{h} \right) + u_w \left(1 - \frac{z}{h} \right) \tag{4.26}$$

the flow rate is:

$$\dot{Q} = \frac{u_w h}{2} \frac{L_0}{L_0 + 2L_1} \tag{4.27}$$

and the pumping pressure is:

$$P_2 = \frac{6u_w \mu}{h^2} \frac{L_0 L_1}{L_0 + 2L_1}. \tag{4.28}$$

Comparing Eqs. (4.22) to (4.21), it can be concluded that when one active wall is used, the generated pressure and flow rate are half of those generated by the channel with two active walls. With these relationships, one can tune the flow profile or the flow rate simply by changing the channel geometry parameters. For instance, for a symmetric channel, when $L_0 \gg L_1$, $u(z)$ is no more dependent on z, and a flat flow profile can be achieved.

4.7 COMSOL Simulation

To further evaluate the validily of the analytical model developed above, numerical simulations were carried out using COMSOL 5.3. Creeping flow was chosen as the physics model for the study. We set up a 2D geometry with three rectangles representing three main sections, corresponding to the inert-active-inert sections in the microchannel. Two small transition sections are introduced between the inert-active, active-inert sections with a linear slip velocity ramp from 0 μm/s to u_w (inert-active) and from u_w to 0 $\mu m/s$ (active-inert) to offer a transition of the wall slip velocity and avoid numerical instability. The length of both transition sections is 0.5 μm, which is small enough not to considerably influence the simulation results. The left and right side of the channel were defined as inlet and outlet with a pressure $P = 0\ Pa$. The top and bottom walls of the inert sections obey a non-slip velocity boundary condition. At the active walls, sliding wall condition with the corresponding wall velocity is applied. The value of the slip velocities u_w, the height of the fluid in the channel h, the length of the three sections corresponding to the both passive sections L_1 and active illumination section L_0 were chosen as summarised in table 4.2.

The simulation results for the three channel configurations are shown in Fig. 4.23.

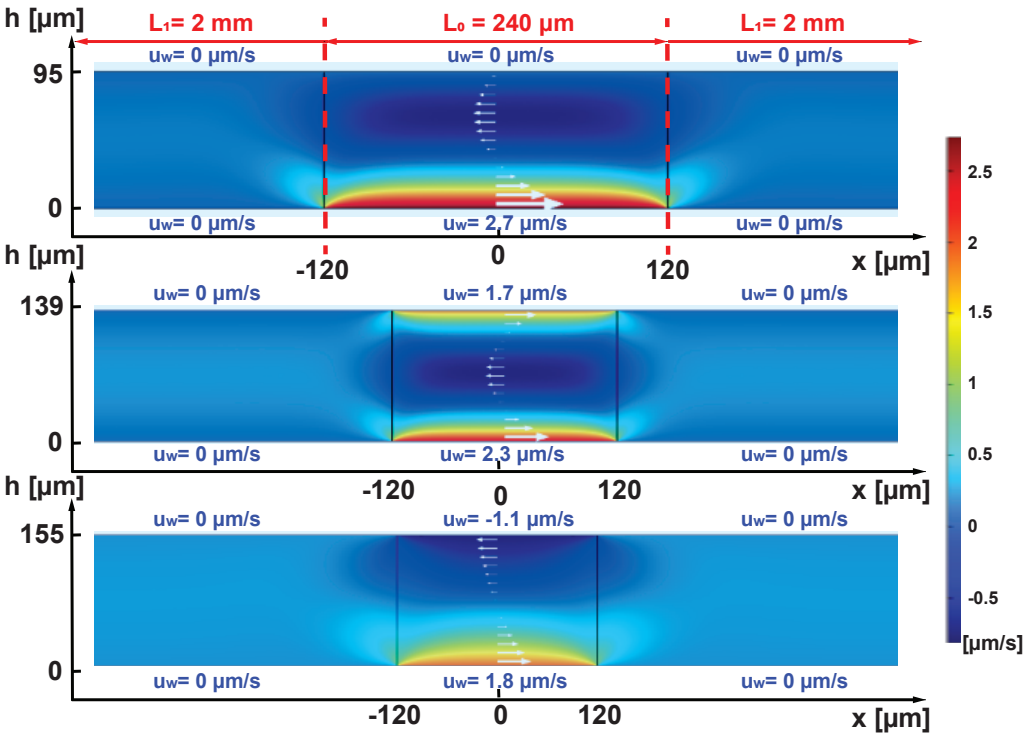

FIGURE 4.23: Illustration of the microfluidic flow profile engineering (a) with bottom surface active pumping (b) with top and bottom surface active pumping in the same direction (c) with top and bottom surface active pumping in opposite directions. Image taken from [98].

The flow profiles for different-sized illumination regions is computed and illustrated in Fig. 4.24. It can be concluded that with a larger illumination region relative to inlet/outlet, the flow profile of a symmetric channel tends to be flatter, as the flow velocity in the middle of the channel is less suppressed by the passive sections.

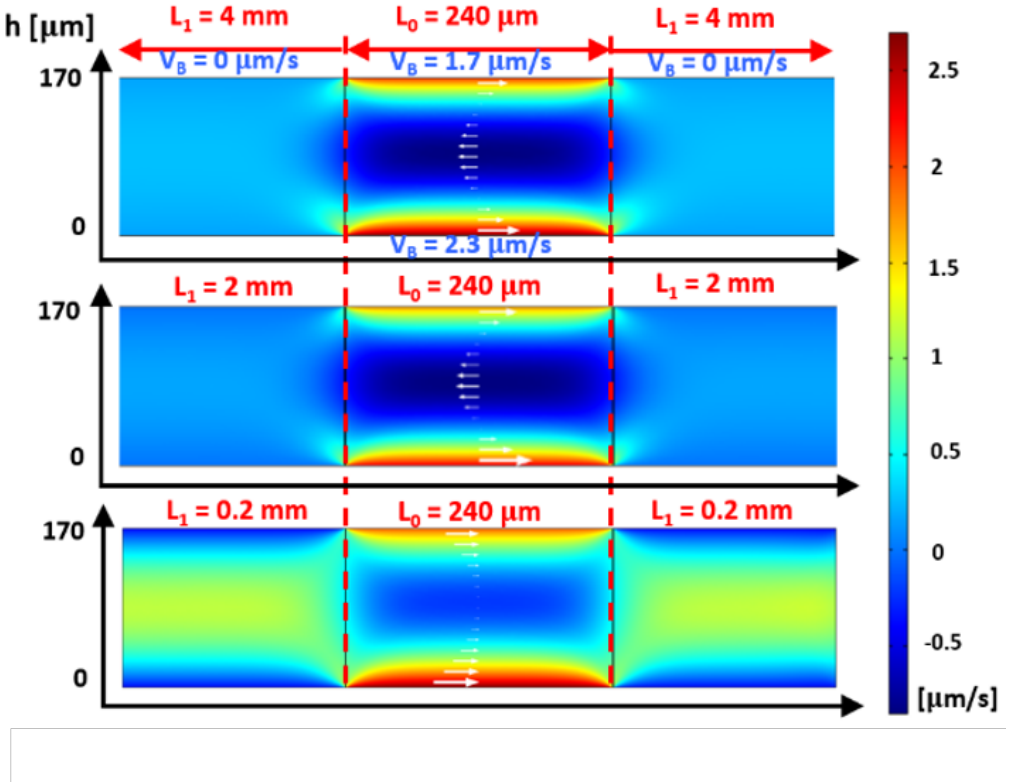

FIGURE 4.24: Simulated hydrodynamic flow profile for different value of L_1 for symmetric channels.

The flow profiles in the active region of the channels with different L_1 value and same slip velocities are plotted in Fig. 4.25.

The flow profiles determined both analytically and numerically agree well with the experimentally measured data, and are compared in Fig. 4.26. This demonstrates that the model captures the main physical ingredients, and provides additional support for the suggested flow profile manipulation in a microfluidic channel.

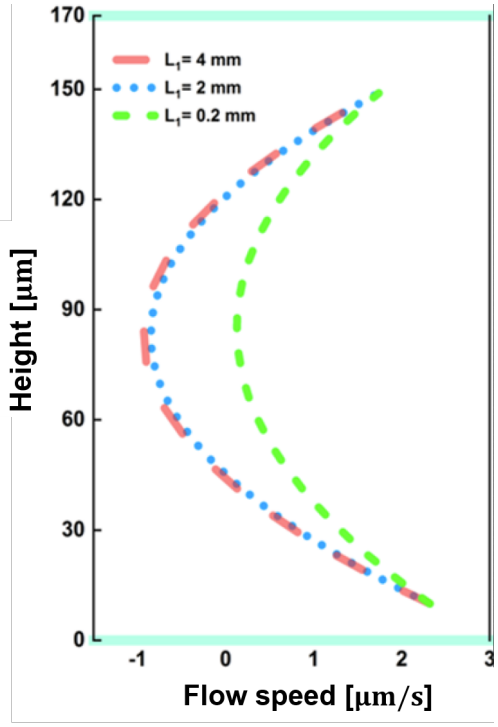

FIGURE 4.25: Flow profiles at x = 0 µm within the symmetric channels with the same slip velocities, different inert section length L_1.

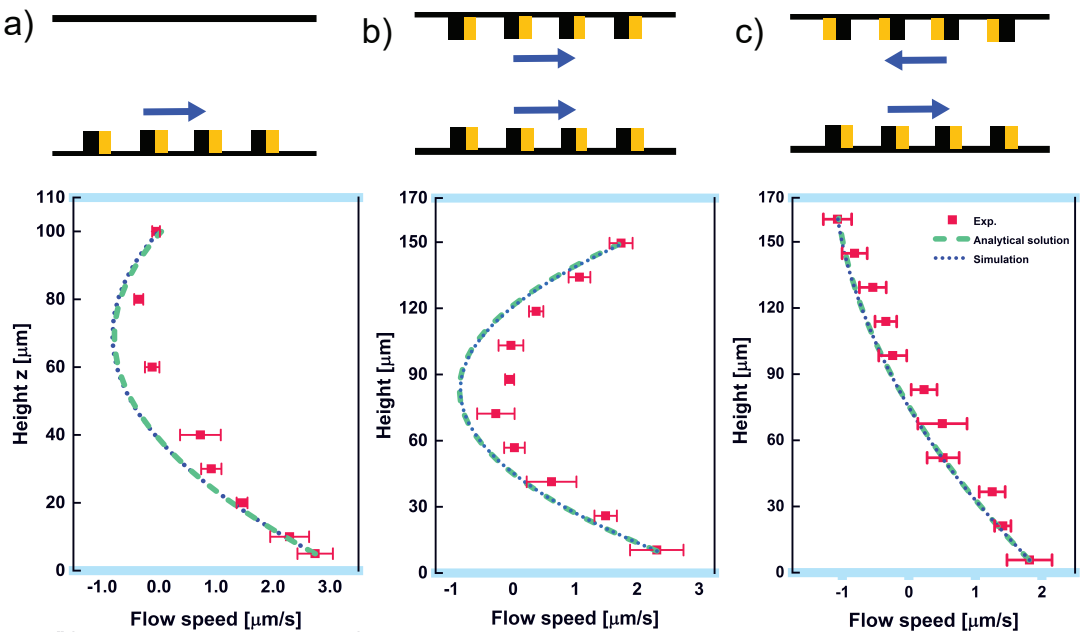

FIGURE 4.26: Adjustment of the fluidic profile by the surface pump. Blue upper and bottom lines in the graphs indicating the top and bottom surface of the microfluidic channel (a). The cross section flow profile when the bottom surface of the channel is structured with Janus micropillars, (b) when both top and bottom surfaces are structured with Janus micropillars with the same direction, (c) with the opposite direction. Image adapted from [98].

4.8 Conclusion

In this chapter, we have demonstrated that surfaces decorated with photocatalytically active SiO_2/ TiO_2 micropillar array can pump 2 % H_2O_2 solution, with Au/ SiO_2/ TiO_2 micropillar array can pump water. These active self-pumping surfaces can be used for wireless microfluidic channel pumping, which pumps H_2O_2 and/or water along the channel. The pumping is fully controlled by the external UV illumination and adjustable by changing the UV intensity. The pumping direction is determined by the geometry of the micropillars. A local self-osmotic flow is created by photocatalytic water decomposition reaction at each micropillar. The local flows couple and form a macroscopic fluid flow, which shows a speed up to 4 μm/s and is comparable to the fastest existing water chemical pumps. The interplay between immobilized Janus pillars is also investigated by changing the spacing between the pillars in order to optimize the arrangement of the array. Surfaces with 2D Janus structures and 3D Janus bars are also prepared and measured. These structures exhibit less efficient pumping performance as the 3D micro pillar structure.

By fixing the active surfaces as walls to a microchannel, fluid can be pumped without external physical pressure driving devices and tubes. For a 240 μm long active channel, we generate a pressure gradient of 1 μPa/μm that drives a volume flow rate of 4 pl/s through the 4.24 mm long microchannel. With the help of an analytical model and numerical simulation, it was shown that not only the fluid can be transported, the fluid profile can also be tailored with different channel structures. A symmetric channel with much longer L_1 than L_0, indicates a back flow at the centerline as the long inert region within the channel provides a high flow resistance. The centerline velocity is minimal with a value of $u = -u_w/2$ when $L_1/L_0 \to \infty$, while the flow profile can be tuned flat when the entire channel is set to be active ($L_1/L_0 \to 0$). By using the defocusing method, fluid flow profiles in a microchannel could be shaped with the help of tracer particles. A variety of flow profiles can be realised, which are not possible in conventional pressure-driven flows.

Volumetric pumping in a PDMS microfluidic channel embedded with our active surface is demonstrated. With one active wall at the bottom, a 100 μm wide, 100 μm high channel is able to pump water forward with a volume flow rate of 4 pl/s, when 240 μm in a 4 mm long channel is illuminated.

Chapter 5

Summary and Outlook

In this thesis, the fundamental behaviour of chemically active particles at the micro scale is investigated and utilized for some new applications. As a typical artificial micro motor alternative, chemical micromotors harvest chemical energy from the environment and propel themselves via catalytic reactions and to generate self-propelled motion.

Unlike the swimming in the macroscopic world where a time-reversible motion can lead to propulsion in the fluid, the object at the micro scale cannot achieve such a motion just by a reciprocal movement at low Re number regime. Inertia plays an extremely small role in comparison with the viscous drag for a micro sized object in fluid. To overcome the dominant viscous resistance and to generate motion, an external energy input is required. This can be provided by magnetic, electric, acoustic, light sources. Alternately, the energy can come from a chemical reaction, which generates a local chemical gradient. Chemical reactions are used to propel the micromotors and to induce flow in this thesis. This, so called self-phoresis, is generated for asymmetric microstructures made from photochemically-active TiO_2. The external light source can trigger and control the chemical reaction on the microparticle.

In this thesis, a new route to obtain asymmetric chemical micromotors is presented. The attractive interaction of a photochemically active species and a passive species (colloid) is used to form a dimer structure. In this way, the particles spontaneously form an asymmetric dimer. This symmetry breaking in turn results in a Janus structure and the self-propulsion of the dimer. The propelling velocity can be controlled with the external light stimulus. The mechanism of the dimer formation is identified to be due to diffusiophoresis. The optimum size ratio of active and passive particle is investigated. A repulsive interaction between active TiO_2 particles ensures that dimers do not easily aggregate.

Based on the property of the osmotic flow, a novel method to realize a chemical

pump is realized. An array of the chemical motor: asymmetric Janus micropillars are immobilized on a surface such that the osmotic flow of neighbouring microstructures couples such that a macroscopic flow is generated. Such a substrate is able to pump the fluid directionally depending on the alignment of the micro pillars in the array. In this thesis, TiO_2 and Au Janus micropillars can split water when illuminated and thus pump water. By assembling two active surfaces in one channel as top and bottom substrate, the fluid flow profile can be tailored. An analytical model and numerical simulations are presented, both show good agreement with the experimental results. Compared to conventional microfluidic pumps, the chemical pump of this thesis has the advantage that it is untethered and that it can be controlled by light, The fluid flow profile is adjustable. The role of the shape and spacing of the microstructures is examined and it is found that the 3D structure of the catalytically active Janus structures near the wall is critical for the fluid pumping.

As heterogeneous biphasic Janus micromotors are hard to be fabricated either by PVD, CVD or chemical synthesis, the dimer formation is promising and could ultimately be used to produce many self-assembled Janus micromotors.

Chromatography is being used for the separation of mixtures while they travel at different velocities in the fluid. For separation it is helpful if the fluid has a flat flow profile across the channel so that the same component can reach the exit at the same time. Whereas the non-slip wall boundary condition in a "normal" pressure driven channel in column chromatography has the well known parabolic fluid profile. The chemically active pumping wall is a practical solution for this problem. By integrating the chemically active microstructures on the wall of the tube, the channel fluid profile can be easily and precisely adjusted to form a flat profile.

Another exciting outlook is that the chemically based pump can theoretically be miniaturized to sub-nano size so that the separation of single macromolecule, sequencing of DNA, etc, can be realized. This application is constrained by two factors. One is the resolution limitation in the fabrication process, given that 30 nm Janus structures have been so far the smallest Janus structures that are fabricated using the same technique [119]. At this scale, the active particles also show strong Brownian motion. Janus particles show generally clearly measurable active propulsion down to 100 nm, and we expect it to be the size limit for pumping with Janus pillars. Besides, the two active surfaces should not be assembled too close that the chemical cross-talk from the opposite interfaces cancels the chemical gradient. A channel with a channel height of

300 nm should be able to provide a reasonable bulk fluid pumping. It remains for future work to integrate the self-pumping walls in a real microfluidic device and to establish size limits.

Bibliography

[1] P. Fischer et al., *Nanoparticles and nanmotors: properties and materials, Lecture notes, lecture 101410, Univ. of Stuttgart*. unpublished, Apr. 2020.

[2] C. K. Batchelor and G. K. Batchelor, *An Introduction to Fluid Dynamics*. Massachusetts: Cambridge University Press, 1967.

[3] E. M. Purcell, "Life at low reynolds number", *Journal of Biological Chemistry*, vol. 45, p. 3, 1977.

[4] D. B. Dusenbery, *Living at micro scale*. Massachusetts: Harvard University Press, 2011.

[5] A. Einstein, "Über die von der molekularkinetischen theorie der wärme geforderte bewegung von in ruhenden flüssigkeiten suspendierten teilchen", *Annalen der Physik*, vol. 322, no. 8, pp. 549–560, 1905.

[6] J. L. Anderson, "Transport mechanisms of biological colloidsa", *Annals of the New York Academy of Sciences*, vol. 469, no. 1, pp. 166–177, 1986.

[7] P. W. Atkins and J. D. Paula, *Physical Chemistry*. Oxford: Oxford University Press, 2006.

[8] J. Ignacio Tinoco, K. Sauer, and J. C. Wang, *Physical Chemistry-Principles And Applications In Biological Sciences*. New Jersey: Prentice Hall, 1995.

[9] C. Bechinger, R. Di Leonardo, H. Löwen, C. Reichhardt, G. Volpe, and G. Volpe, "Active particles in complex and crowded environments", *Reviews of Modern Physics*, vol. 88, no. 4, p. 045 006, 2016.

[10] D. Yamamoto and A. Shioi, "Self-Propelled Nano/Micromotors with a Chemical Reaction: Underlying Physics and Strategies of Motion Control", *KONA Powder and Particle Journal*, vol. 32, no. 0, pp. 2–22, 2015.

[11] W. Gao, X. Feng, A. Pei, Y. Gu, J. Li, and J. Wang, "Seawater-driven magnesium based Janus micromotors for environmental remediation", *Nanoscale*, vol. 5, no. 11, pp. 4696–4700, May 2013, Publisher: The Royal Society of Chemistry.

[12] W. Gao, A. Pei, and J. Wang, "Water-Driven Micromotors", *ACS Nano*, vol. 6, no. 9, pp. 8432–8438, Sep. 2012.

[13] R. Liu and A. Sen, "Autonomous Nanomotor Based on Copper–Platinum Segmented Nanobattery", *Journal of the American Chemical Society*, vol. 133, no. 50, pp. 20 064–20 067, Dec. 2011.

[14] W. F. Paxton, K. C. Kistler, C. C. Olmeda, A. Sen, S. K. St. Angelo, Y. Cao, T. E. Mallouk, P. E. Lammert, and V. H. Crespi, "Catalytic Nanomotors: Autonomous Movement of Striped Nanorods", *Journal of the American Chemical Society*, vol. 126, no. 41, pp. 13 424–13 431, Oct. 2004.

[15] W. F. Paxton, S. Sundararajan, T. E. Mallouk, and A. Sen, "Chemical Locomotion", *Angewandte Chemie International Edition*, vol. 45, no. 33, pp. 5420–5429, 2006.

[16] T. R. Kline, W. F. Paxton, Y. Wang, D. Velegol, T. E. Mallouk, and A. Sen, "Catalytic Micropumps: Microscopic Convective Fluid Flow and Pattern Formation", *Journal of the American Chemical Society*, vol. 127, no. 49, pp. 17 150–17 151, Dec. 2005, Publisher: American Chemical Society.

[17] J. L. Moran and J. D. Posner, "Electrokinetic locomotion due to reaction-induced charge auto-electrophoresis", *Journal of Fluid Mechanics*, vol. 680, pp. 31–66, Aug. 2011.

[18] R. F. Ismagilov, A. Schwartz, N. Bowden, and G. M. Whitesides, "Autonomous Movement and Self-Assembly", *Angewandte Chemie International Edition*, vol. 41, pp. 652–654, 2002.

[19] *Examples of semiconductor materials*. [Online]. Available: `https://en.wikipedia.org/wiki/List_of_semiconductor_materials`, (accessed: 03.05.2021).

[20] *Electronic archive new semiconductor materials. characteristics and properties*, 2015. [Online]. Available: `http://www.ioffe.ru/SVA/NSM/Semicond/`, (accessed: 22.11.2020).

[21] P. C. Safa Kasap, *Handbook of Electronic and Photonic Materials*. Springer US, 2007.

[22] N. Rahimi, R. A. Pax, and E. M. Gray, "Review of functional titanium oxides. I: TiO_2 and its modifications", *Progress in Solid State Chemistry*, vol. 44, no. 3, pp. 86–105, Sep. 2016.

[23] A. Fujishima and K. Honda, "Electrochemical Photolysis of Water at a Semiconductor Electrode", *Nature*, vol. 238, no. 5358, pp. 37–38, Jul. 1972, Number: 5358 Publisher: Nature Publishing Group.

[24] K. Nakata and A. Fujishima, "TiO_2 photocatalysis: Design and applications", *Journal of Photochemistry and Photobiology C: Photochemistry Reviews*, vol. 13, no. 3, pp. 169–189, Sep. 2012.

[25] H. P. Suryawanshi, S. G. Bachhav, and D. R. Patil, "The effect of adsorbed hydroxyl content on the surface of TiO_2 nanorod array and its photocatalytic degradation study", *Current Catalysis*, vol. 7, no. 3, pp. 224–235, 2018.

[26] A. Fujishima, X. Zhang, and D. A. Tryk, "TiO_2 photocatalysis and related surface phenomena", *Surface Science Reports*, vol. 63, no. 12, pp. 515–582, Dec. 2008.

[27] S. G. Kumar and L. G. Devi, "Review on Modified TiO_2 Photocatalysis under UV/Visible Light: Selected Results and Related Mechanisms on Interfacial Charge Carrier Transfer Dynamics", *The Journal of Physical Chemistry A*, vol. 115, no. 46, pp. 13 211–13 241, Nov. 2011.

[28] M. Ni, M. K. H. Leung, D. Y. C. Leung, and K. Sumathy, "A review and recent developments in photocatalytic water-splitting using TiO_2 for hydrogen production", *Renewable and Sustainable Energy Reviews*, vol. 11, no. 3, pp. 401–425, Apr. 2007.

[29] G. Burgeth and H. Kisch, "Photocatalytic and photoelectrochemical properties of titania–chloroplatinate(IV)", *Coordination Chemistry Reviews*, vol. 230, no. 1, pp. 41–47, 2002.

[30] A. Wood, M. Giersig, and P. Mulvaney, "Fermi level equilibration in quantum dotmetal nanojunctions", *The Journal of Physical Chemistry B*, vol. 105, no. 37, pp. 8810–8815, 2001.

[31] M. Jakob, H. Levanon, and P. V. Kamat, "Charge distribution between UV-irradiated TiO_2 and gold nanoparticles: determination of shift in the fermi level", *Nano Letters*, vol. 3, no. 3, pp. 353–358, 2003.

[32] V. Subramanian, E. E. Wolf, and P. V. Kamat, "Green emission to probe photoinduced charging events in ZnO- Au nanoparticles. charge distribution and fermi-level equilibration", *The Journal of Physical Chemistry B*, vol. 107, no. 30, pp. 7479–7485, 2003.

[33] S. Chen and R. W. Murray, "Electrochemical quantized capacitance charging of surface ensembles of gold nanoparticles", *The Journal of Physical Chemistry B*, vol. 103, no. 45, pp. 9996–10 000, 1999.

[34] V. Subramanian, E. E. Wolf, and P. V. Kamat, "Catalysis with TiO_2/Gold Nanocomposites. Effect of Metal Particle Size on the Fermi Level Equilibration", *Journal of the American Chemical Society*, vol. 126, no. 15, pp. 4943–4950, Apr. 2004, Publisher: American Chemical Society.

[35] M. T. Nenadovic, T. Rajh, O. I. Micic, and A. J. Nozik, "Electron transfer reactions and flat-band potentials of tungsten(VI) oxide colloids", *The Journal of Physical Chemistry*, vol. 88, no. 24, pp. 5827–5830, 1984.

[36] N. M. Dimitrijevic, D. Savic, O. I. Micic, and A. J. Nozik, "Interfacial electron-transfer equilibria and flatband potentials of .alpha.-ferric oxide and titanium dioxide colloids studied by pulse radiolysis", *The Journal of Physical Chemistry*, vol. 88, no. 19, pp. 4278–4283, 1984.

[37] M. Saquib, M. Abu Tariq, M. Faisal, and M. Muneer, "Photocatalytic degradation of two selected dye derivatives in aqueous suspensions of titanium dioxide", *Desalination*, vol. 219, no. 1, pp. 301–311, Jan. 2008.

[38] M. Muneer, M. Qamar, M. Saquib, and D. W. Bahnemann, "Heterogeneous photocatalysed reaction of three selected pesticide derivatives, propham, propachlor and tebuthiuron in aqueous suspensions of titanium dioxide", *Chemosphere*, vol. 61, no. 4, pp. 457–468, Oct. 2005.

[39] M. M. Haque and M. Muneer, "Heterogeneous photocatalysed degradation of a herbicide derivative, isoproturon in aqueous suspension of titanium dioxide", *Journal of Environmental Management*, vol. 69, no. 2, pp. 169–176, Oct. 2003.

[40] A. Rodríguez, R. Rosal, J. A. Perdigón-Melón, M. Mezcua, A. Agüera, M. D. Hernando, P. Letón, A. R. Fernández-Alba, and E. García-Calvo, "Ozone-Based Technologies in Water and Wastewater Treatment", in *Emerging Contaminants from Industrial and Municipal Waste*, D. Barceló and M. Petrovic, Eds., vol. 5S/2, Berlin, Heidelberg: Springer Berlin Heidelberg, 2008.

[41] A. Syoufian and K. Nakashima, "Degradation of methylene blue in aqueous dispersion of hollow titania photocatalyst: Study of reaction enhancement by various electron scavengers", *Journal of Colloid and Interface Science*, vol. 317, no. 2, pp. 507–512, Jan. 2008.

[42] M. Bonnet, C. Massard, P. Veisseire, O. Camares, and K. O. Awitor, "Environmental Toxicity and Antimicrobial Efficiency of Titanium Dioxide Nanoparticles in Suspension", *Journal of Biomaterials and Nanobiotechnology*, vol. 6, no. 3, pp. 213–224, May 2015, Publisher: Scientific Research Publishing.

[43] D. T. Cromer and K. Herrington, "The Structures of Anatase and Rutile", *Journal of the American Chemical Society*, vol. 77, no. 18, pp. 4708–4709, Sep. 1955, Publisher: American Chemical Society.

[44] W. H. Bauer, "Atomabstände und Bindungswinkel im Brookit, TiO_2", *Acta Cryst.*, 1961.

[45] X. Chen and S. S. Mao, "Titanium dioxide nanomaterials: Synthesis, properties, modifications, and applications", *Chemical Reviews*, vol. 107, no. 7, pp. 2891–2959, 2007.

[46] T. L. Thompson and J. T. Yates, "Surface Science Studies of the Photoactivation of TiO_2 New Photochemical Processes", *Chemical Reviews*, vol. 106, no. 10, pp. 4428–4453, 2006.

[47] U. Diebold, "The surface science of titanium dioxide", *Surface Science Reports*, vol. 48, no. 5, pp. 53 –229, 2003.

[48] S.-D. Mo and W. Y. Ching, "Electronic and optical properties of three phases of titanium dioxide: Rutile, anatase, and brookite", *Physical Review B*, vol. 51, no. 19, pp. 13 023–13 032, May 1995, Publisher: American Physical Society.

[49] J. Muscat, V. Swamy, and N. M. Harrison, "First-principles calculations of the phase stability of TiO_2", *Physical Review B*, vol. 65, no. 22, p. 224 112, Jun. 2002, Publisher: American Physical Society.

[50] K. Tanaka, M. F. V. Capule, and T. Hisanaga, "Effect of crystallinity of TiO_2 on its photocatalytic action", *Chemical Physics Letters*, vol. 187, no. 1, pp. 73–76, Nov. 1991.

[51] L. Andronic, D. Perniu, and A. Duta, "Synergistic effect between tio_2 sol–gel and degussa p25 in dye photodegradation", *Journal of Sol-Gel Science and Technology*, vol. 66, pp. 472–480, Jun. 2013.

[52] T. Luttrell, S. Halpegamage, J. Tao, A. Kramer, E. Sutter, and M. Batzill, "Why is anatase a better photocatalyst than rutile? - model studies on epitaxial TiO_2 films", *Scientific Reports*, vol. 4, no. 1, p. 4043, Feb. 10, 2014.

[53] P. Somasundaran, *Encyclopedia of Surface And Colloid Science, Volume 2*. CRC Press, 2006.

[54] I. Buttinoni, "Self-propelled particles driven by light", PhD thesis, University of Stuttgart, 2014.

[55] R. Piazza, "Thermophoresis: Moving particles with thermal gradients", *Soft Matter*, vol. 4, no. 9, p. 1740, 2008.

[56] H. J. V. Tyrrell, *Diffusion and Heat Flow In Liquids*. London, Butterworths, 1961.

[57] J. L. Moran, "7 - robotic colloids: Engineered self-propulsion at the microscale (and smaller)", in *Robotic Systems and Autonomous Platforms*, ser. Woodhead Publishing in Materials, S. M. Walsh and M. S. Strano, Eds., Woodhead Publishing, 2019.

[58] J. L. Anderson, "Colloid Transport by Interfacial Forces", *Annual Review of Fluid Mechanics*, vol. 21, no. 1, pp. 61–99, 1989.

[59] N. B. Derjaguin, V. V. Churaev, and V. M. Muller, *Surface Forces*. Boston, MA: Springer, 1987.

[60] R. J. Hunter, *Zeta Potential in Colloid Science*. Elsevier Press, 1981.

[61] Y. Ye, J. Luan, M. Wang, Y. Chen, D. Wilson, F. Peng, and Y. Tu, "Fabrication of Self-Propelled Micro- and Nanomotors Based on Janus Structures", *Chemistry - A European Journal*, Apr. 2019.

[62] H.-R. Jiang, N. Yoshinaga, and M. Sano, "Active Motion of a Janus Particle by Self-Thermophoresis in a Defocused Laser Beam", *Physical Review Letters*, vol. 105, no. 26, p. 268 302, Dec. 2010, Publisher: American Physical Society.

[63] S. Gangwal, O. J. Cayre, M. Z. Bazant, and O. D. Velev, "Induced-charge electrophoresis of metallodielectric particles", *Physical Review Letters*, vol. 100, no. 5, p. 058 302, 2008.

[64] T.-Y. Chiang and D. Velegol, "Multi-ion diffusiophoresis", *Journal of Colloid and Interface Science*, vol. 424, pp. 120–123, Jun. 2014.

[65] J. R. Howse, R. A. L. Jones, A. J. Ryan, T. Gough, R. Vafabakhsh, and R. Golestanian, "Self-Motile Colloidal Particles: From Directed Propulsion to Random Walk", *Physical Review Letters*, p. 4, 2007.

[66] F. Mou, L. Kong, C. Chen, Z. Chen, L. Xu, and J. Guan, "Light-controlled propulsion, aggregation and separation of water-fuelled TiO_2/Pt Janus submicromotors and their "on-the-fly" photocatalytic activities", *Nanoscale*, vol. 8, no. 9, 2016.

[67] R. Dong, Q. Zhang, W. Gao, A. Pei, and B. Ren, "Highly Efficient Light-Driven TiO_2–Au Janus Micromotors", *ACS Nano*, vol. 10, no. 1, pp. 839–844, Jan. 2016, Publisher: American Chemical Society.

[68] M. Safdar, S. U. Khan, and J. Jänis, "Progress toward catalytic micro- and nanomotors for biomedical and environmental applications", *Advanced Materials*, vol. 30, no. 24, p. 1 703 660, 2018.

[69] J. Palacci, S. Sacanna, S.-H. Kim, G.-R. Yi, D. J. Pine, and P. M. Chaikin, "Light-activated self-propelled colloids", *Philosophical Transactions of the Royal Society A: Mathematical, Physical and Engineering Sciences*, vol. 372, no. 2029, p. 20 130 372, 2014.

[70] N.-T. Nguyen, S. A. M. Shaegh, N. Kashaninejad, and D.-T. Phan, "Design, fabrication and characterization of drug delivery systems based on lab-on-a-chip technology", *Advanced Drug Delivery Reviews*, vol. 65, no. 11, pp. 1403–1419, 2013.

[71] H. Moghadas, M. S. Saidi, N. Kashaninejad, and N.-T. Nguyen, "Challenge in particle delivery to cells in a microfluidic device", *Drug Delivery and Translational Research*, vol. 8, no. 3, pp. 830–842, 2018.

[72] T. Dinh, H.-P. Phan, N. Kashaninejad, T.-K. Nguyen, D. V. Dao, and N.-T. Nguyen, "An on-chip SiC MEMS device with integrated heating, sensing, and microfluidic cooling systems", *Advanced Materials Interfaces*, vol. 5, no. 20, p. 1 800 764, 2018.

[73] A. Gerami, Y. Alzahid, P. Mostaghimi, N. Kashaninejad, F. Kazemifar, T. Amirian, N. Mosavat, M. Ebrahimi Warkiani, and R. T. Armstrong, "Microfluidics for porous systems: Fabrication, microscopy and applications", *Transport in Porous Media*, vol. 130, no. 1, pp. 277–304, 2019.

[74] M. Barisam, M. S. Saidi, N. Kashaninejad, R. Vadivelu, and N.-T. Nguyen, "Numerical simulation of the behavior of toroidal and spheroidal multicellular aggregates in microfluidic devices with microwell and u-shaped barrier", *Micromachines*, vol. 8, no. 12, 2017.

[75] M. Barisam, M. S. Saidi, N. Kashaninejad, and N.-T. Nguyen, "Prediction of necrotic core and hypoxic zone of multicellular spheroids in a microbioreactor with a u-shaped barrier", *Micromachines*, vol. 9, no. 3, 2018.

[76] N. Kashaninejad, N.-T. Nguyen, and W. K. Chan, "Eccentricity effects of microhole arrays on drag reduction efficiency of microchannels with a hydrophobic wall", *Physics of Fluids*, vol. 24, no. 11, p. 112 004, 2012.

[77] N.-T. Nguyen, M. Hejazian, C. H. Ooi, and N. Kashaninejad, "Recent advances and future perspectives on microfluidic liquid handling", *Micromachines*, vol. 8, no. 6, p. 186, 2017.

[78] N. Kashaninejad, "A new form of velocity distribution in rectangular microchannels with finite aspect ratios", unpublished, 2019.

[79] F. M. White, *Viscous fluid flow*. New York: McGraw-Hill, 1991.

[80] S. P. Sutera and R. Skalak, "The History of Poiseuille's Law", *Annu. Rev. Fluid Mech.*, vol. 25, pp. 1–20, 1993.

[81] *Derivation of hagen-poiseuille equation for pipe flows with friction*. [Online]. Available: `https://www.tec-science.com/mechanics/gases-and-liquids/hagen-poiseuille-equation-for-pipe-flows-with-friction/`, (accessed: 03.05.2021).

[82] R. K. Shah, *Laminar flow forced convection in ducts: a source book for compact heat exchanger analytical data*. New York: Academic Press, 1978.

[83] M. Spiga and G. L. Morino, "A symmetric solution for velocity profile in laminar flow through rectangular ducts", *International Communications in Heat and Mass Transfer*, vol. 21, no. 4, pp. 469–475, 1994.

[84] A. A. Avramenko, A. I. Tyrinov, and I. V. Shevchuk, "Start-up slip flow in a microchannel with a rectangular cross section", *Theoretical and Computational Fluid Dynamics*, vol. 29, no. 5, pp. 351–371, 2015.

[85] N. H. Asmar, *Partial Differential Equations with Fourier Series and Boundary Value Problems*. New Jersey: Prentice Hall, 2005.

[86] H. Bruus, "Acoustofluidics 1: Governing equations in microfluidics", *Lab on a Chip*, vol. 11, no. 22, pp. 3742–3751, 2011.

[87] T. Yu, P. Chuphal, S. Thakur, S. Y. Reigh, D. P. Singh, and P. Fischer, "Chemical Micromotors Self-Assemble and Self-Propel by Spontaneous Symmetry Breaking", *Chem. Commun. (Cambridge, U. K.)*, vol. 54, pp. 11 933–11 936, Oct. 2018.

[88] J. Wang, *Nanomachines: Fundamentals and Applications*. Wiley VCH, 2013.

[89] W. Wang, W. Duan, S. Ahmed, T. E. Mallouk, and A. Sen, "Small power: Autonomous nano- and micromotors propelled by self-generated gradients", *Nano Today*, vol. 8, no. 5, pp. 531–554, Oct. 2013.

[90] D. P. Singh, U. Choudhury, P. Fischer, and A. G. Mark, "Non-Equilibrium Assembly of Light-Activated Colloidal Mixtures", *Advanced Materials*, vol. 29, no. 32, p. 1 701 328, 2017.

[91] B. V. Derjaguin, G. P. Sidorenkov, E. A. Zubashchenkov, and E. V. Kiseleva, "Kinetic phenomena in boundary films of liquids", *Kolloidn. Zh.*, vol. 9, pp. 335–347, 1947.

[92] P. H. Colberg, S. Y. Reigh, B. Robertson, and R. Kapral, "Chemistry in Motion: Tiny Synthetic Motors", *Accounts of Chemical Research*, vol. 47, no. 12, pp. 3504–3511, Dec. 2014, Publisher: American Chemical Society.

[93] A. Brown and W. Poon, "Ionic effects in self-propelled Pt-coated Janus swimmers", *Soft Matter*, vol. 10, no. 22, pp. 4016–4027, May 2014, Publisher: The Royal Society of Chemistry.

[94] J. Palacci, S. Sacanna, A. P. Steinberg, D. J. Pine, and P. M. Chaikin, "Living Crystals of Light-Activated Colloidal Surfers", *Science*, vol. 339, no. 6122, pp. 936–940, Feb. 2013, Publisher: American Association for the Advancement of Science Section: Report.

[95] A. Malevanets and R. Kapral, "Mesoscopic model for solvent dynamics", *The Journal of Chemical Physics*, vol. 110, no. 17, pp. 8605–8613, May 1999.

[96] S. Y. Reigh, P. Chuphal, S. Thakur, and R. Kapral, "Diffusiophoretically induced interactions between chemically active and inert particles", *Soft Matter*, vol. 14, no. 29, pp. 6043–6057, Jul. 2018, Publisher: The Royal Society of Chemistry.

[97] L. Li and H. Zeng, "Marine mussel adhesion and bio-inspired wet adhesives", *Biotribology*, vol. 5, pp. 44–51, Mar. 2016.

[98] T. Yu, A. G. Athanassiadis, M. N. Popescu, V. Chikkadi, A. Güth, D. P. Singh, T. Qiu, and P. Fischer, "Microchannels with Self-Pumping Walls", *ACS Nano*, vol. 14, no. 10, pp. 13 673–13 680, Oct. 2020, Publisher: American Chemical Society.

[99] J. G. Gibbs and Y.-P. Zhao, "Autonomously motile catalytic nanomotors by bubble propulsion", *Applied Physics Letters*, vol. 94, no. 16, p. 163 104, Apr. 2009, Publisher: American Institute of Physics.

[100] J.-W. Kim, T. Suzuki, S. Yokota, and K. Edamura, "Tube-type micropump by using electro-conjugated fluid (ECF)", *Sensors and Actuators A: Physical*, vol. 174, pp. 155–161, 2012.

[101] W. F. Paxton, P. T. Baker, T. R. Kline, Y. Wang, T. E. Mallouk, and A. Sen, "Catalytically Induced Electrokinetics for Motors and Micropumps", *J. Am. Chem. Soc.*, vol. 128, pp. 14 881–14 888, Nov. 2006.

[102] X. Ma, A. Jannasch, U.-R. Albrecht, K. Hahn, A. Miguel-López, E. Schäffer, and S. Sánchez, "Enzyme-Powered Hollow Mesoporous Janus Nanomotors", *Nano Lett.*, vol. 15, pp. 7043–7050, Oct. 2015.

[103] A. A. Farniya, M. J. Esplandiu, D. Reguera, and A. Bachtold, "Imaging the Proton Concentration and Mapping the Spatial Distribution of the Electric Field of Catalytic Micropumps", *Phys. Rev. Lett.*, vol. 111, p. 168 301, Oct. 2013.

[104] M. J. Esplandiu, A. Afshar Farniya, and A. Bachtold, "Silicon-Based Chemical Motors: An Efficient Pump for Triggering and Guiding Fluid Motion Using Visible Light", *ACS Nano*, vol. 9, pp. 11 234–11 240, 2015.

[105] D. Patra, H. Zhang, S. Sengupta, and A. Sen, "Dual Stimuli-Responsive, Rechargeable Micropumps *via* "Host–Guest" Interactions", *ACS Nano*, vol. 7, pp. 7674–7679, Sep. 2013.

[106] M. Alarcón-Correa, J.-P. Günther, J. Troll, V. M. Kadiri, J. Bill, P. Fischer, and D. Rothenstein, "Self-Assembled Phage-Based Colloids for High Localized Enzymatic Activity", *ACS Nano*, vol. 13, pp. 5810–5815, May 2019.

[107] R.-E. Munteanu, M. N. Popescu, and S. Gáspár, "Glucose Oxidase Micropumps: Multi-Faceted Effects of Chemical Activity on Tracer Particles near the Solid–Liquid Interface", *Condens. Matter*, vol. 4, p. 73, Sep. 2019.

[108] R. Niu and T. Palberg, "Seedless assembly of colloidal crystals by inverted micro-fluidic pumping", *Soft Matter*, vol. 14, pp. 3435–3442, May 2018.

[109] S. Michelin and E. Lauga, "A reciprocal theorem for boundary-driven channel flows", *Phys. Fluids*, vol. 27, p. 111 701, Nov. 2015.

[110] D. J. Laser and J. G. Santiago, "A review of micropumps", *Journal of Micromechanics and Microengineering*, vol. 14, no. 6, R35–R64, Apr. 2004.

[111] D. J. Beebe, G. A. Mensing, and G. M. Walker, "Physics and Applications of Microfluidics in Biology", *Annual Review of Biomedical Engineering*, vol. 4, no. 1, pp. 261–286, Aug. 2002, Publisher: Annual Reviews.

[112] B. D. Iverson and S. V. Garimella, "Recent advances in microscale pumping technologies: A review and evaluation", *Microfluid. Nanofluid.*, vol. 5, pp. 145–174, Aug. 2008.

[113] X. Wang, C. Cheng, S. Wang, and S. Liu, "Electroosmotic pumps and their applications in microfluidic systems", *Microfluid. Nanofluid.*, vol. 6, pp. 145–162, Feb. 2009.

[114] N. Pamme, "Magnetism and microfluidics", *Lab-on-a-Chip*, vol. 6, pp. 24–38, 2006.

[115] K. Yoshida, T. Sato, S. I. Eom, J.-w. Kim, and S. Yokota, "A study on an AC electroosmotic micropump using a square pole – Slit electrode array", *Sens. Actuators*, vol. 265, pp. 152–160, 2017.

[116] *Confocal and wide microscopy comparison*. [Online]. Available: `https://www.labclinics.com/en/if-imaging-widefield-versus-confocal-microscopy/`, (accessed: 22.11.2020).

[117] K. M. Taute, S. Gude, S. J. Tans, and T. S. Shimizu, "High-Throughput 3D tracking of bacteria on a standard phase contrast microscope", *Nat. Commun.*, vol. 6, pp. 1–9, Nov. 2015.

[118] *Shear stress and parabolic velocity profile*. [Online]. Available: `https://summer.skku.edu/`, (accessed: 22.11.2020).

[119] T.-C. Lee, M. Alarcón-Correa, C. Miksch, K. Hahn, J. G. Gibbs, and P. Fischer, "Self-Propelling Nanomotors in the Presence of Strong Brownian Forces", *Nano Lett.*, vol. 14, pp. 2407–2412, 2014.

Acknowledgements

This thesis would not be accomplished without the help and contribution from many people.

My deep appreciation goes first to my supervisor, Prof. Peer Fischer, for being brave and creative enough in giving me, who was with a theoretical background, an opportunity to work in his group. I've been totally amazed by the beauty of the experimental work and the micro/nano world he's shown to me and benefited from his training on PhD students to make them develop independent scientific thoughts. Except for being a great scientist, he's a responsible advisor as well. He's always been open and available for help and discussion.

Furthermore, I would like to thank Prof. Thomas Sottmann and Prof. Elias Klemm for kindly offering to join the examination committee and taking their time to evaluate this work.

I am grateful to Dr. Mihail N. Popescu, Dr. Shang-Yik Reigh and Prof. Snigdha Thakur for their collaborations and mentoring regarding the theory. I want to also thank Prof. Joachim Spatz, Prof. Jürgen Weis, Prof. Frank Gießelmann, Prof. Thomas Sottmann, Prof. Cosima Stubenrauch for granting my access to experimental equipments.

I would like to express my special gratitude to Dr. Tian Qiu, Dr. Athanasios G. Athanassiadis, Dr. Stefan Knoppe, Dr. Vijayakumar Chikkadi, Dr. Dhruv P. Singh, Dr. Andrew Mark for fruitful discussions and the guidance they provided in our lab, and to Conny, Alex, Björn, Moon-Kwang and Damien for helping with the experimental setup. Many thanks go to all the other group members, who always inspire and support each other, throughout the years: Hyeon-Ho, Stefano, Udit, Johannes, Kai, Jan, Vincent, Flo, Melanie, Insook, Eunjin, Hannah, Mariana, Hyunah, Zhichao, Nikhilesh, Rahul, Christian, Nicolas, Dandan, Ida, and Eran. I also appreciate Herbert, Diana, Gabi, Stefan for their support from the Institute of Physical Chemistry of the University of Stuttgart, and Jutta who's been helpful with the administration that keeps the research group running.

At last, I would like to thank my baby Yu, my parents, my husband and my friends for always being there and their constant love, care and encouragement.